Inertio-Capillary Impacts

by

Luke F. L. Alventosa

Submitted to the School of Engineering
in partial fulfillment of the requirements for the degree of

Doctor of Philosophy in Engineering

at

BROWN UNIVERSITY

May 2023

Author .....
School of Engineering
April, 27 2023

Certified by .....
Daniel M. Harris
Assistant Professor
Thesis Supervisor

Accepted by .....
Eric Chason
Chairman, Department Committee on Graduate Theses

BROWN UNIVERSITY
THE GRADUATE SCHOOL

Name: **Luke Alventosa**

Division/Department/Program/School: **Engineering**

Previous degrees: **M.S. SUNY Stony Brook, 2016**
B.S. Swarthmore College, 2015

Title of thesis: **"Inertio-Capillary Impacts"**

Daniel M. Harris

Thesis approved for department by:

Approval of thesis recommended to Graduate Council by Committee:

Roberto Zenit
Anand Oza

Date of Final Examination: **April 19, 2023**

Votes on recommending degree (to be signed by examining committee):

Aye: **Nay:**

Daniel M. Harris

Daniel M. Harris

Presiding Officer

R. Zenit

Anand Oza

Inertio-Capillary Impacts

by

Luke F. L. Alventosa

Submitted to the School of Engineering
on April, 27 2023, in partial fulfillment of the
requirements for the degree of
Doctor of Philosophy in Engineering

Abstract

Droplet impacts are of fundamental importance to the natural water cycle as collision and coalescence of droplets are the primary mechanism by which warm rain forms. Additionally, droplet impacts are of paramount significance in a variety of industrial processes, including spray cooling, wet scrubbing, and even play a role in cooling nuclear reactors. Throughout this work, we utilize a combination of theoretical modeling and experiments to elucidate the dynamics of these common phenomena. The first problem we analyze is a droplet impacting a deep fluid bath. Millimetric drops are generated using a piezoelectric droplet-on-demand generator and normally impact a bath of the same fluid. The limit where capillarity and fluid inertia dominate the interfacial dynamics is investigated. This so-called inertio-capillary limit is shown to define an upper bound on the possible coefficient of restitution for droplet–bath impact. We then consider the scenario where the substrate is no longer deformable, and study the dynamics of non-wetting droplets impacting on stationary and vibrating substrates, with deterministic chaos emerging in the latter case. Extending beyond axisymmetric impacts, we then analyze droplet impact scenarios where there is some relative tangential velocity between the substrate and droplet. We determine the thresholds for coalescence, and our results suggest that substrate deformability plays an important role in transitions between the bouncing and merging regimes. Finally, we consider an analogous solid case to the normal droplet impact studies, where a small rigid sphere impacts and rebounds from a deformable elastic membrane. We perform experiments and identify new previously unreported behaviors in this simple system which are attributed to the non-negligible inertia of the membrane. Overall, the dynamics of these impact scenarios are extremely rich, producing physical phenomena that are inherently multi-scale, requiring information and knowledge from micron to centimeter scales. As showcased here, reduced-order modeling and controlled experiments are essential in distilling some simplicity out of the complexity.

Thesis Supervisor: Daniel M. Harris
Title: Assistant Professor

Acknowledgments

To my parents, Leopoldo Alventosa and Kathleen Lobben: You are my first teachers and without your enduring faith in my abilities, never-ending love and guidance I would not be in the position I am today.

To my siblings Karina, Sean, and Kiera, thank you for being a never-ending stream of new knowledge and always being there to support me. I give thanks everyday for you all and for the laughter we've shared together over the years.

To my advisor and mentor, Daniel Harris, I thank you for continuing to challenge me and providing support and understanding whenever needed. To quote the jazz pianist Herbie Hancock,

"A great teacher is one who realizes that he himself is also a student and whose goal is not dictate the answers, but to stimulate his students' creativity enough so that they go out and find the answers themselves."

Thank you for being an excellent teacher and mentor.

To my partner Mischa, your love and support over the past few years have been light in a challenging time. Creativity flows continuously out of you, and here's to more adventures together.

This work came to fruition not only through the work the I completed over the last 5 years, but through various collaborative efforts within the Harris Lab at Brown. I would like to take the time to offer gratitude to the people who made this work possible.

To Ajay, Carlos, Eli, Elvis, Ian, Jack, John, Navid, Oliver, Radu, Robert, and all of the other members of the Harris Lab, thanks for all of the positive interactions that we had over the years at Brown. Your curiosity and knowledge have been a source of inspiration for me.

Contents

List of Figures

List of Tables

Chapter 1

Introduction

On a mid-March day in 2021, I took a short walk over to Gano Park on the east side of Providence. The weather was mild for the season, and a light drizzle developed. I stopped near the Seekonk river to seek shelter under a tree, and, like many times before, I began to watch the motion of the river. Surprisingly, the surface of the river was almost perfectly smooth, as the coming of the rain had quieted the wind. This is a rare sight, as even the slightest breeze can create a rich variety of capillary-scale surface waves on a body of water. Turbulence in the wind induces these little waves, and the excess pressure on the downwind side of the disturbance causes the small waves to grow. While these waves seem small and inconsequential relative to the overall surface motion, they modify the inherent roughness of the sea surface, which effectively modulates how well the large-scale flow "grips" the surface [Munk, 1951]. This effect comes into play in all different kinds of physical scenarios, from the generation of currents, storm surges, and even larger wavelength waves [Munk, 1951]. Replacing the typical wave interactions on the surface was a pattern equally as complex; a form of deterministic chaos. Each droplet was impacting in a seemingly random location, mimicking the diffuse motion of molecules in a gas.

Warm rain droplets form roughly 2,000 feet above sea level in the lower atmosphere. The Sun creates localized regions of warm air, which rapidly rise into the atmosphere due to buoyancy. These convection rolls are commonplace and occur in miso soup as well as the plasma which makes up the sun itself. This warm air

carries with it the two necessary ingredients for cloud formation: water vapor and seeding particles. These seeding particles can be any small aerosol, and include tree pollen, ash, dirt, sea-spray [Bird et al., 2010]. As the warm air rises, it expands into a larger volume and cools, which decreases the total amount of water vapor that can be stored in a given air volume. The seeding particles act as heterogeneous nucleation sites, and small water droplets form en masse, with upwards of tens of thousands of droplets in a single square meter [Testik and Barros, 2007]. These droplets then are clustered together via the action of turbulence and interact. They can bounce off one another, coalesce, or even breakup if they have too much initial kinetic energy [Pan and Law, 2007].

In interfacial fluid dynamics, the Young-Laplace law describes the capillary pressure difference sustained across the interface between two static fluids due to surface tension. The law states that the difference in pressure between the inside of the drop or bubble and the outside is proportional to the mean curvature of the interface. Thus, small drops and bubbles have a comparatively larger pressure inside than larger drops. This difference in pressures causes coarsening, in which a cascade in the drop size distribution occurs, where small drops coalesce to form into larger drops, shifting the mean droplet size to larger values. In clouds, the process is more complicated, yet despite the many turbulent interactions, droplet rebounds and breakups, the size distribution of the warm rain cloud coarsens and eventually the droplets become too heavy and fall towards the Earth's surface. (This process is not the only way that rain forms, ice may also form on the seeding particles. If the ice falls through warmer air on its way toward the surface a phase change may occur.) As the droplets fall, they interact with their turbulent surroundings, and depending on their size, may even fall faster than they would in still air, selectively riding vorticies that are pushing fluid downwards [Good et al., 2014]. The trajectory of a droplet (or any inertial particle) as it travels in another fluid is a non-linear process [Maxey and Riley, 1983]. The particular combination of inertia, viscosity, and surface tension present in the dynamics of falling droplets, in addition to turbulence in the background flow, created the seemingly random impact location that I was observing.

Upon impact on the river, the droplets coalesced with the still air-water interface, and had just enough initial energy to create a Worthington jet. These little jets are common when an object crosses a fluid interface, and are caused by the collapse of the cavity that forms behind the impacting object [Worthington, 1908]. Sometimes the conditions are just right, and small daughter droplets can pinch off from the jet via a surface tension driven instability. The daughter droplets have a short life time, resting on the interface for a few milliseconds before vanishing into the bulk, injecting a small vortex into the bath, hidden from the observer [Thomson and Newall, 1886]. The impact and coalescence of each droplet induces gravity-capillary waves to form on the surface, rapidly propagating outward in a series of perfectly concentric rings, sorting themselves by their own respective phase speeds. Both the initial impact of the rain drops and coalescence event of the daughter droplets have their own generated wavefield, a mark that they leave on the overall surface before vanishing completely. The waves communicate the event to the surrounding fluid, and dissipate the initial impact energy via the action of viscosity. The calm surface conditions helped me see just how far these small capillary waves would travel before becoming imperceptible.

The natural water cycle is not the only place where a deep understanding of droplet physics is essential. It is very common in fluid mechanics and engineering to come across collections of droplets in the form of sprays. Sprays are used in pesticide application, medicine, de-icing of plane wings, internal combustion engines, nuclear reactors, cooling of hot surfaces, coating applications, and, as we are all painfully aware of now, even play a role in pathogen transport. Due to the extremely diverse range of applications, these physical scenarios have been studied extensively by scientists and engineers for more than a hundred years [Lefebvre and McDonell, 2017]. In this work, we are going to remove some of the complexities of these applications and focus on the fundamental unit in all of these processes: the droplet. In particular, we are going to study in detail the interactions of a single droplet in a variety of different scenarios. These droplets can bounce, coalesce, roll, float, and surf in a complex interplay between the surrounding gas and the droplet. We will utilize a combination of mathematical modeling, computer simulation, and experiments to understand these

processes. Typically, certain parameters are utilized in existing literature to study these impacts. The coefficient of restitution, which we denote as α, is a metric of energy transfer occurring during an impact and is defined in this work as a ratio of the exiting velocity of the droplet to the impacting velocity. The contact time, t_c is commonly reported in the literature as well, as this metric can potentially be used in determining the heat transferred to the drop during an impact, for instance. Additionally, we report the maximum surface deformation, δ. This thesis is organized as follows: First in Chapter 2, the interfacial flow models utilized throughout the work will be derived in detail. Then in Chapter 3, we analyze our first problem, the normal impact of a droplet on a bath of the same fluid, focusing on the regime where the presence of a low density interstitial gas always prevents initial coalescence. We run a series of experiments to elucidate the dynamics of the interfaces, and compare the results of the experiments to our mathematical model and direct numerical simulations. Then in Chapter 4, we extend our exploration to situations where the surrounding gas no longer can support the impacting droplet and coalescence occurs during the initial impact. We examine the role that motion in the bottom fluid has on coalescence thresholds through new experiments, and visualize how the wavefield and droplet deform due to the underlying motion of the interface. In Chapter 5 we extend our analysis to study the impact of a droplet on a rigid non-wetting surface, and attempt to explain some of the interesting trends in experimental data collected across the literature utilizing our mathematical model. We further extend the model to study another form of deterministic chaos that produces period-doubling cascades with a simple drop and vibrating plate system. Finally, we consider an analogous case to the normal impact of a droplet, where a small dense sphere impacts and rebounds from an elastic membrane. In contrast to the droplet impact case, the speed of the wave generated is much faster, and thus the dynamics of the impacting object and substrate are more tightly coupled. We run experiments to elucidate the details of the impact, compare them to simulations, and find interesting regimes of behavior that have been previously unreported. We conclude the work by discussing future directions and outstanding questions. A gallery of interfacial fluid dynamical phenomena

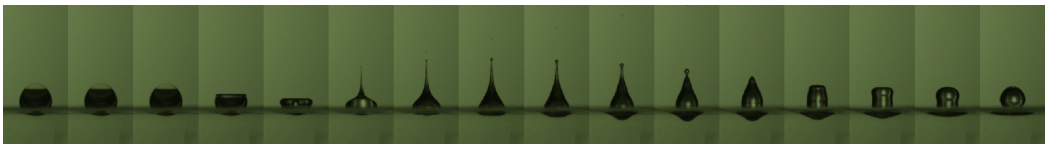

Figure 1-1: The bursting of a bubble on a droplet of silicone oil resting on a bath of the same fluid produces an extremely small aerosol droplet. This aerosol is ejected from the singular jet formed, seen in the 6th panel. Aerosols are formed via the same mechanism when sea foam bubbles burst, and these have been demonstrated to act as cloud seeding particles [Bird et al., 2010].

is included at the end of this section in figures (1-1 - 1-7).

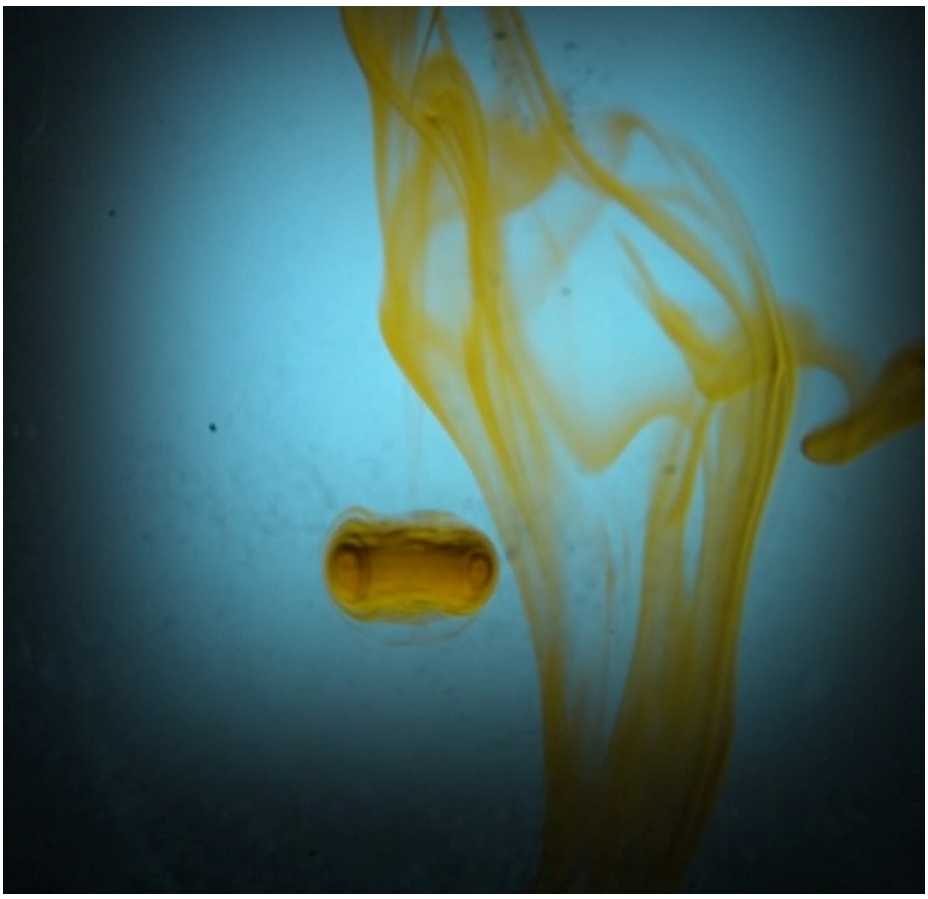

Figure 1-2: The coalescence of droplet of water containing fluorescein produces a vortex ring in a bath of water. The vortex will travel down until viscosity breaks it into smaller vorticies.

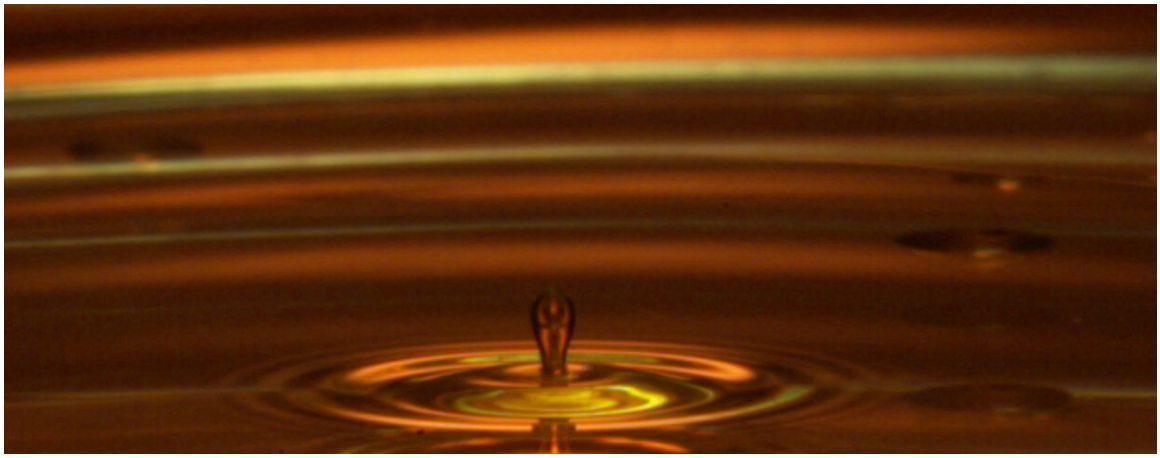

Figure 1-3: A surface tension driven instability pinches off a daughter droplet.

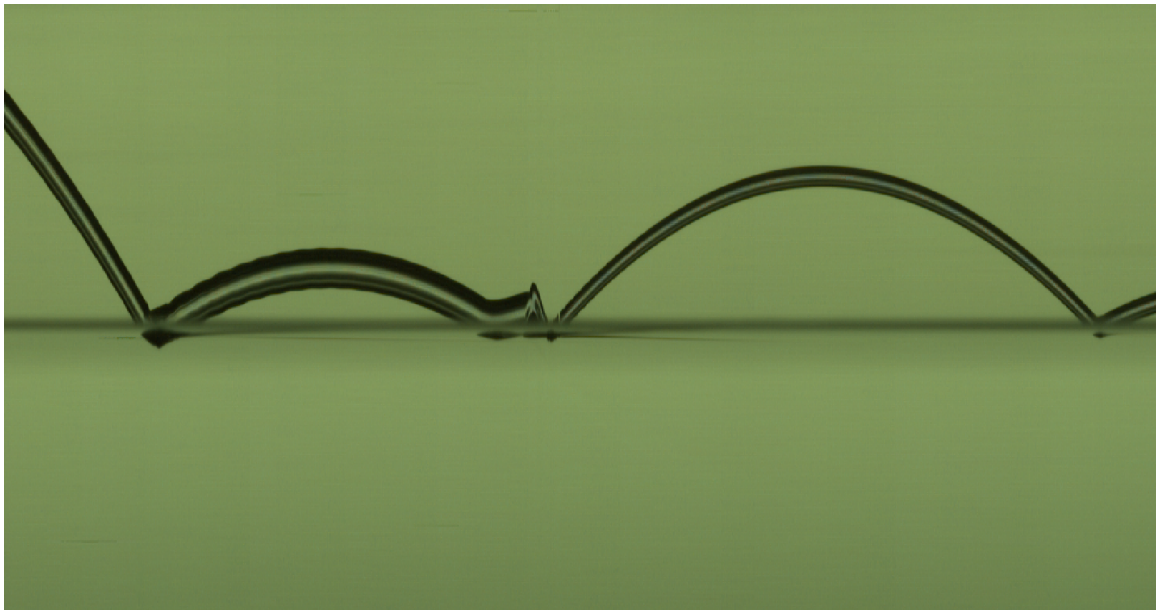

Figure 1-4: After bouncing once on a clean interface, a water droplet partially coalesces with the bath and produces a smaller droplet, which then also bounces. This spatiotemporal diagram, also called a kymograph, stiches together a single pixel wide center stripe from raw video data and plots time along the x-axis.

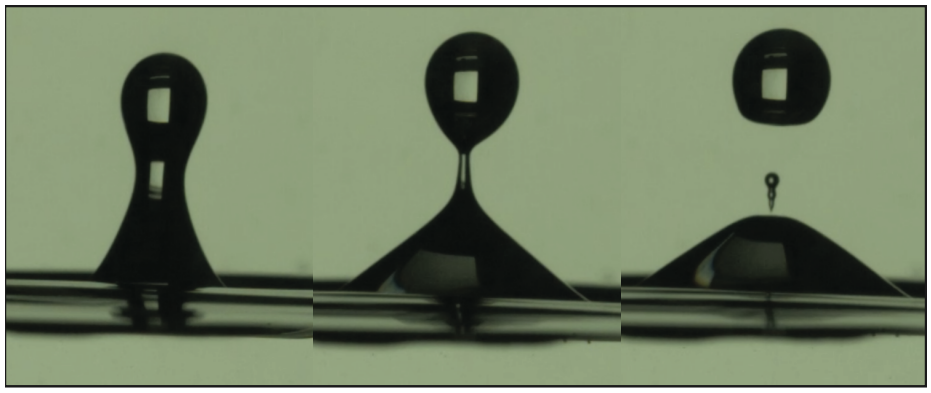

Figure 1-5: The coalescence of droplet of water with radius near the capillary length $l_c = \sqrt{\sigma/\rho g}$ creates a Worthington jet, shown in the left panel. If the droplet impact velocity is just right, this jet will collapse and pinch off daughter droplets.

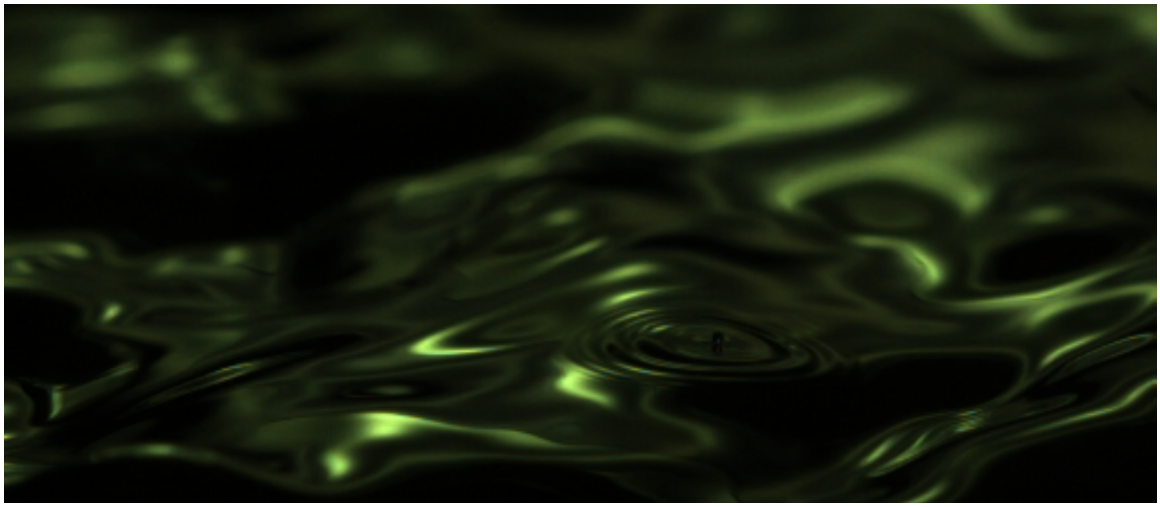

Figure 1-6: A small droplet of water bouncing on a chaotic, wavy surface.

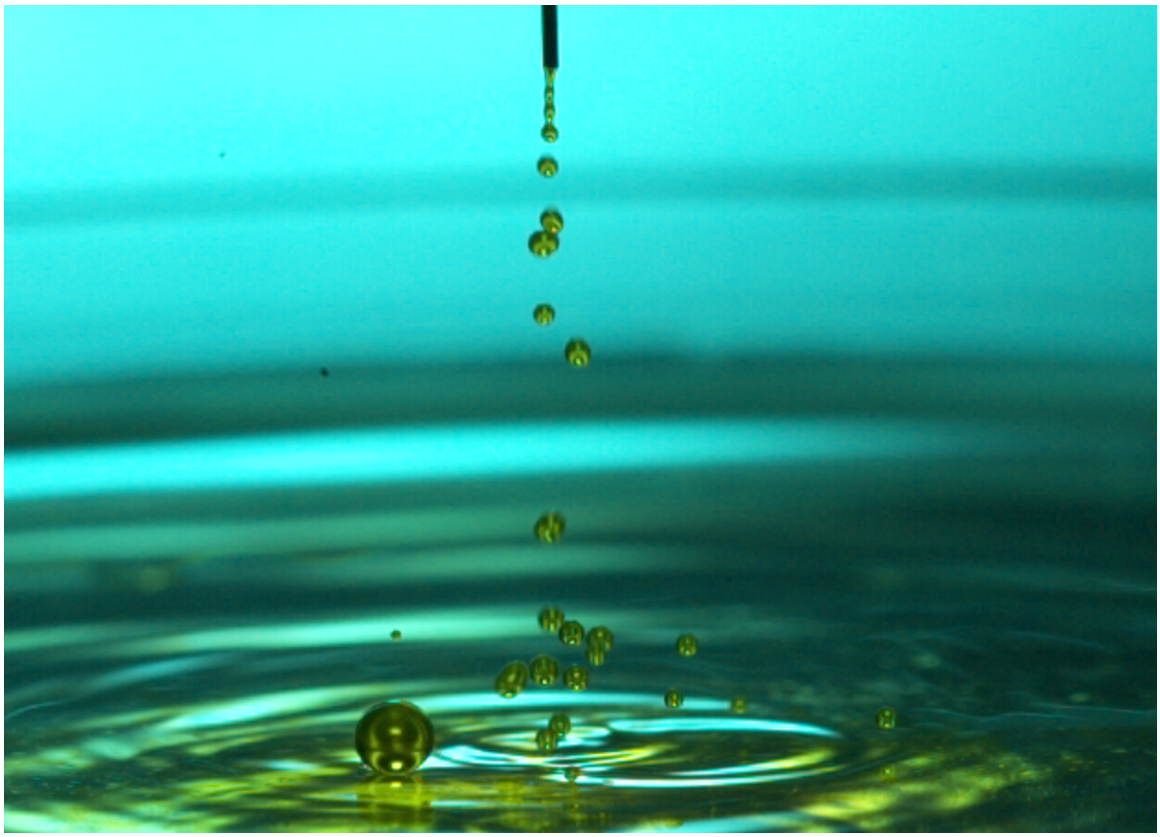

Figure 1-7: A spray of water droplets of different sizes are emitted from the tip of a syringe. These droplets contain fluorescein, which when exposed to blue light glows green. These droplets not only bounce off the free surface, but off each other.

Chapter 2

Weakly Viscous Interfacial Flow Modeling

In this section, we will detail two weakly viscous interfacial flow models to describe the motion of droplet interfaces and planar fluid interfaces. These derivations hold for fluid interfaces where the density and viscosity of the surrounding fluid are much smaller than the other fluid. In this work, we will assume that the surrounding fluid is a gas, and the other fluid is some Newtonian liquid. Both of these models are derived from first principles and require no fitting parameters. We then apply orthogonal function decompositions for the flow variables used in these models, and derive sets of ordinary differential equations that describe the flow variables. This reduction in complexity comes with it a large decrease in computational time, which will allow us to model many different inertio-capillary impact problems. These models, as well as the expressions for the surplus energies, have been previously derived, yet the derivations are repeated here for clarity. Some relevant aspects of the final equations from this chapter are repeated in the following chapters when applied.

2.1 Bath Interface Model

We aim to develop a theory governing the impact of capillary-scale objects on a free interface. Presently, direct numerical simulation has been utilized to study these

problems, yet this approach comes with high computational cost. The present work attempts to solve this problem using a linearized, quasi-potential flow model following the work of [Galeano-Rios et al., 2017] and [Blanchette, 2016]. For the problem of an object impacting on a free interface, the Navier-Stokes equations govern the flow generated by the fluid-object interaction. Ordinary differential equations can be written for the motion of the object itself. Assuming the flow to be incompressible and isothermal, we can write these equations as

$$\frac{\partial \mathbf{u}}{\partial t} + (\mathbf{u} \cdot \nabla)\mathbf{u} = -\frac{1}{\rho}\frac{\partial P}{\partial \mathbf{x}} + \frac{1}{\rho}\nabla \cdot \mathbf{T} + \mathbf{g} \ , \tag{2.1}$$

$$\nabla \cdot \mathbf{u} = 0 \ , \tag{2.2}$$

where $\mathbf{u} = [u, v, w]^T$ is the fluid velocity vector, $\mathbf{T}$ is the viscous stress tensor, P is the pressure field, $\mathbf{g} = \nabla[0, 0, gz]^T$ is the gravitational force vector, and ρ, $\nu = \frac{\mu}{\rho}$ are the fluid density and kinematic viscosity. For the current problem, these equations are subject to the following boundary conditions: a kinematic and dynamic condition for the flow at the interface, and that far away from the interface, viscosity dampens out any motion. The dynamic boundary condition can be written as

$$-P\hat{n} + \mathbf{T} \cdot \hat{n} = (\sigma\kappa - p_s)\hat{n}. \tag{2.3}$$

Here, κ is the mean curvature of the interface, p_s is a forcing pressure evaluated at the fluid interface due to the impact of an object, σ is the fluid surface tension, and $\hat{n}$ is the outward facing unit normal vector. If a function describing the motion of the free interface is represented by $\eta = \eta(r, \theta, t)$, then we can define a functional $F = F(\mathbf{x}, t) = \eta - z$, assuming the undisturbed interface is situated in the r-θ plane. Then, the normal vector can be written as

$$\hat{n} = \frac{\nabla F}{|\nabla F|} = \frac{1}{\sqrt{1 + (\partial_r \eta)^2 + (\frac{1}{r}\partial_\theta \eta)^2}}[-\partial_r \eta, -\frac{1}{r}\partial_\theta \eta, 1]. \tag{2.4}$$

In this notation, ∂_i denotes partial differentiation with respect to the i^{th} variable. The kinematic condition can be formulated as

$$\partial_t \eta + \mathbf{u} \cdot \nabla(\eta - z) = 0. \tag{2.5}$$

The final boundary condition is that the fluid velocity vanishes on the bottom of the bath, that is $\boldsymbol{u}|_{z=h_0} = 0$, where h_0 is the depth of the bath. We also assume that the bath is deep, and thus $\lambda \ll |h_0|$, where λ is some characteristic wavelength of the flow. That is, far away from the free surface, $\mathbf{u}$ approaches zero via the action of viscosity. Furthermore, we will assume the fluid to be Newtonian, and utilizing the continuity equation $\nabla \cdot \mathbf{u} = 0$, the viscous stress tensor can be written as the sum of a symmetric and anti-symmetric tensor $\mathbf{T} = \mu(\nabla \mathbf{u} + \nabla \mathbf{u}^T)$.

We will assume that the deformation of the interface is small, and thus that the waves created by impact are well within a linear approximation. We therefore can linearize the dynamic and kinematic boundary conditions about $z = 0$, and neglect any powers of the velocity $\mathbf{u}$ or product of the velocity and surface elevation η.

Therefore, the governing equations of motion reduce to

$$\nabla \cdot \mathbf{u} = 0, \tag{2.6}$$

$$\frac{\partial \mathbf{u}}{\partial t} = -\frac{1}{\rho}\frac{\partial P}{\partial \mathbf{x}} + \nu \Delta \mathbf{u} + \mathbf{g}, \tag{2.7}$$

with boundary conditions

$$\partial_z u + \partial_r w = 0, \tag{2.8}$$

$$\partial_z v + \frac{1}{r}\partial_\theta w = 0, \tag{2.9}$$

$$-P + 2\mu \partial_z w = \sigma\kappa - p_s, \tag{2.10}$$

and

$$\partial_t \eta = w. \tag{2.11}$$

These boundary conditions are applied at the undisturbed free surface at $z = 0$. We will use a Helmholtz decomposition, where $\mathbf{u} = \nabla\phi + \nabla \times \Psi$. Here, ϕ is the scalar potential and $\Psi = [\psi_1, \psi_2, \psi_3]^T$ is the vector stream function. In order to ensure that the decomposition satisfies the bottom boundary conditions, we require that $\left[\partial_r\phi, \frac{1}{r}\partial_\theta\phi, \partial_z\phi\right]^T|_{h_0} = 0$ and $\nabla \times \Psi = 0$ at $z = h_0$.

Substituting this decomposition into the governing equations transforms the problem to

$$\Delta\phi = 0, \tag{2.12}$$

$$\nabla(\partial_t\phi) + \partial_t(\nabla \times \Psi) = -\nabla\frac{\widetilde{P}}{\rho} + \nu\Delta(\nabla \times \Psi), \tag{2.13}$$

where we have used $\widetilde{P} = P + \mathbf{g}$ and a few useful vector calculus identities. If we choose $\partial_t\phi = -\frac{\widetilde{P}}{\rho}$ and $\partial_t(\nabla \times \Psi) = \nu\Delta(\nabla \times \Psi)$ then equation (2.13) is satisfied then our governing equation becomes

$$\Delta\phi = 0. \tag{2.14}$$

Applying the decomposition to the boundary conditions gives us

$$0 = \partial_z(\partial_r\phi + \psi_1) + \partial_r(\partial_z\phi + \psi_3), \tag{2.15}$$

$$0 = \partial_z(\frac{1}{r}\partial_\theta\phi + \psi_2) + \frac{1}{r}\partial_\theta(\partial_z\phi + \psi_3), \tag{2.16}$$

$$\partial_t\phi + g\eta = -2\nu\partial_z^2\phi - 2\nu\partial_z\psi_3 + \frac{\sigma}{\rho}\kappa - \frac{p_s}{\rho}, \tag{2.17}$$

where we have again used $\widetilde{P} = P + gz$ and $\partial_t\phi = -\frac{\widetilde{P}}{\rho}$. If we take a derivative of equation (2.15) and add it to a derivative of (2.16), and use (2.13) written for the z coordinate, we obtain

$$\partial_t\psi_3 = 2\nu\nabla^2(\partial_z\phi + \psi_3), \tag{2.18}$$

where we have also taken advantage of the fact that $\nabla \cdot \Psi = 0$. Here, $\nabla^2 = \partial_r^2 + (1/r)\partial_r + (1/r^2)\partial_\Theta^2$ is the surface Laplacian, not to be confused with the full Laplacian, which we denote in this text by Δ. Substituting the decomposition into the kinematic

boundary condition (2.11), we have

$$\partial_t \eta = \partial_z \phi + \psi_3. \tag{2.19}$$

Combining equation (2.18) and (2.19) yields

$$\partial_t \psi_3 = 2\nu \nabla^2 (\partial_t \eta). \tag{2.20}$$

Since the fluid is initially at rest with an undisturbed interface, this expression implies that

$$\psi_3 = 2\nu \nabla^2 (\eta). \tag{2.21}$$

Following [Galeano-Rios et al., 2017], if we non-dimensionalize equation (2.17), use the result from (2.21), and make a high-Reynolds number flow assumption, we can eliminate ψ_3 from the dynamic boundary condition (2.17), writing

$$\partial_t \phi = -g\eta - 2\nu \partial_z^2 \phi + \frac{\sigma}{\rho}\kappa - \frac{p_s}{\rho}. \tag{2.22}$$

Here, we define the Reynolds number as $Re = \frac{RU}{\nu}$, with U being some characteristic velocity and R is the undeformed radius of the droplet. Then, the kinematic boundary condition can be reformulated without using the stream function as

$$\partial_t \eta = \partial_z \phi + 2\nu \nabla^2 \eta, \tag{2.23}$$

even though we have assumed that there is non-negligible vorticity in the flow. In summary, we have

$$\nabla^2 \phi + \partial_z^2 \phi = 0, \quad z \leq 0, \tag{2.24}$$

$$\partial_t \eta = \partial_z \phi + 2\nu \nabla^2 \eta, \quad z = 0, \tag{2.25}$$

$$\partial_t \phi = -g\eta - 2\nu \partial_z^2 \phi + \frac{\sigma}{\rho}\kappa - \frac{p_s}{\rho}, \quad z = 0, \tag{2.26}$$

$$\boldsymbol{u} = \nabla \phi = 0 \text{ at } z = h_0. \tag{2.27}$$

2.1.1 Eigenfunction Decomposition of Surface Waves

We seek to apply the above linearized theory to the impact of capillary-scale objects on a free, undisturbed interface. We assume that the impact occurs in a bath of some viscous fluid which is subject to two important boundary conditions, mainly that $\partial_n \phi = 0$ on the walls of the bath and that $\partial_z \phi = 0$ on the bottom of the bath. If we take ∂_n of (2.23),

$$\partial_t \partial_n \eta = 2\nu \nabla^2 \partial_n \eta.$$

In order to satisfy this additional boundary constraint, we will assume that

$$\partial_n \eta = 0$$

on the walls of the container. Thus, the free surface of the bath is required to maintain a constant contact angle of 90° on the walls. Applying the same operation to (2.22), making use of $\partial_n \phi = 0$ on the walls, we obtain

$$0 = \frac{\sigma}{\rho} \partial_n (\partial_r^2 \eta + \frac{1}{r^2} \partial_\theta^2 \eta),$$

where we have utilized $\kappa \approx \nabla^2 \eta$, consistent with our linear approximation. Then, following [Benjamin and Ursell, 1954], since this expression for the dynamic boundary condition will hold on any bounding curve K, we can utilize an orthogonal function expansion for the unknowns η, ϕ and their derivatives.

These orthogonal functions $S_{j,m}(x, y)$ must satisfy

$$(\nabla^2 + k_{j,m}^2) S_{j,m} = 0, \tag{2.28}$$

inside of any bounding curve K that exists on the border of the bath and the boundary condition of $\partial_n S_{j,m} = 0$ on K. $k_{j,m}$ are the eigenvalues of the system, and depend on the choice of the physical domain of the problem. If the boundary curve K is a circle, the functions become $S_{j,m} = J_j(k_{j,m} r) \cos j\Theta$. Here J_j are Bessel functions of the first kind and $k_{j,m}$ are the solutions to $J_j'(k_{j,m} b) = 0$, where b is the bath radius.

If we further assume the problem to be axisymmetric, then we can choose $j = 0$, and write $S_{0,m} = J_0(k_{0,m}r)$. For convenience, we define $k_{0,m} = k_m$ henceforth. We then can express the free surface elevation as

$$\eta = \sum_{m=0}^{\infty} a_m J_0(k_m r).$$

In order to determine ϕ, we will employ separation of variables. Assume $\phi(r, z, t) = R(r)T(t)Z(z)$. We have, from the continuity equation,

$$\Delta\phi = 0 \tag{2.29}$$

subject to the boundary conditions

$$\partial_z\phi|_{z=0} = \partial_t\eta - 2\nu\nabla^2\eta, \tag{2.30}$$

$$\partial_z\phi|_{z=-h_0} = 0, \tag{2.31}$$

$$\phi|_{z=-h_0} = 0. \tag{2.32}$$

In cylindrical coordinates, the Laplacian operator can be written as

$$\Delta f = \partial_r^2 f + \frac{1}{r}\partial_r f + \frac{1}{r^2}\partial_\theta^2 f + \partial_z^2 f = 0. \tag{2.33}$$

Substituting ϕ into this expression yields

$$\partial_r^2 R(TZ) + \frac{1}{r}\partial_r R(TZ) + \partial_z^2 Z(RT) = 0.$$

Separating the variables again and doing a little rearrangement gives us

$$\frac{1}{R}(\partial_r^2 R + \frac{1}{r}\partial_r R) = -\frac{1}{Z}\partial_z^2 Z = -k_m^2.$$

This yields two ordinary differential equations for two of the three unknown functions.

$$\partial_r^2 R + \frac{1}{r}\partial_r R + k_m^2 R = 0,$$

$$\partial_z^2 Z - k_m^2 Z = 0.$$

The first equation is simply Bessel's equation, and as such has solution $R_m(r) = CJ_0(k_m r) + DY_0(k_m r)$. Since the solution must be defined over the entire domain and Y_0 is singular at the origin, we set $D = 0$, and we can set $C = 1$. The second ODE has a known solution as well, and is

$$Z_m(z) = A \sinh k_m z + B \cosh k_m z.$$

Utilizing the boundary condition that $\partial_z \phi|_{z=-h_0} = \partial_z Z|_{z=-h_0} = 0$ we determine

$$A = B \tanh k_m h_0.$$

Additionally, the value of B is arbitrary and we can set it to $B = 1$. Now,

$$\phi_m = T_m J_0(k_m r)(\tanh k_m h_0 \sinh k_m z + \cosh k_m z), \tag{2.34}$$

where $T_m = T_m(t)$ is yet to be determined. Applying the final boundary condition, equation (2.30), gives us

$$T_m J_0(k_m r) k_m \tanh k_m h_0 = \frac{da_m}{dt} J_0(k_m r) + 2\nu k_m^2 a_m J_0(k_m r). \tag{2.35}$$

Rearranging, we get

$$T_m = \frac{1}{k_m \tanh k_m h_0} \left(\frac{da_m}{dt} + 2\nu k_m^2 a_m \right). \tag{2.36}$$

Therefore, the completed expression for ϕ is

$$\phi_m = \left(\frac{da_m}{dt} + 2\nu k_m^2 a_m \right) J_0(k_m r) \frac{\cosh k_m (h_0 + z)}{k_m \sinh k_m h_0}, \tag{2.37}$$

which we have utilized some useful hyperbolic trigonometric identities. This expression is for one mode only. To get the complete expression we must sum over all modes

m. In summary, we have

$$\eta = \sum_{m=0}^{\infty} a_m J_0(k_m r), \tag{2.38}$$

$$\nabla^2 \eta = -\sum_{m=0}^{\infty} k_m^2 a_m J_0(k_m r), \tag{2.39}$$

$$\phi = \sum_{m=0}^{\infty} \left(\frac{da_m}{dt} + 2\nu k_m^2 a_m \right) J_0(k_m r) \frac{\cosh k_m(h_0 + z)}{k_m \sinh k_m h_0}. \tag{2.40}$$

In order to arrive at the final equations of motion for the free surface, we take the decompositions (2.38-2.40) and substitute them into the dynamic boundary condition (2.26). Rearranging, we find

$$\sum_{m=0}^{\infty} \left[\frac{d^2 a_m}{dt^2} + 4\nu k_m^2 \frac{da_m}{dt} + \left(\frac{\sigma k_m^2}{\rho} + g \right) k_m \tanh(k_m h_0) a_m \right] J_0(k_m r) = -\frac{p_s}{\rho} k_m \tanh(k_m h_0). \tag{2.41}$$

Each wave mode in the bath is described by a forced, damped harmonic oscillator equation.

2.1.2 Bath Energy Expressions

We can also utilize the expansions for the bath interface to write down expressions for the surface energy, kinetic energy, and gravitational potential energy of the waves generated on the surface in terms of the mode amplitudes and their derivatives. In the expressions that follow, Δ represents the excess surface energy relative to the undisturbed free surface. Following Appendix B in [Durey and Milewski, 2017], we write

$$\Delta SE = \iint \sigma(\sqrt{1 + |\eta|} - 1) dA \tag{2.42}$$

For small deformations, $|\eta| \ll 1$, and

$$\Delta SE = \pi\sigma \int_0^b |\nabla \eta|^2 r dr \tag{2.43}$$

Expanding the derivative in the above expression as $|\nabla\eta|^2 = \nabla\cdot(\eta\underline{\nabla}\eta) - \eta\nabla_H^2\eta$ and using the divergence theorem in 2D yields

$$\Delta SE = -\pi\sigma\int_0^b \eta\nabla^2\eta r dr. \tag{2.44}$$

Substituting the expressions (2.38) and (2.39) yields

$$\Delta SE = \frac{\pi b^2\sigma}{2}\sum_{m=0}^{\infty} k_m^2 a_m^2 J_0^2\left(k_m b\right). \tag{2.45}$$

The excess gravitational potential energy can be written as

$$\Delta GPE = \frac{1}{2}\rho g\int_0^b\int_0^{2\pi}\eta^2 r d\theta dr, \tag{2.46}$$

$$= \frac{\pi b^2\rho g}{2}\sum_{m=0}^{\infty} a_m^2 J_0^2\left(k_m b\right). \tag{2.47}$$

We can perform the same analysis for the excess kinetic energy of the wave. Starting with the definition

$$\Delta KE = \int_0^b\int_0^{2\pi}\int_{-h_0}^{\eta}\frac{1}{2}\rho|\nabla\phi|^2 r dz d\theta dr. \tag{2.48}$$

From the continuity equation, we write $|\nabla\phi|^2 = \nabla\cdot(\phi\underline{\nabla}\phi)$, and we utilize the divergence theorem again to write

$$\Delta KE = \pi p\int_0^b \phi\frac{\partial\phi}{\partial z} r dr. \tag{2.49}$$

Substituting in (2.40)

$$\Delta KE = \frac{\pi b^2\rho}{2}\sum_{m=0}^{\infty}\frac{1}{k_m}\left(\frac{da_m}{dt} + 2\nu k_m^2 a_m\right)^2 \coth\left(k_m h_0\right) J_0^2\left(k_m b\right). \tag{2.50}$$

In summary:

$$\Delta E = \triangle SE + \triangle GPE + \Delta KE,$$
$$\Delta SE = \frac{\pi b^2 \sigma}{2} \sum_{m=0}^{\infty} k_m^2 a_m^2 J_0^2 \left(k_m b\right),$$
$$\Delta GPE = \frac{\pi b^2 \rho g}{2} \sum_{m=0}^{\infty} a_m^2 J_0^2 \left(k_m b\right),$$
$$\Delta KE = \frac{\pi b^2 \rho}{2} \sum_{m=0}^{\infty} \frac{1}{k_m} \left(\frac{da_m}{dt} + 2\nu k_m^2 a_m\right)^2 \coth\left(k_m h_0\right) J_0^2 \left(k_m b\right).$$

2.2 Droplet Interface Model

In this section, we will derive the interfacial model that we utilize throughout this work for the droplet. Similar to the previous section, we decompose the deformation of the interface into a set of mode amplitudes which are functions of time only. That is, $r = \xi(\theta, \varphi, t)$ and

$$\xi(\theta, t) = R + \sum_{l=0}^{\infty} \sum_{n=-l}^{l} \beta_l^n(t) Y_l^n(\theta, \varphi), \tag{2.51}$$

with $Y_l^n = P_l^n(\cos\theta) e^{in\varphi}$, where $P_l^n(\cos\theta)$ are the Legendre polynomials. Additionally, consistent with our previous derivation, we assume the problem to be axisymmetric, and set $n = 0$. We will drop the n from the expressions for convenience. Then, following [Chandrasekhar, 2013, Reid, 1960, Miller and Scriven, 1968], we assume that the flow is incompressible, and a velocity potential function can be written that satisfies

$$\Delta\phi = 0 \tag{2.52}$$

Again, utilizing separation of variables, the solution to Laplace's equation can be found, [Chandrasekhar, 2013, Reid, 1960], and is written as

$$\phi = \sum_{l=0}^{\infty} B_l(t) \left(\frac{r}{R}\right)^l P_l, \tag{2.53}$$

where $B_l(t)$ is some other unknown amplitude coefficient for the l^{th} mode. As in the prior section, we assume linearity of the deformations and thus the kinematic boundary condition can be written as

$$\partial_t \xi = \partial_r \phi, \tag{2.54}$$

leading to

$$\sum_{l=0}^{\infty} \frac{d\beta_l}{dt} P_l = \sum_{0}^{\infty} B_l \frac{l}{R} P_l. \tag{2.55}$$

Dropping the sums, we have

$$\frac{d\beta_l}{dt} = B_l \frac{l}{R} \tag{2.56}$$

We then turn to a statement of the conservation of energy,

$$T = \dot{W} - \varepsilon \tag{2.57}$$

where $T = K + G$ is the sum of the kinetic and gravitational potential energies, $\dot{W}$ is the rate of surface work done on the droplet, and ε is the rate of energy dissipation due to viscosity. These expressions can be written as

$$\dot{W} = \int_{dS} SE_d \cdot \nabla\phi dS, \tag{2.58}$$

$$SE_d = (-p_s + \sigma\kappa)\hat{n}, \tag{2.59}$$

$$K = \int_V \rho \nabla\phi \cdot \nabla\phi dV, \tag{2.60}$$

$$G = \frac{4}{3}\pi\rho R^3 g\beta_1, \tag{2.61}$$

$$\varepsilon = \int_{dV} 2\mu \mathbf{D} \cdot \mathbf{D} dV. \tag{2.62}$$

We take the outward facing normal vector $\hat{n} = [\hat{e_r}, 0, 0]^\top$, the differential surface element as $dS = r^2 \sin\theta d\theta d\phi$, and $\mathbf{D} = (\nabla\mathbf{u} + \nabla\mathbf{u}^T)$ is the deviatoric stress tensor.

Then, the contribution of the droplet curvature to the rate of surface work is

$$\sigma\kappa = -\frac{2\sigma}{R} - \frac{\sigma(l-1)(l+2)}{R^2}\sum_{l=0}^{\infty}\beta_l P_l. \tag{2.63}$$

We can express $\dot{W}$ as

$$\dot{W} = -2\pi\int_0^{\pi}\sum_{l=0}^{\infty} p_s B_l P_l \frac{l}{R}\left(\frac{r}{R}\right)^{l-1} r^2\sin\theta d\theta d\phi \tag{2.64}$$

$$-2\pi\int_0^{\pi}\frac{\sigma(l-1)(l+2)}{R^2}\sum_{l=0}^{\infty}\beta_l B_l P_l^2\frac{l}{R}\left(\frac{r}{R}\right)^{l-1} r^2\sin\theta d\theta d\phi \tag{2.65}$$

Assuming linear deformations, evaluating at $r = R$, and utilizing the kinematic boundary condition, we arrive at

$$\dot{W} = -2\pi R^2\int_0^{\pi}\sum_{l=0}^{\infty} p_s\frac{d\beta_l}{dt}\sin\theta P_l d\theta \tag{2.66}$$

$$-\sum_{l=0}^{\infty}\frac{4\pi}{2l+1}\frac{\sigma(l-1)(l+2)}{l}\beta_l\frac{d\beta_l}{dt}. \tag{2.67}$$

We can express T and ε as

$$T = \sum_{l=0}^{\infty}\frac{2\pi l}{2l+1}\rho R B_l^2 - \sum_{l=0}^{\infty}\rho\frac{4}{3}\pi R^3 g\beta_1, \tag{2.68}$$

$$\varepsilon = \sum_{l=0}^{\infty} 8\pi l(l-1)\frac{\mu}{R}B_l^2. \tag{2.69}$$

Additionally, we recognize that the contribution of the zeroth mode must be zero at all times $\beta_0 = 0$, otherwise our assumption of incompressibility will be violated [Chandrasekhar, 2013, Moláček and Bush, 2012]. Taking the time derivative of T and

substituting the expressions into (2.57) yields

$$\sum_{l=1}^{\infty}\frac{4\pi l}{2l+1}\rho R B_l\frac{dB_l}{dt}-\sum_{l=1}^{\infty}\rho\frac{4}{3}\pi R^3 g\frac{d\beta_l}{dt}=-2\pi R^2\int_0^{\pi}\sum_{l=1}^{\infty}p_s\frac{d\beta_l}{dt}\sin\theta P_l d\theta$$
$$-\sum_{l=1}^{\infty}\frac{4\pi}{2l+1}\frac{\sigma(l-1)(l+2)}{l}\beta_l\frac{d\beta_l}{dt}$$
$$-\sum_{l=0}^{\infty}8\pi l(l-1)\frac{\mu}{2}B_l^2.$$

Now, we again utilize the linearized kinematic boundary condition, and divide out one $\frac{d\beta_l}{dt}$, rearrange and arrive at the final result,

$$\sum_{l=1}^{\infty}\frac{d^2\beta_l}{dt^2}-\sum_{l=1}^{\infty}g\delta_{1l}+\sum_{l=1}^{\infty}\frac{l(l-1)(l+2)\sigma}{\rho R^3}\beta_l+\sum_{l=1}^{\infty}2(2l+1)(l-1)\frac{\mu}{\rho R^2}\frac{d\beta_l}{dt}$$
$$=-\sum_{l=1}^{\infty}\frac{(2l+1)}{2}\frac{l}{\rho R}\int_0^{\pi}p_s P_l\sin\theta d\theta.$$

We can rearrange the result and drop the sums for convenience to yield a set of ODE's that govern each individual droplet mode $\beta_l(t)$,

$$\frac{d^2\beta_l}{dt^2}+2(2l+1)(l-1)\frac{\mu}{\rho R^2}\frac{d\beta_l}{dt}+\frac{l(l-1)(l+2)\sigma}{\rho R^3}\beta_l$$
$$=-\frac{(2l+1)}{2}\frac{l}{\rho R}\int_0^{\pi}p_s P_l\sin\theta d\theta+g\delta_{1l}$$

2.2.1 Droplet Energy Expressions

We summarize the expressions for the excess droplet kinetic, gravitational potential, and surface energies relative to the undeformed state here in terms of the decomposition variables as

$$\Delta K=\sum_{l=2}^{\infty}\rho R^3\frac{2\pi}{l(2l+1)}\frac{d\beta_l}{dt}^2, \tag{2.70}$$

$$\Delta G=\rho\frac{4}{3}\pi R^3 g\beta_1, \tag{2.71}$$

$$\Delta SE_d=2\pi\sigma\sum_{l=2}^{\infty}\frac{l^2+l-2}{2l+1}\beta_l^2. \tag{2.72}$$

These expressions have also been derived in [Moláček and Bush, 2012, Balla et al., 2019]. In the following sections, we will apply these models to help further our understanding of inertio-capillary impact problems, and compare the results of the models directly to experiments and direct numerical simulations.

Chapter 3

Inertio-capillary rebound of a droplet impacting a fluid bath

The work presented in this chapter appears as part of a publication in the Journal of Fluid Mechanics as *Alventosa, L. F., Cimpeanu, R., and Harris, D. M. (2023). Inertio-capillary rebound of a droplet impacting a fluid bath. Journal of Fluid Mechanics, 958, A24.* LFA wrote the quasi-potential models, performed and analyzed the experiments, wrote and utilized the simulation code, with assistance and mentorship from DMH. DMH performed the scaling analysis and RC contributed the DNS. All authors contributed to the writing of the paper.

3.1 Introduction

Droplet impacts occur frequently in both natural and industrial settings. Rain drops impacting on leaves have been shown to be a primary mechanism for pathogen transport among plants [Kim et al., 2019] and birds with superhydrophobic feathers stay warmer in a cold rain due to a reduced droplet contact time [Shiri and Bird, 2017]. Spray cooling devices have attracted the attention of researchers due to the large heat transfer rates and high uniformity of heat transfer [Kim, 2007]. Wet scrubbing of exhaust gases relies on the inertial impaction of small particles and aerosols on the surface of freely falling droplets [Park et al., 2005]. Various other drop impact

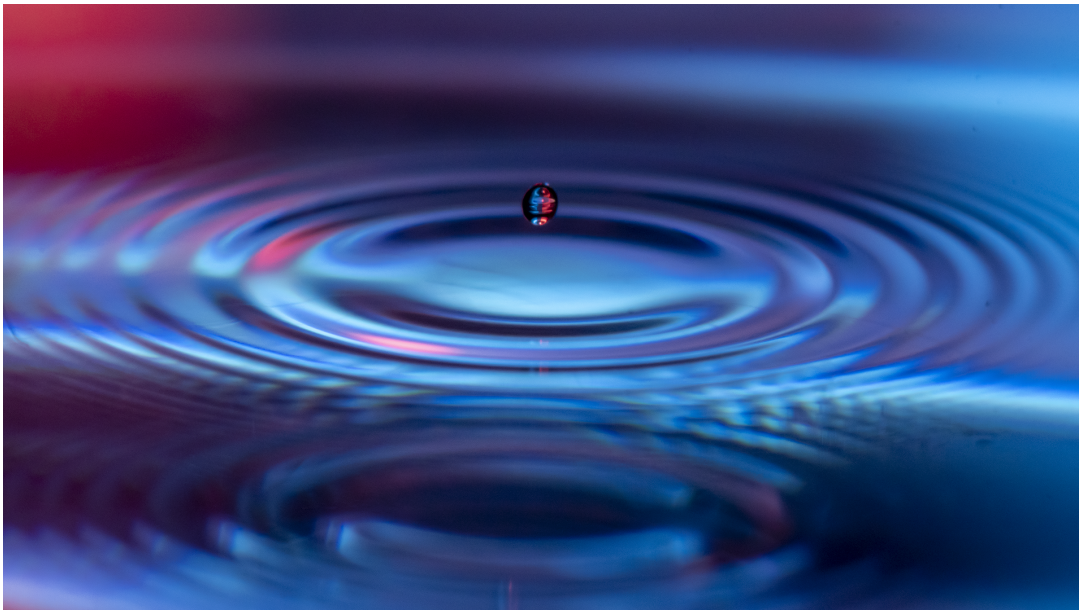

Figure 3-1: A small water droplet ($R \approx 0.4$ mm) rebounds from a bath of the same fluid.

phenomena, such as splashing, were experimentally documented by Worthington at the start of the 20^{th} century [Worthington, 1908]. More recently, droplets bouncing repeatedly on a vertically oscillated bath have received considerable interest as a macroscopic pilot-wave system capable of reproducing some behaviors reminiscent of quantum particles [Couder et al., 2005b, Bush and Oza, 2020]. For instance, bouncing droplets confined to submerged cavities can exhibit wave-like statistical behavior analogous to electrons in quantum corrals [Harris et al., 2013, Sáenz et al., 2018]. Droplet impact onto solid surfaces is also an extremely well-studied field [Yarin, 2006, Josserand and Thoroddsen, 2016], with the combination of high quality experiments and direct numerical simulation (DNS) leading to a deep understanding of the multi-scale dynamics.

The problem of droplet coalescence onto a bath of the same fluid has also been studied extensively over the last century and a half, beginning with [Rayleigh, 1879] and [Thomson and Newall, 1886]. These early works included sketches of drop-interface coalescence, as well as a detailed description of the vortices that are formed in the fluid bath. Preceding coalescence, the thin gas film that forms between the two interfaces drains until van der Waals forces act to initiate coalescence. Coales-

cence of a drop into a bath occurs when the film is on the order of 100 nm thick [Couder et al., 2005a, Yarin, 2006, de Ruiter et al., 2012, Kavehpour, 2015]. The development of accessible high-speed photography and high performance computing has ushered in a rapid expansion in quantity and quality of data on these free surface problems. [Thoroddsen and Takehara, 2000] used a high-precision and high-speed visualization setup to quantify the coalescence time of droplets on an air-liquid interface. [Tang et al., 2019] studied the dynamics of the gas layer on a liquid bath whose depth was similar to that of the droplet radius. The rich class of outcomes and dynamics that arise from such a simple interaction between droplet, surrounding gas, and interface proves that these fundamental problems merit considerable attention.

During contact, the combined effects of inertia, surface tension, gravity, and viscosity govern the hydrodynamic interaction between the droplet and the interface, and the complex balance of forces within this regime creates the variety of distinct phenomena. The Weber number $We = \rho V_0^2 R/\sigma$, the Bond number $Bo = \rho R^2 g/\sigma$, and the Ohnesorge number $Oh = \mu/\sqrt{\sigma R \rho}$ are often used to describe these capillary-scale dynamics. In this work, R represents the undeformed droplet radius, ρ, σ, μ are the density, surface tension, and viscosity of the fluid in both the droplet and bath, V_0 is the impact velocity of the droplet, and g is the gravitational acceleration. The present work focuses on the inertio-capillary regime, where fluid inertia and surface tension dominate viscous and gravitational effects (specifically, $Oh \ll 1$ and $Bo \ll 1$). During impact, a thin gas film develops between the free interface and surface of the droplet. The drainage of this thin film plays a crucial role in determining the fate of the droplet: specifically whether it rebounds from or coalesces with the underlying bath [de Ruiter et al., 2012]. At sufficiently low We, the droplet and the interface never come into physical contact and remain separated by a stable air film. The droplet then levitates on this thin film and can eventually rebound due to the relaxation of the bath and droplet interface. Droplets bouncing on a free interface were first documented by Reynolds in 1881, when he noted that drops can "float" on a bath of the same liquid if the impact velocity is sufficiently small [Reynolds, 1881].

In cases of droplet-bath impact, as well as droplet-droplet impact, there exists

a parameter regime where droplets bounce completely (Figure 3-1). The bouncing-coalescence threshold is often characterized by a critical We that depends sensitively on all parameters in the problem [Tang et al., 2019]. Droplet bouncing on an undisturbed interface at variable impacting angles was first studied in detail by [Jayaratne and Mason, 1964] experimentally. They were able to determine a relationship between the drop radius, impact speed, and impact angle at which the bouncing-coalescence threshold occurs between uncharged drops. Building on the work of [Gopinath and Koch, 2001], [Bach et al., 2004] studied droplet impact of small ($R \leq 50$ μm) aerosol droplets impacting a fluid bath. They developed a rarefied gas model to describe the dynamics of the gas layer separating the droplet and bath, and used an inviscid potential flow model to describe the transfer of energy from the droplet to the bath during impact. The authors determined that the criterion for drop bouncing is more sensitive to gas mean-free path and gas viscosity than to the Weber number itself. [Zou et al., 2011] investigated water droplets bouncing on an air-water interface, and examined the role of bath depth in bounce-back behavior. They determined that the contact time was independent of the impact velocity for a large range of Bond numbers. [Wu et al., 2020] used a drop-on-demand generator to study the bouncing of water droplets, developed a model for the maximum penetration depth, and compared it to their experimental study. They varied the droplet diameter, and found that the maximum rebound height decreased with increasing diameter. An experimental work utilizing three different fluids was completed by [Zhao et al., 2011]. They chose water, 1-propanol, and ethanol as the working fluids and found good agreement in measured contact times to [Jayaratne and Mason, 1964]. Also, they determined that the contact time of the droplet was relatively independent of the impact velocity, similar to that found by [Richard et al., 2002] for a droplet impacting a non-wetting, dry surface. In the variety of experimental work on this particular problem, the scaling for contact time t_c of the droplet appears to be mostly independent of We, except at very low We [Zhao et al., 2011, Zou et al., 2011, Wu et al., 2020]. Additionally, numerous papers report a saturation of translational energy recovery by the droplet at intermediate We, as measured by the coefficient of restitution

α [Jayaratne and Mason, 1964, Bach et al., 2004, Zhao et al., 2011, Zou et al., 2011, Wu et al., 2020]. These observations have not yet been fully explained nor their parametric dependencies clearly elucidated to the best of the current authors' knowledge. This motivates the development of a first principles model that can accurately and efficiently describe the dynamics of both the droplet and the fluid bath over the physically relevant parameter regime.

The multi-scale hydrodynamics present in these impact problems creates significant challenges for numerical simulations, and all but eliminates analytical solutions to these problems. [Wagner, 1932] proposed the first theoretical study of an object impacting on an inviscid, incompressible fluid, utilizing linearized free-surface kinematic and dynamic conditions to develop a theory that decomposed the fluid domain into two parts, one where the applied pressure is unknown but the interface shape is known, and vice versa. The so-called Wagner theory was extended to a solid of revolution by [Schmieden, 1953] and eventually to three dimensions by [Scolan and Korobkin, 2001]. These models assume that the working fluid is ideal, and thus any waves generated upon impact are not subject to viscous dissipation. [Dias et al., 2008] derived a theory to include the effects of weak damping in free surface problems, which appear as leading order corrections in the free surface boundary conditions. The inclusion of damping in this method provides a mechanism for the waves generated by impact to decay in time. The [Dias et al., 2008] theory is valid in the weakly viscous regime and represents a rigorous derivation of a linearized free surface model first proposed by [Lamb, 1895].

More recently, [Galeano-Rios et al., 2017, Galeano-Rios et al., 2021a] applied the quasi-potential model of [Dias et al., 2008] to free surface impact problems and solves the problem of the unknown, time evolving contact region through the use of a so-called "kinematic match". In the kinematic match framework, the free surface shape within the region of contact is determined by the geometry of the problem, and the extent of this region can be computed with the use of a tangency boundary condition. The model in [Galeano-Rios et al., 2017] worked well in determining the trajectory of the droplet in some cases, however neglected any deformations of the

droplet. [Blanchette, 2016, Blanchette, 2017] modeled the impact of a droplet onto a still and oscillating bath, where a simplified version of the kinematic match concept was used by assuming that the shape and radial extent of the pressure distribution in the contact region are known *a priori*. Additionally, droplet deformations were modeled as a vertical spring or as an octahedral network of springs and masses. For still bath impacts, only very limited direct comparison to experimental measurements were made, with mixed success. [Moláček and Bush, 2012] developed a quasi-static model for a droplet impacting on a non-wetting rigid solid surface with fixed curvature. They compared this quasi-static model to a dynamic model that described the droplet-air interface using spherical harmonics derived from a balance of surface, kinetic, and potential energies and found good agreement between the two at low We numbers, as compared to experiments and the model of [Okumura et al., 2003]. However, these models do not predict the energy transfer and time dependent waves on a fluid bath. [Terwagne et al., 2013] wrote a linear mass-spring-damper model for a bouncing droplet on a vertically oscillated bath. Similarly, this model assumed that the bath surface was non-deformable. Additionally, [Moláček and Bush, 2013] studied silicone oil droplets bouncing on a vertically oscillated bath and developed linear and logarithmic spring models to classify bouncing dynamics. While efficient to solve, these models require the input of free parameters determined from experimental data and thus cannot independently predict bouncing metrics such as the coefficient of restitution or contact time. Other linear spring-type models have been proposed in the literature, but again such models generally rely on fitting parameters obtained from experimental data or direct numerical simulation [Sanjay et al., 2022]. Direct numerical simulations of free surface impact problems have been completed in other recent works [Pan and Law, 2007, He et al., 2015, Sharma and Dixit, 2020, Fudge et al., 2021], and provide very good results, even in regimes presently inaccessible to experiments. From these simulations the droplet shape, trajectory, and waves, as well as the flow within the droplet and bath, can be captured and analyzed in detail. However, due to the high computational cost of these free surface flow problems, the vast parameter space encompassed by this problem renders large

sweeps impractical for direct simulation, and leaves much to be understood about the overall dynamics over a more complete space.

In this work, we develop an efficient model that accurately predicts the trajectory of the impacting droplet, the instantaneous droplet shape, and the transient waves generated on the bath interface by impact, without any adjustable parameters. First, we use the Navier-Stokes equations with linearized free surface conditions and include viscosity as leading order corrections to these boundary conditions, which holds in the limit of large Re. We then derive a set of ordinary differential equations to describe the motion of the bath interface. The droplet shape is modeled by another set of ordinary differential equations that govern the weakly-damped oscillation of individual modes on the droplet interface that hold for small Oh. Both the bath and droplet models are the result of linearizing about their undeformed states, and thus we anticipate best agreement when deformations are small. The bath and drop models are coupled using a single-point kinematic match condition and evolved simultaneously in time. We validate this model with new experimental data as well as direct numerical simulations. We then apply the validated model over a wide range of parameters where the relative influence of the hydrodynamic, surface tension, and gravitational forces on the rebound behavior of the bouncing droplet will be elucidated.

3.2 Experimental Methods

3.2.1 Experimental setup

A series of droplet impact experiments were conducted utilizing two working fluids: deionized water and silicone oil with viscosity of 5 cSt. A drop-on-demand generator is used to reliably produce droplets with a maximum variation in the diameter of less than 1% [Ionkin and Harris, 2018]. This device, along with a schematic of the experimental setup is shown in Figure 3-2(a). The drop generator is entirely 3D printed, with the exception of a small piezoelectric disk, hardware, and connective tubing. The deformation of the piezoelectric disk due to an applied voltage pulse acts to ex-

pel fluid through a small nozzle. As the fluid exits the nozzle, the piezoelectric disk relaxes, initiating pinch off of the droplets. The droplets then fall under the action of gravity toward the bath. Two visualizations of droplet impact and rebound are shown in Figures 3-2(b) and 3-2(c). The drop generator is mounted on a 3D-printed translation stage, allowing for repeatable changes to the impacting velocity via height increases of the droplet generator. Directly underneath the drop generator is a 3D printed fluid bath. The bath is 70 mm in width and length, and 50 mm deep. The impact location was 25 mm from the front wall of the bath. This impact location allowed for consistent focus above and below the free surface yet was still sufficiently far from the front panel that the waves created during impact do not have time to reflect and interact with the droplet during contact. For the water experiments, the front and rear walls are constructed using polystyrene that has an equilibrium contact angle of 87.4° [Ellison and Zisman, 1954]. Being close to 90°, this creates a negligibly small meniscus that allows for detailed photography of the impact from the side [Galeano-Rios et al., 2021a]. For the silicone oil experiments, we use a shorter bath window panel, constructed of extruded acrylic and a thin transparent plastic sheet. The bath was brim-filled to the height of the acrylic window panel, such that the contact line was pinned with angle held at approximately 90°. The drops are imaged using a high-speed camera (Phantom Miro LC 311) and illuminated by a Phlox LED-W back light. Video data is taken at 10,000 frames-per-second (fps) with an exposure time of 99.6 μs.

3.2.2 Experimental procedure

Care must be taken to ensure that both the fluid interface and the fluid in the reservoir of the drop generator are contaminant-free, as dust or surfactants can modify the physics involved. Prior to each experiment, the bath and tubing are thoroughly cleaned with an isopropyl alcohol solution, flushed with deionized water, and then left to dry in a fume hood with particulate filtering for 30 minutes. The drop generator and nozzle are cleansed with an ethanol solution, and then flushed with deionized

Table 3.1: Relevant parameters and their range of values in our experimental study.

Parameter	**Symbol**	**Definition**	**Value**
Impact speed	V_0	–	$20 - 100\,\mathrm{cm/s}$
Droplet radius	R	–	$0.035\,\mathrm{cm}$
Density (water)	ρ	–	$0.998\,\mathrm{g/cm^3}$
Surface tension (water)	σ	–	$72.2\,\mathrm{dynes/cm}$
Kinematic viscosity (water)	ν	–	$0.978\,\mathrm{cSt}$
Density (silicone oil)	ρ	–	$0.96\,\mathrm{g/cm^3}$
Surface tension (silicone oil)	σ	–	$20.5\,\mathrm{dynes/cm}$
Kinematic viscosity (silicone oil)	ν	–	$5\,\mathrm{cSt}$
Gravitational acceleration	g	–	$981\,\mathrm{cm/s^2}$
Weber Number	We	$\rho V_0^2 R/\sigma$	$0.5 - 8.0$
Bond Number	Bo	$\rho g R^2/\sigma$	$0.017 - 0.056$
Ohnesorge Number	Oh	$\mu/\sqrt{\sigma R \rho}$	$0.006 - 0.057$
Reynolds Number	$Re = \sqrt{We}/Oh$	$\rho V_0 R/\mu$	$15 - 280$

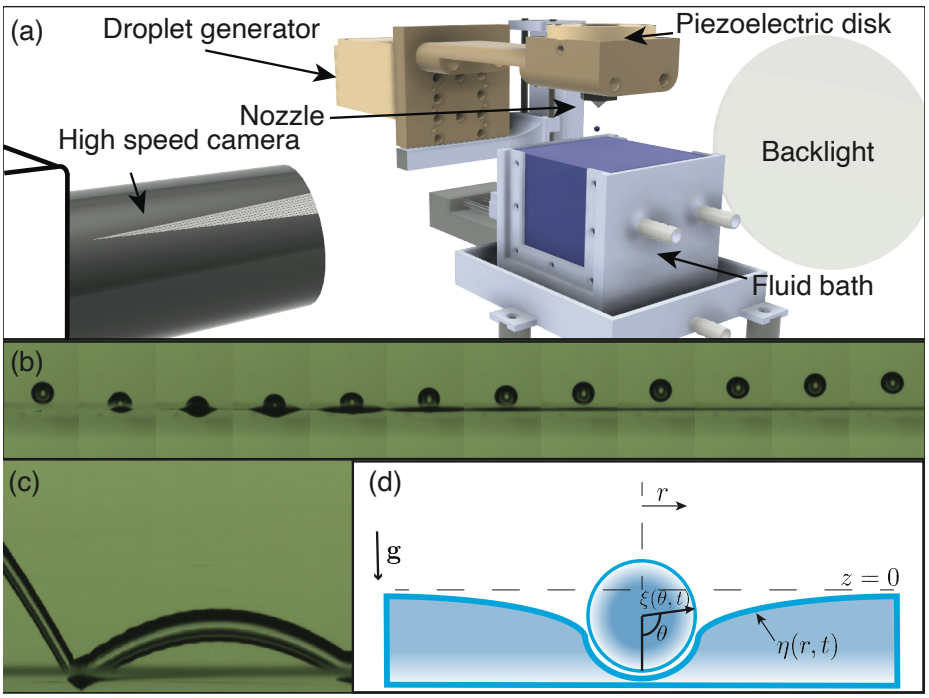

Figure 3-2: (a) A rendering of the experimental setup. (b) Experimental montage of impact of a deionized water droplet on a bath of the same fluid. Images are spaced 0.7 ms apart. (c) Spatiotemporal diagram of a deionized water droplet bouncing. The image is constructed by taking a single pixel wide stripe of the raw video footage, and plotting time along the x-axis. Panels (b) and (c) correspond to an impact of deionized water on a bath of the same fluid with $We = 0.7$, $Bo = 0.017$, and $Oh = 0.006$. (d) Schematic of the problem.

water for 5 minutes. Gloves are worn at all times to minimize contamination. The drop generator is controlled by an Arduino Uno board, with a simple H-bridge circuit initiating the voltage switching of a DC power supply [Ionkin and Harris, 2018]. The fluid within the bath is periodically flushed, approximately after every 15 droplet impacts to reduce surface contamination [Kou and Saylor, 2008]. Overflow from the flushing is caught by a small lip in the bottom of the bath, which is then drained to a waste container. There are two syringes connected to the bath, which allow for fine adjustments of the equilibrium bath depth after flushing.

We collect experimental data for the top and bottom of the droplet during free flight. During contact, we track the height of the top of the droplet and that of the center of the deformed free surface. Since the air layer that separates the droplet and the interface is negligibly thin relative to the scale of the droplet, we assume that this point is also effectively the location of the droplet's south pole. Just after the drop rebounds off the surface, the axisymmetric surface wave created by the impact is partially in the line of sight of the camera, and obscures the bottom of the droplet for a brief period during take-off. These data points have been omitted from the bottom trajectory when reported. The raw video data are post-processed using a custom Canny edge detection software implemented in MATLAB 2021b, which quantifies the droplet trajectory, and then computes impact parameters and bouncing metrics [Galeano-Rios et al., 2021a].

There are several metrics of interest in our study, which we define in what follows. The maximum penetration depth, δ, of a bounce is defined as the position of the bottom of the droplet at the lowest point in the trajectory (relative to the undisturbed interface height). In our experiment, the contact time, t_c, is defined as the time duration from which the top of the droplet crosses the height $z = 2R$ to the time the top of the droplet returns to that height. Due to the nature of visualisation setup it was impossible to determine precisely when the droplets lost physical contact with the fluid; however, this always occurred before the top of the drop returned to the level $z = 2R$. Each bounce was also characterised by its coefficient of restitution, α, which is defined here as the negative of the normal exit velocity, V_e, divided by the

normal impact velocity, V_0. This parameter ranges between 0 and 1, and is related to the momentum exchange during impact.

In order to determine the contact time (t_c) and coefficient of restitution (α), a parabola was fitted using a least-squares method to the incoming and outgoing trajectories, separately, with at least 30 data points prior to impact and at least 40 data points following rebound. The analytical form of the parabolic fit was then used to extrapolate the time at which the sphere crosses the still air-water interface height (which corresponds to a root of the parabolic function). The derivative of the parabolic fit function was then computed analytically and its value evaluated at these times in order to calculate the impact speed, V_0, and exit speed, V_e [Galeano-Rios et al., 2021a].

3.3 Linearized quasi-potential fluid model

In this section, we develop a model for droplet impact on a flat fluid interface from first principles. First, we use the linearized Navier-Stokes equations to model the flow within the bath and the shape of the bath interface. Then, we use an orthogonal function decomposition of the bath model to derive a single set of linear ordinary differential equations (ODEs) that govern the bath mode amplitudes. We then write a similar model for the droplet interface, which reduces to another set of linear ODEs governing droplet mode amplitudes. Finally we propose a model for the pressure distribution and its extent acting on the bath and droplet during contact, couple the two sets of ODEs together using a single-point kinematic match condition, and solve the system implicitly using standard numerical integration techniques. A schematic of the problem is illustrated in Figure 3-2(d).

3.3.1 Bath interface model

The present work models the bath interface dynamics using a linearized, quasi-potential flow model following the work of [Galeano-Rios et al., 2017]. For the problem of a droplet impacting on a free interface, the Navier-Stokes equations govern

the flow generated by the bath-droplet interaction. Assuming the flow to be incompressible, isothermal, and Newtonian, we can define the fluid velocity vector $\mathbf{u} = [u, v, w]^T = \nabla\phi + \nabla \times \Psi$ and the bath interface shape $\eta = \eta(r, \Theta, t)$, Here, ϕ is the scalar potential and Ψ is the vector stream function. We then linearize the governing equations and boundary conditions about the undisturbed free surface $z = 0$. Utilizing the arguments presented in [Galeano-Rios et al., 2017] and [Dias et al., 2008], we can recast the governing equations to be

$$\nabla^2\phi + \partial_z^2\phi = 0, \quad z \leq 0, \tag{3.1}$$

$$\partial_t\eta = \partial_z\phi + 2\nu\nabla^2\eta, \quad z = 0, \tag{3.2}$$

$$\partial_t\phi = -g\eta - 2\nu\partial_z^2\phi + \frac{\sigma}{\rho}\kappa - \frac{p_s}{\rho}, \quad z = 0, \tag{3.3}$$

$$\partial_z\phi = 0 \text{ at } z = h_0. \tag{3.4}$$

Here, $p_s(r, \Theta, t)$ is the contact pressure, g is the gravitational acceleration, $\kappa(r, \Theta, t) = \nabla^2\eta$ is twice the linearized mean curvature of the interface, h_0 is the depth of the undisturbed bath, and ρ, σ, $\nu = \mu/\rho$ are the fluid density, surface tension, and kinematic viscosity, respectively. In this notation, $\partial_{()}$ denotes partial differentiation with respect to the variable given in the parenthesis and $\nabla^2 = \partial_r^2 + (1/r)\partial_r + (1/r^2)\partial_\Theta^2$. The tangential stress boundary conditions are automatically satisfied in these approximations. As detailed in [Galeano-Rios et al., 2017], this leading order theory is valid in the weakly viscous limit when $Re = \sqrt{We}/Oh \gg 1$. A similar bath model was used by [Blanchette, 2016, Blanchette, 2017], although the viscous correction term was not included in the dynamic boundary condition (3.3).

We assume that the impact occurs in a bath of some viscous fluid which is subject to two boundary conditions, $\partial_n\phi = 0$ on the walls of the bath and $\partial_z\phi = 0$ on the bottom of the bath, where n is the outward facing normal of the walls of the bath [Benjamin and Ursell, 1954]. The former condition implies that $\partial_n\eta = 0$ on the walls of the container. These conditions correspond physically to a bath where the working fluid maintains a constant contact angle of 90° at the walls, and has no-flux boundary conditions along the walls and bottom. Applying these conditions to the governing

system of equations, an orthogonal function expansion for the unknowns η, ϕ and their derivatives can be explicitly written.

The orthogonal basis functions $S_{j,m}(r,\Theta)$ ultimately must satisfy

$$(\nabla^2 + k_{j,m}^2)S_{j,m} = 0, \tag{3.5}$$

inside of any bounding curve K that exists on the border of the bath and the boundary condition of $\partial_n S_{j,m} = 0$ on K. $k_{j,m}$ are the eigenvalues of the system, and depend on the choice of the physical domain of the problem. If the boundary curve K is a circle, the functions become $S_{j,m} = J_j(k_{j,m}r)\cos j\Theta$. Here J_j are Bessel functions of the first kind and $k_{j,m}$ are the solutions to $J_j'(k_{j,m}b) = 0$, where b is the bath radius. If we further assume the problem to be axisymmetric, then we can choose $j = 0$, and write $S_{0,m} = J_0(k_{0,m}r)$. For convenience, we define $k_{0,m} = k_m$ henceforth. We then can express the free surface elevation as

$$\eta(r,t) = \sum_{m=0}^{\infty} a_m(t)J_0(k_m r). \tag{3.6}$$

We then re-write all of the unknowns of the axisymmetric bath problem, using (3.1) and (3.2), as a function of the time varying amplitude coefficients, $a_m(t)$:

$$\eta(r,t) = \sum_{m=0}^{\infty} a_m(t)J_0(k_m r), \tag{3.7}$$

$$\kappa(r,t) = \nabla^2\eta = -\sum_{m=0}^{\infty} k_m^2 a_m J_0(k_m r), \tag{3.8}$$

$$\phi(r,z,t) = \sum_{m=0}^{\infty} \left(\frac{da_m}{dt} + 2\nu k_m^2 a_m\right) J_0(k_m r)\frac{\cosh k_m(h_0+z)}{k_m \sinh k_m h_0}. \tag{3.9}$$

In order to arrive at the final equations of motion for the free surface, we take the decompositions (3.7-3.9) and substitute them into the dynamic boundary condition

(3.3). Rearranging, we find

$$\sum_{m=0}^{\infty}\left[\frac{d^2a_m}{dt^2}+4\nu k_m^2\frac{da_m}{dt}+\left(\frac{\sigma k_m^2}{\rho}+g\right)k_m\tanh\left(k_m h_0\right)a_m\right]J_0(k_m r)=-\frac{p_s}{\rho}k_m\tanh\left(k_m h_0\right). \tag{3.10}$$

Each wave mode in the bath is described by a forced, damped harmonic oscillator equation.

3.3.2 Droplet interface model

Additionally, we wish to recover a similar set of equations that describe the gravity-capillary waves present in the droplet, and then couple these equations to the motion of the bath. The full derivation of the droplet oscillation model can be found throughout prior works [Lamb, 1924] [Tsamopoulos and Brown, 1983, Courty et al., 2006] [Chevy et al., 2012, Balla et al., 2019] and is briefly summarized below.

We begin by utilizing spherical harmonics to decompose the droplet radius in a spherical domain,

$$\xi(\theta,t)=R+\sum_{l=1}^{\infty}\sum_{n=-l}^{l}\beta_l^n(t)Y_l^n(\cos\theta,\phi), \tag{3.11}$$

with $Y_l^n=P_l^n(\cos\theta)e^{in\phi}$. Due to the axisymmetry of the problem, we set $n=0$ and the spherical harmonics reduce to associated Legendre polynomials, $P_l^n(\cos(\theta))$. For convenience, we write $\beta_l^n=\beta_l$ henceforth. We assume that the velocity potential takes the same form as the decomposition of the interface [Lamb, 1924, Balla et al., 2019]. We then turn to an energy conservation equation of the form

$$\frac{dT}{dt}=\dot{W}-\epsilon, \tag{3.12}$$

with $T=K+G$, $\dot{W}$, and ϵ, as the total energy (sum of the kinetic energy K and potential energy G) of the drop, the rate of work done on the droplet interface, and the viscous dissipation, respectively. We can express T, $\dot{W}$, and ϵ using the decomposition (4.1), and substitute these expressions into the conservation of energy equation. Then, utilizing the linearized kinematic boundary condition yields a set of

forced, damped harmonic oscillators that describe the amplitude of each individual spherical mode,

$$\sum_{l=1}^{\infty}\left[\frac{d^2\beta_l}{dt^2}+2\alpha_l\frac{d\beta_l}{dt}+\omega_l^2\beta_l\right]=\sum_{l=1}^{\infty}\left[-\frac{(2l+1)l}{2\rho R}\int_0^{\pi}p_s(\theta)\sin\theta P_l(\cos\theta)d\theta+g\delta_{1l}\right]. \tag{3.13}$$

We drop the sums, and arrive at the result

$$\frac{d^2\beta_l}{dt^2}+2\alpha_l\frac{d\beta_l}{dt}+\omega_l^2\beta_l=-\frac{(2l+1)l}{2\rho R}\int_0^{\pi}p_s(\theta)\sin\theta P_l(\cos\theta)d\theta+g\delta_{1l}, \tag{3.14}$$

with

$$\alpha_l=(2l+1)(l-1)\frac{\mu}{\rho R^2}, \tag{3.15}$$

$$\omega_l^2=l(l-1)(l+2)\frac{\sigma}{\rho R^3}, \tag{3.16}$$

and δ_{1l} is the Kronecker delta function. This model is valid in the weakly viscous limit, when $Oh \ll 1$. An extension of the free droplet model to arbitrary Oh can be found in other prior works [Chandrasekhar, 2013, Moláček and Bush, 2012, Miller and Scriven, 1968].

3.3.3 Pressure forcing during impact

There is still an additional unknown in the bath mode (3.10) and drop mode (3.14) equations: the applied pressure distribution $p_s(r,t)$. This is generally a function of the properties of the fluid medium, the impacting speed of the object, the shape of the impacting object, and the motion of the gas that surrounds the fluid. However, in this work, we will assume that the viscosity of the ambient gas is small relative to the fluid bath such that the flow within the small air film is negligible, and the pressure acts solely to apply an upwards hydrodynamic force on the droplet. In non-dimensional terms, we can construct two additional restrictions for our model, $\rho_g/\rho \ll 1$ and $Oh_g = \mu_g/\sqrt{\rho\sigma R} \ll Oh$ following prior work [Moláček and Bush, 2012]. In the current experimental and direct numerical simulation work, $\rho_g/\rho \sim \mathcal{O}(10^{-3})$ and

$Oh_g \sim \mathcal{O}(10^{-4})$, thus the influence of these two additional parameters is indeed negligible. We have verified this for our typical experimental parameters through DNS, and find that both a 4-fold increase and decrease in the ambient density and viscosity from air properties at standard temperature and pressure (STP) produces negligible changes to the trajectory, instantaneous shape of the droplet, and free surface shape throughout the interaction of the droplet and bath (see section (3.6)).

The radial extent of the pressure distribution is generally unknown for impact problems, and constitutes an additional problem that we must solve. In the present work, we assume that this unknown pressure distribution takes the form

$$p_s(r,t) = \frac{F(t)}{\pi R^2} H_r(r/r_c(t)) \tag{3.17}$$

where F is the instantaneous magnitude of the contact force, evaluated at $r = 0$ and H_r is an assumed spatial profile of the pressure in the contact region. For this distribution, we can use a function that resembles the true shape of the pressure distribution during contact. The contact region, A_c, will be assumed to a simply-connected disk, following [Galeano-Rios et al., 2017] and [Korobkin, 1995]. This allows us to write a single unknown $r_c(t)$ to fully describe the temporal evolution of this region of contact. [Blanchette, 2016, Blanchette, 2017] used a fixed parabolic pressure shape function

$$H_r(r) = \begin{cases} C\left(1 - (\frac{r}{R})^2\right) & r \leq R \\ 0 & r > R. \end{cases} \tag{3.18}$$

Here, C is the constant magnitude of the pressure at $r = 0$ and R is the undeformed radius of the droplet. [Blanchette, 2016, Blanchette, 2017] chose the value of the magnitude C such that $\int_0^b p_s r dr = \pi R^2$. Thus, the pressure acting on the bath interface in the respective models had a constant pressure shape function H_r for all times during contact. However, simulation results from [Galeano-Rios et al., 2017, Galeano-Rios et al., 2021a] show that the shape of the pressure distribution at the surface of a fluid bath due to an impacting, non-wetting sphere is flatter and more similar to a top-hat function for most times, and that the spatial extent of the distribution

changes continuously with time during impact. Additionally, for a droplet impacting on a solid surface, the pressure in the air film has been inferred by [de Ruiter et al., 2015b]. The air film thickness during a bounce was measured using interferometry and the pressure estimated using a lubrication model. The film pressure in both the impacting and rebounding regimes is approximately uniform, with deviations from uniformity only near the edge of the film. In related work, the impact pressure between a droplet and a wettable solid substrate has been studied extensively by [Mandre et al., 2009] and [Mani et al., 2010], and their results indicate that the impact pressure increases sharply near the contact line, likely a consequence of the decreased air film thickness in that region. For the case of droplets bouncing on a deep pool, [Tang et al., 2019] measured the air film thickness and found the film thickness to be significantly more uniform in both impacting and rebounding stages for We values similar to those explored in the present work, presumably as a result of the deformability of the substrate and impactor. Our predictions from direct numerical simulation similarly suggest a more uniform air film thickness for the present problem, and a nearly uniform pressure profile during all stages of rebound.

We will use a simple polynomial that resembles a smoothed top hat in this work, with

$$H_r(r/r_c(t)) = \begin{cases} C\left(1 - (\frac{r}{r_c(t)})^6\right) & r \leq r_c(t) \\ 0 & r > r_c(t). \end{cases} \tag{3.19}$$

In order to remain consistent with our linearization, we do not allow r_c to exceed R. Requiring that the integral of the pressure over the contact area is $F(t)$, we find

$$\int_0^b H_r(r/r_c) r \; dr = \frac{R^2}{2}, \tag{3.20}$$

which sets the constant C in the pressure shape function $H_r(r/r_c)$. Our bath model relies on the decomposition of the fluid motion into a linear superposition of infinitely many waves with wavenumbers k_m. Therefore, we apply a similar decomposition to this pressure function $p_s = \sum_{m=0}^{\infty} d_m J_0(k_m r)$. Since we are working in a cylindri-

cal domain, we will choose the zeroth order Bessel function of the first kind as our orthogonal basis function, and thus the d_m are the Fourier-Bessel coefficients of the function H_r,

$$d_m = \frac{2}{(bJ_1(k_m))^2} \int_0^b H_r(r) r J_0(k_m r) dr, \tag{3.21}$$

with the domain extending from $r = [0, b]$. The reconstruction of the top-hat function in Fourier-Bessel space converges too slowly to be of practical use [Storey, 1968], also noted by [Blanchette, 2016], and as such we use a polynomial expression that resembles a smoothed top hat. Additionally, we tested higher order polynomials (corresponding to a larger flat region), and found increasingly poor convergence behavior, similar to that of the top hat (see section (3.6) for a case study on the sensitivity of the results to the choice of shape function). The ultimate choice of shape function used here thus represents a practical compromise.

Substituting in the definition of the pressure (3.17) into (3.10), performing the Fourier-Bessel decomposition, we find

$$\frac{d^2 a_m}{dt^2} + 4\nu k_m^2 \frac{da_m}{dt} + \left(\frac{\sigma k_m^2}{\rho} + g \right) k_m \tanh(k_m h_0) a_m = -\frac{F}{\rho \pi R^2} d_m k_m \tanh(k_m h_0), \tag{3.22}$$

which govern the evolution of bath wave modes m. Similarly, substituting the pressure (3.17) into (3.14), we write

$$\frac{d^2 \beta_l}{dt^2} + 2\alpha_{l,0} \frac{d\beta_l}{dt} + \omega_{l,0}^2 \beta_l = -\frac{F}{2\pi \rho R^3} c_l (2l+1) l + g \delta_{1l}. \tag{3.23}$$

The coefficients c_l result from the mode decomposition of the projection of the pressure into spherical space,

$$c_l = \int_0^\pi H_r(\theta) \sin(\theta) P_l(\cos\theta) d\theta, \tag{3.24}$$

which naturally arise in the derivation of equation (3.14). Additionally, the definition of the pressure (3.17) reduces the governing equation of the $l = 1$ "translational" mode to

$$\frac{d^2 \beta_1}{dt^2} = -\frac{F}{m} + g, \tag{3.25}$$

which clearly governs the droplet center of mass motion $\beta_1 = -z_{cm}$. Evidence from the simulations of [Galeano-Rios et al., 2017] indicates that impact trajectory is very sensitive to the instantaneous size of the contact area. Utilizing a constant pressed area for the pressure, as done in [Blanchette, 2016], does not produce results that compare well with experiment, particularly for cases of small We. Figure 3-12 in section (3.6) depicts how the choice of this pressure shape function modifies the predicted trajectory of the droplet for typical experimental parameters. The trajectory is largely insensitive to the choice of pressure shape function, but incorporating a time-dependent contact radius is essential for agreement. The method for determining both $F(t)$ and $r_c(t)$ are discussed in the next section.

3.3.4 Modeling contact

The contact force $F(t)$ is determined through the use of a "1-Point" kinematic match (1PKM) condition. Essentially, we enforce contact only at a single point; the center of our axisymmetric domain. Thus, the additional constraint can be written as

$$\eta(r=0,t) = z_{cm}(t) - \xi(\theta=0,t) = \sum_{m=0}^{\infty} a_m(t) = z_{cm}(t) - \left(R + \sum_{l=2}^{\infty} \beta_l(t) \right). \quad (3.26)$$

This additional constraint allows us to determine the unknown contact force $F(t)$. Contact between the droplet and the bath ends when the magnitude of the contact force as predicted by the kinematic match becomes negative. We note that this 1PKM model is a significant simplification of the full kinematic match successfully used to study related impact problems [Galeano-Rios et al., 2017, Galeano-Rios et al., 2019, Galeano-Rios et al., 2021a]. The full kinematic match predicts the evolution of the contact area and the contact pressure distribution (without requiring an assumption for H_r) by imposing natural geometric and kinematic constraints, essentially considering additional equations to solve at each time step. The algorithm requires iteration at each time step, and the minimization of a tangency boundary condition is used to determine the correct contact area and pressure shape.

Lastly we turn to the unknown contact radius $r_c(t)$. By not restricting the de-

formations of the bath and droplet interface with the use of additional tangency and distributed kinematic match conditions, we find that the results of our simulation consistently produce interfacial shapes that cross each other. The amount of overlap between the two interfaces is generally small, for instance, in the comparison in Figure 3-3 the maximum overlap is less than $0.05R$. However, we can use the predictions from both interfacial models to determine the exact location where the two interfaces cross and separate, and use this as the instantaneous radius of contact $r_c(t)$. Thus, at each time, contact between the bath and drop is ensured at both $r = 0$ and $r = r_c(t)$. In order to enforce contact within the entirety of the contact region, a full kinematic match would be required - this circumvents the need for any assumptions on the pressure profile shape, but is substantially more computationally expensive. Our contact radius criterion is similar to that of the numerical model presented in prior work on droplet rebound from solid substrates [Moláček and Bush, 2012]. While this method is unphysical, it yields accurate predictions for the contact radius as compared to DNS (Figure 3-3(b)).

3.3.5 Summary

Choosing a timescale of $t_\sigma = \sqrt{\rho R^3/\sigma}$ (with $\tau = t/t_\sigma$), a length scale of R, and a force scale of $2\pi\sigma R$ (with $f = F/2\pi\sigma R$), we recast the governing equations in

non-dimensional form as

$$\eta(r,\tau) = \sum_{m=0}^{M} a_m(\tau) J_0(k_m r), \tag{3.27}$$

$$\xi(\theta,\tau) = 1 + \sum_{l=2}^{L} \beta_l(\tau) P_l(\cos\theta), \tag{3.28}$$

$$\frac{d^2 a_m}{d\tau^2} + 4Oh\, {k_m}^2 \frac{da_m}{d\tau} + \left({k_m}^2 + Bo\right) k_m \tanh\left(k_m h_0\right) a_m = -2 f d_{m,0} k_m \tanh\left(k_m h_0\right), \tag{3.29}$$

$$\frac{d^2 \beta_l}{d\tau^2} + 2Oh\,(2l+1)(l-1)\frac{d\beta_l}{d\tau} + l(l-1)(l+2)\beta_l = -f c_l (2l+1) l + Bo\,\delta_{1l}, \tag{3.30}$$

$$\frac{d^2 z_{cm}}{d\tau^2} = \frac{3}{2} f - Bo\,, \tag{3.31}$$

$$\eta(0,\tau) = z_{cm}(\tau) - \xi(\theta = 0, \tau). \tag{3.32}$$

Equations (3.29) and (3.30) describe the evolution of the bath and droplet oscillation modes, respectively. Equation (3.31) governs the vertical motion of the droplet's center of mass. Equation (3.32) couples these equations all together, with $r = 0$ as the single point of "contact" enforced between the droplet and the bath and allows for determination of the unknown $f(\tau)$. These equations are solved using standard ordinary differential equation numerical integration techniques. The shape of the bath and droplet can be reconstructed at any time t via the sums in equations (3.27) and (3.28), respectively.

The complete model is valid when $Re = \sqrt{We}/Oh \gg 1$ and $Oh \ll 1$. Also, since the model is linearized about the undeformed state, we anticipate it to hold when deformations remain small, further suggesting $Bo \ll 1$ and $We \ll 1$. However, we later demonstrate through direct comparison with experiment and DNS that the model remains predictive even for moderate We.

3.3.6 Numerical methods

We solve these equations using a backward Euler method, ensuring a minimum of 100 time steps within the inertio-capillary time t_σ. An implicit method was chosen, following [Galeano-Rios et al., 2021a], as the instantaneous size of the pressure distribution acting on both the droplet and bath at the next time step is unknown. Treating the pressure explicitly on either the droplet or the bath can lead to non-physical behavior in the system. We used $M = 150$ modes for the bath interface and $L = 55$ modes for the droplet interface. These values were determined by running simulations of a $We = 0.7$, $Bo = 0.017$, $Oh = 0.006$ impact and assessing convergence as described in what follows. First, we kept the number of droplet modes fixed at $L = 15$ and increased the number of bath modes from 30 to 500 in increments of 25. Then, the simulation was run again, fixing the number of bath modes at 75 and increasing droplet modes from 15 to 200. Sufficient convergence was determined if the maximum absolute value of the difference in center of mass trajectories during contact changed by less than 1%. Finally, both the droplet and bath number of modes were increased simultaneously, and convergence was still observed. These values are similar to comparable to those found in [Blanchette, 2016] ($M = 200$, using sine functions as the basis functions in a square bath), and [Moláček and Bush, 2012] ($L = 150$, but found good accuracy in comparison to experimental data at $L = 20$). Additionally, once mode convergence was determined, we decreased the time step of the simulation in increments until time step convergence was similarly reached using the same criterion. Unexpectedly, in a fully-converged simulation, there is a time step threshold below which the algorithm results in unstable oscillations in the magnitude of $F(t)$. This time step threshold is typically at least three orders of magnitude smaller than t_σ. This apparent instability deserves awareness and future attention, but does not affect the results presented in the present work. The bath size was set to $b = 25R$ which was determined to be sufficiently large such that reflected waves did not influence the droplet during impact. In order to find the instantaneous contact radius, we take two line segments from the reconstruction of the droplet and

bath interface shapes. From these we can write a linear system of equations for four unknowns: the (r, z)-pair of the intersection location, the normalized distance from the starting point of the first line segment to the intersection, and the normalized distance from the starting point of the second line segment to the intersection [Schwarz, 2022]. We then loop over every line segment to find every intersection. We take the largest of this set as $r_c(t)$. In the reconstructions of the interfaces at each time step, at least 5000 points are used in both θ and r to ensure that error is minimized. All code associated with the implementation of the model is available at `https://github.com/harrislab-brown/BouncingDroplets`.

3.4 Results

In this section, we first present the results of a direct comparison between experiment, quasi-potential model, and DNS for a single impact We. Then, we vary We for two working fluids, and compare the results of the three different impact metrics between the experiment, DNS, and model. Having validated the model and DNS, we then run sweeps over Bo and Oh to deduce the effect that these non-dimensional constants have on droplet rebound metrics, and compare predictions to existing experimental data sets available in the literature.

3.4.1 Comparison to experiment

We first consider a single impact of a deionized water droplet with $R = 0.35$ mm. A direct comparison of the trajectory results of the model, DNS, and the experiments is depicted in Figure 3-3(a). We find excellent agreement for the top, center of mass, and bottom trajectories between the experiment, quasi-potential model, and DNS. Additionally, we make a direct comparison between the quasi-potential model and the DNS for the prediction of the radius of contact in Figure 3-3(b). During impact, the quasi-potential model accurately predicts the instantaneous contact area, as well as the maximum contact area. The DNS, which accurately resolves the air film, shows that a finite region of contact is already developed prior to impact. At

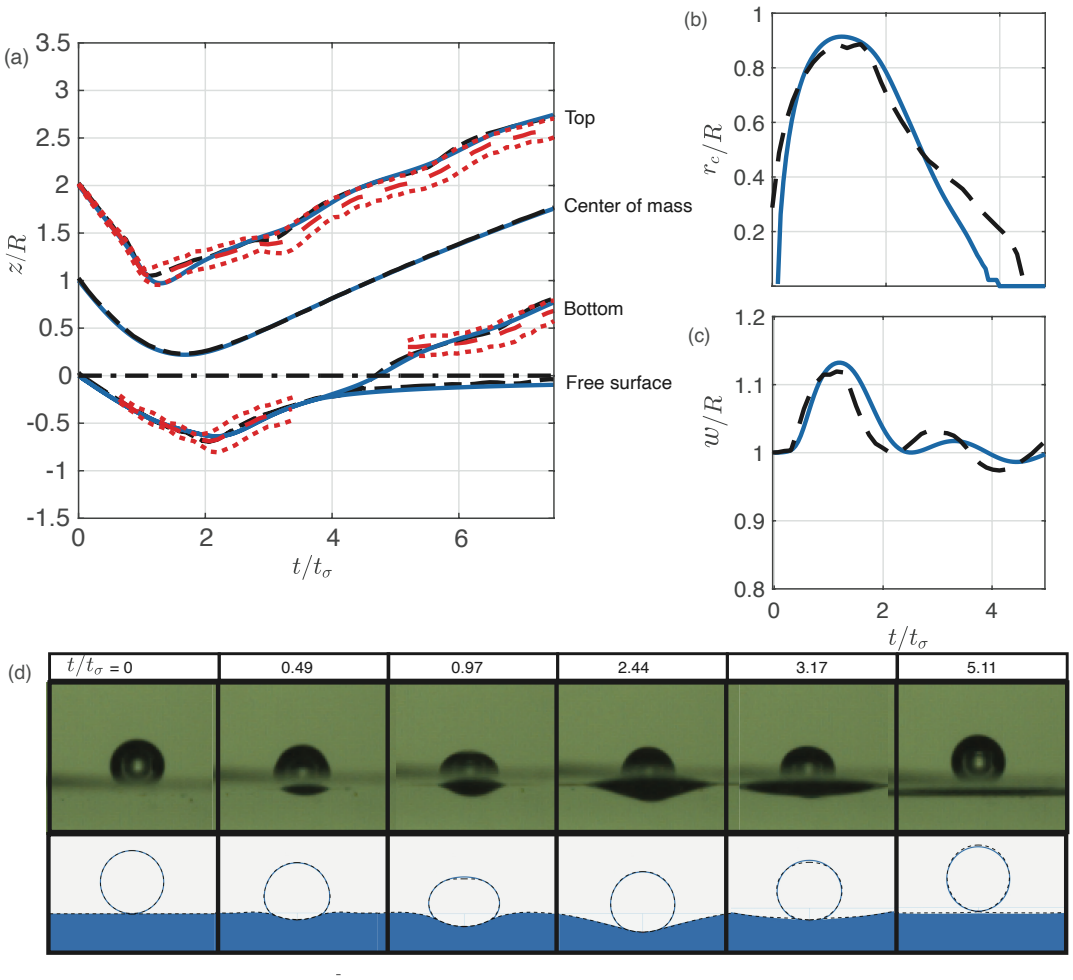

Figure 3-3: Rebound of a $R = 0.35$ mm deionized water droplet from a bath of the same fluid corresponding to $We = 0.7$, $Bo = 0.017$, and $Oh = 0.006$. (a) Trajectory comparison between the experiment (red dashed line with typical variation shown as dotted red lines), DNS (black dashed line), and quasi-potential model (blue solid line). (b) Instantaneous contact radius, normalized by the undeformed radius R, as a function of time for the quasi-potential model and DNS. (c) Maximum width of the droplet w, as a function of time for the quasi-potential model and DNS. (d) Comparison of droplet shape between experiment, DNS, and quasi-potential model. Video supplementary material is available.

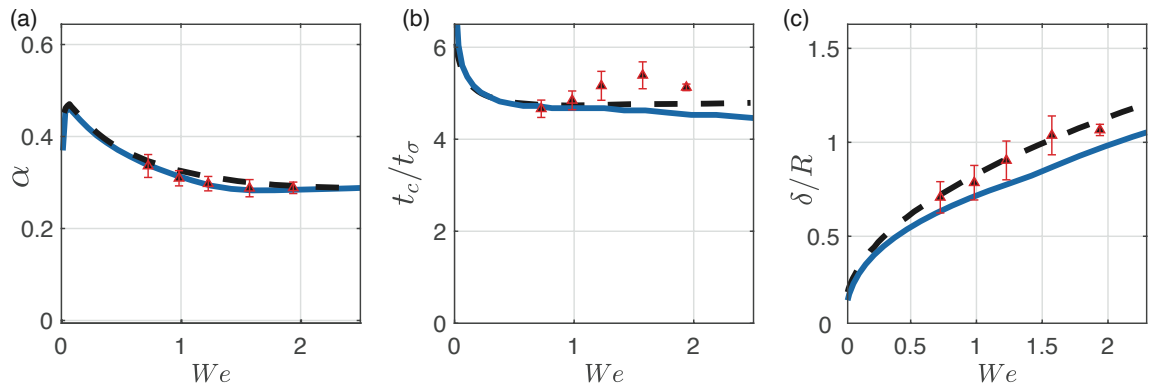

Figure 3-4: (a) Coefficient of restitution, (b) contact time, and (c) maximum penetration depth for a $R = 0.35$ mm deionized water droplet rebounding from a bath of the same fluid as a function of We (with $Bo = 0.017$ and $Oh = 0.006$). Error bars on experimental data points are quantified as the standard deviation of at least 5 experimental trials. Predictions of the quasi-potential model are shown as blue solid lines, DNS as black dashed lines.

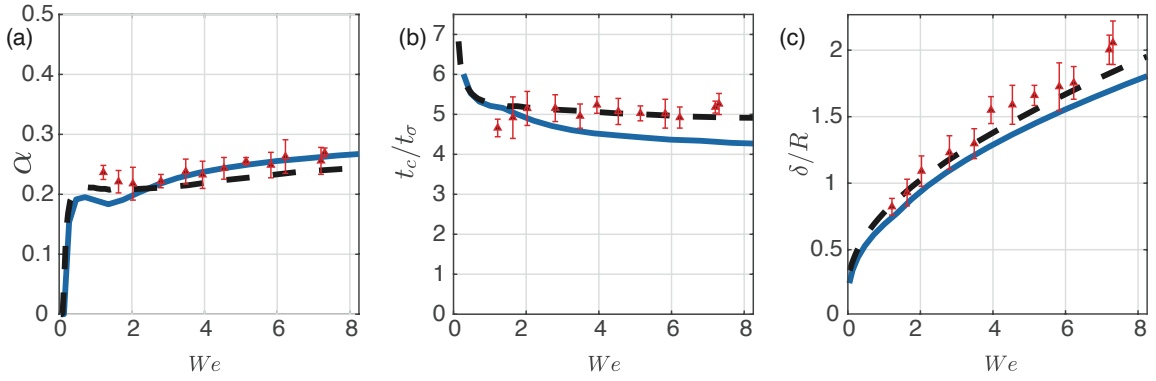

Figure 3-5: (a) Coefficient of restitution, (b) contact time, and (c) maximum penetration depth for a $R = 0.35$ mm 5 cSt oil droplet rebounding from a bath of the same fluid as a function of We (with $Bo = 0.056$ and $Oh = 0.058$). Error bars on experimental data points are quantified as the standard deviation of at least 5 experimental trials. Predicitions of the quasi-potential model are shown as blue solid lines, DNS as black dashed lines.

$t/t_\sigma > 3$, the two models deviate from each other, and this is most likely due to suction effects as the droplet pulls away from the surface. These effects cannot be predicted while neglecting the motion of the air, as in the current quasi-potential model, however do not appear consequential to the overall droplet trajectory. A comparison between the two models for the maximum width of the droplet is depicted in Figure 3-3(c). As is the case with the contact radius, the deformation of the droplet in the DNS occurs slightly before that of the quasi-potential model, as the pressure in the film is already building prior to contact. This leads to an overall phase shift of the oscillation between the models, although the maximum value for the deformation between both models remains in very good agreement. We also compare the droplet and interface shape between the experiments, DNS, and linearized model can be seen in the panels of Figure 3-3(d). The impact is depicted for six different instants during contact. As the droplet deforms the interface, a capillary wave travels from the impact location to the north pole of the droplet. The collapse of this wave onto itself occurs just before the time of maximum deformation of the bath, and corresponds to the maximum deformation of the droplet. After this time, surface tension in the bath begins to act to restore the equilibrium, having redistributed some of the initial impact energy in the form of interfacial waves. The droplet remains mostly spherical as the bath relaxes, until contact is lost. During free flight, the droplet oscillates as an underdamped harmonic oscillator, dissipating additional energy through viscosity. Both the DNS and experiment show slightly stronger oscillations in the top of the droplet as compared to the model, to the point which the instantaneous slope at the top is occasionally close to zero. Overall, the DNS and quasi-potential model are in excellent agreement and predict the bath shape, droplet shape, and droplet trajectory with high accuracy for these parameters.

As we begin to explore the larger parameter space, we consider three different output parameters for the rebounds, namely: coefficient of restitution (α), contact time (t_c), and maximum surface deflection (δ). As mentioned in section 3.2.2, given the experimental difficulty to accurately determine the time of surface detachment of the droplet, contact time, t_c, is defined in the experiment as the interval between

the two instances when the north pole of the droplet crosses level $z = 2R$ and the coefficient of restitution, α, is defined as minus the ratio of the vertical velocities at those times. For the model and DNS, we define the metrics in the same way, but when the center of mass of the droplet crosses $z = R$. This is chosen because a measure on the center of mass more accurately describes the total translational energy transfer from the droplet. However, in comparing the results from the model and DNS using both top (measured at $z = 2R$) and center of mass (measured at $z = R$), we found a typical difference of 2% for α and t_c/t_σ in the silicone oil experiments, and 5% for the same parameters in the deionized water experiments.

Figure 3-4 outlines a variation of impact We for a deionized water droplet onto a water bath. In this parameter sweep, the coefficient of restitution generally decreases as the We number is increased, eventually saturating at a value just below 0.3, and remaining nearly independent of the We number thereafter. The contact time also decreases as the We number is increased, but remains relatively independent of the We number at an earlier value, consistent with results found for impact on a solid surface [Richard et al., 2002] and for previous experiments for impact on a deep pool [Zhao et al., 2011]. The maximum penetration depth increases monotonically with We. We find good agreement between the model, DNS, and experiments with regard to the restitution coefficient, contact time, and maximum surface deflection for these experiments. Additionally, the quasi-potential model is able to predict α for the entire range of experiments. Both the model and DNS slightly underpredict the dimensionless contact time at intermediate We, yet do agree with the experimental data for $We \leq 1$. The quasi-potential model also underpredicts the penetration depth and contact time at moderate We. Nonlinear effects associated with larger deformation have been neglected in this model, and are most likely the cause of this discrepancy.

Figure 3-5 depicts a We number variation using 5 cSt silicone oil. In non-dimensional terms, this represents an increase in both the Bo and Oh numbers. Similar trends in t_c/t_σ and δ are observed for the silicone oil as compared to the deionized water. However, α tends to generally increase with We in this case, as

opposed to water which showed the opposite trend. The quasi-potential model accurately predicts α for almost the full range of We, with slight underprediction for $We < 2$. Similar to the water case, the quasi-potential model underpredicts t_c/t_σ and δ at intermediate We, with the DNS capturing these metrics more accurately. Although not verified experimentally, the model and DNS predict that droplets with very, very low We numbers cease to return to their original height at all. Note that $We \leq 0.5$ is challenging to explore experimentally for these parameters, as pinch off of the droplets from the generator induces oscillations that need to dampen out prior to impact. The short free flight time and low viscosity of these extremely low We cases mean that there is still oscillation present at impact, which has been shown in prior work to influence rebound dynamics in related droplet impact problems [Biance et al., 2006, Yun, 2018].

3.4.2 Inertio-capillary limit

The validated quasi-potential model can now be used to explore other sets of parameters. In particular, based on the assumptions of the model, we expect the model to remain accurate (and even perhaps improve) for cases of even smaller Bo and Oh than achieved in experiments. As a grounding point, we first turn our attention to the pure inertio-capillary limit, where both gravitational and viscous effects are ignored (i.e. $Bo = 0$ and $Oh = 0$). This case reduces the number of dimensionless parameters that describe the physical problem to just one: the We number. The results in the inertio-capillary limit are presented in Figure 3-6, along with the droplet and bath shape predictions for various We. The penetration depth δ^* increases monotonically with increasing We, as found for both the water and oil experiments. Additionally, the contact time t_c^* decreases before becoming mostly independent of We. However, in this limiting case, the coefficient of restitution α^* monotonically decreases with We and does not have a local maximum in the restitution coefficient, and droplets can even retain a majority of their impacting energy at sufficiently low We. Furthermore, the coefficient of restitution then remains nearly independent of We above $We > 1.75$, and is predicted to saturate to a value of approximately $\alpha_s^* = 0.31$.

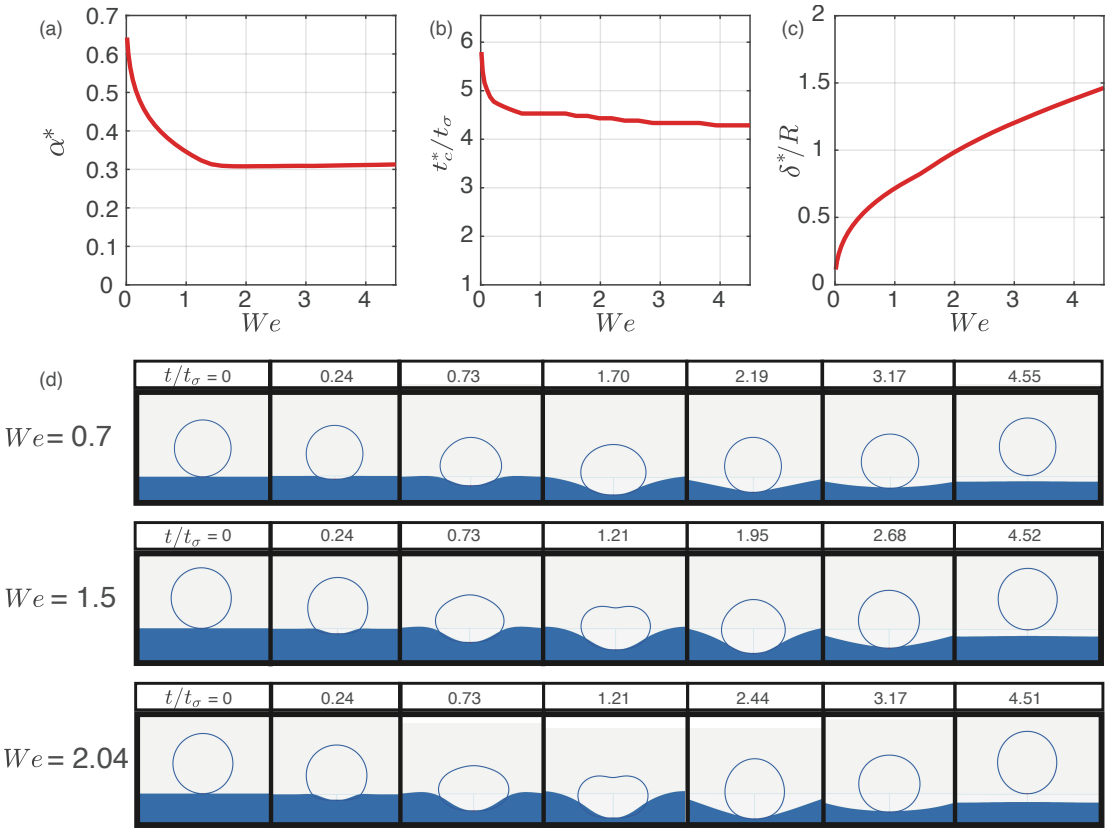

Figure 3-6: (a-c) Rebound parameters of a droplet in the inertio-capillary regime (as denoted by the asterisk). d) Droplet and bath shape in the pure inertio-capillary regime ($Bo = 0$, $Oh = 0$) for three different We.

3.4.3 Influence of viscosity and gravity

We then individually probe the parameter space by increasing either Bo or Oh. These variations are presented in Figures 3-7 and 3-8. The result of increasing Bo, while keeping Oh constant (yet negligibly small), is depicted in Figure 3-7. At low values Bo, the curves converge to the inertio-capillary limit as presented in the prior section. For a given We, the coefficient of restitution decreases monotonically with Bo, until eventually ceasing to return to its original height. At intermediate values of Bo the curves exhibits an interesting non-monotonic dependence on We, with a local maxima at finite We. Furthermore, the contact time of the droplets is predicted to increase with increasing Bo. These qualitative trends are consistently reproduced by the DNS, with satisfactory quantitative agreement between the quasi-potential model and DNS for $Bo \lesssim 0.1$. For larger Bo, and for the highest We cases explored, the model generally underpredicts the coefficient of restitution as compared to the DNS.

Increasing Oh while keeping Bo negligibly small, is shown in Figure 3-8, and also predicts a monotonic decrease in the restitution coefficient, with curves converging to the inertio-capillary limit for small Oh. Unlike the Bo variation, the shape of the curve remains relatively unchanged. The non-dimensionalized contact time changes only marginally, even over an order of magnitude increase in Oh. Very similar trends are predicted by DNS, with models diverging quantitatively beyond $Oh \gtrsim 0.1$, consistent with a breakdown of the weakly viscous modeling assumptions. For larger Oh, the quasi-potential model overpredicts the coefficient of restitution and underpredicts the contact time, as compared to the DNS.

3.4.4 Scaling analysis

In this subsection we present scaling arguments to rationalize the dependence of the coefficient of restitution on Bo and Oh detailed in Figures 3-7(a) and 3-8(a), respectively. As revealed in the prior section, at a fixed We, the coefficient of restitution decreases monotonically from the inertio-capillary limit (Fig. 3-6(a)) as either Bo or Oh is increased. Due to the number of parameters involved, in order to proceed, we

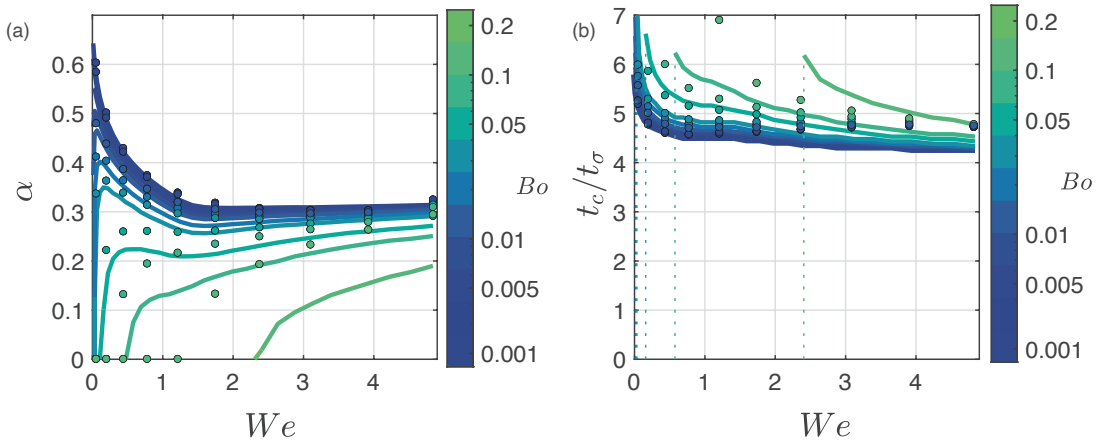

Figure 3-7: (a) Coefficient of restitution and (b) contact time as a function of the Bond number Bo. Viscous effects are set to be finite but negligible, with $Oh = 6 \times 10^{-4}$. Predicitions of the quasi-potential model are shown as solid lines, DNS as individual markers. The vertical dashed lines in panel (b) reference the critical We for each Bo below which droplets do not bounce.

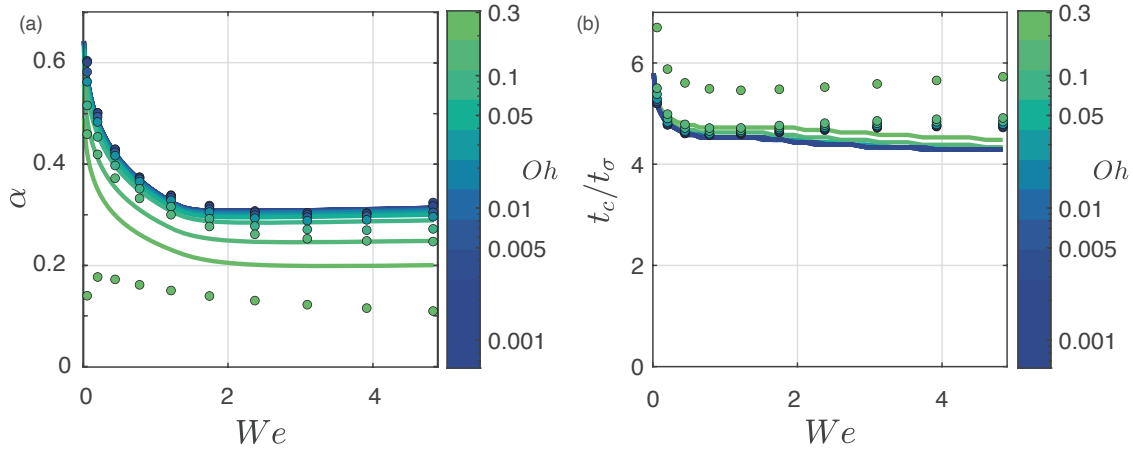

Figure 3-8: (a) Coefficient of restitution and (b) contact time as a function of the Ohnesorge number Oh. Gravitational effects are set to be finite but negligible, with $Bo = 1 \times 10^{-3}$. Predicitions of the quasi-potential model are shown as solid lines, DNS as individual markers.

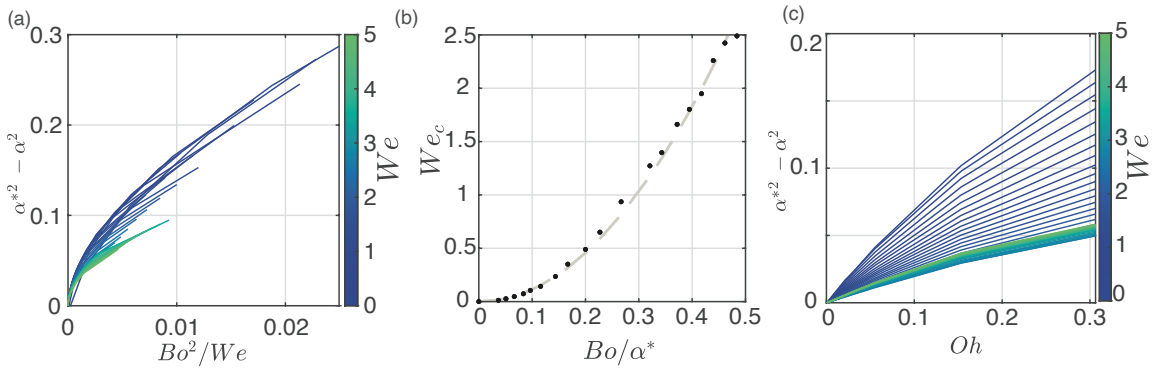

Figure 3-9: (a) Coefficient of restitution predictions from the quasi-potential model for $Oh = 6 \times 10^{-4}$ (Fig. 3-7(a)) re-plotted as informed by the scaling in equation (3.35). (b) Critical We as a function of Bo; the points are predictions from the quasi-potential model, and the dotted curve is a parabolic fit ($We_c = 11.43 Bo^2/\alpha^{*2}$) consistent with the scaling in equation (3.36). (c) Coefficient of restitution predictions from the quasi-potential model for $Bo = 1 \times 10^{-3}$ (Fig. 3-8(a)) re-plotted as informed by the scaling in equation (3.37).

will assume that this additional energy transfer (or loss) due to weak gravitational (or viscous) effects is independent of the baseline energy transferred (ΔE^*) in the inertio-capillary limit. Mathematically, this assumption can be expressed in the form

$$\alpha^2 = \frac{E_o - \Delta E^* - \Delta E_{g,\mu}}{E_o} = \alpha^{*2} - \frac{\Delta E_{g,\mu}}{E_o}, \tag{3.33}$$

or

$$\alpha^{*2} - \alpha^2 = \frac{\Delta E_{g,\mu}}{E_o}, \tag{3.34}$$

where $E_o = \frac{2\pi}{3}\rho R^3 U^2$ is the initial droplet kinetic energy, and $\Delta E_{g,\mu}$ is the supplemental energy transferred or lost due to gravity or viscosity, respectively. In what follows, we propose scalings for these energies.

Since gravity is a conservative force, increases in Bo must lead to an overall increase in the deformation (and subsequent oscillation) of the bath and droplet. In the capillary-dominated regime, the gravity-induced deformation can be estimated to scale with $\rho R^3 g/\sigma$, corresponding to an additional surface energy scaling as $\Delta E_g \sim \rho^2 R^6 g^2/\sigma$. Normalizing this estimate by the incident kinetic energy, we find an addi-

tional fractional energy transfer to droplet-bath deformations that scales as

$$\frac{\Delta E_g}{E_o} \sim \frac{\rho R^3 g^2}{\sigma U^2} = \frac{Bo^{\,2}}{We}. \tag{3.35}$$

Motivated by equations (3.34) and (3.35), we re-plot the data from Figure 3-7(a) in 3-9(a), and find a satisfactory collapse. In particular, the scaling in equation (3.35) correctly predicts that bounces at lower We will be more heavily penalized in terms of their coefficient of restitution. This inequity rationalizes the observed non-monotonic behavior of α with We predicted for intermediate Bo (Figure 3-7(a)). Furthermore, equations (3.34) and (3.35) suggest a scaling for the "critical" Weber number We_c below which the droplet ceases to bounce (i.e. $\alpha^2 < 0$):

$$We_c \sim \frac{Bo^2}{\alpha^{*2}}. \tag{3.36}$$

The data for the critical Weber number as predicted by the quasi-potential model is shown in Figure 3-9(b), and follows the proposed scaling in equation (3.36). We note that [Blanchette, 2016] observed a parabolic scaling for the critical Weber number with Bo in prior work, also finding this threshold to be largely independent of Oh.

Upon the inclusion of viscosity, there is viscous dissipation in the drop and bath that now occurs during contact. The rate of viscous energy dissipation (per unit volume) can be estimated to scale as $\mu(\nabla \mathbf{u})^2 \sim \mu U^2/R^2$. Assuming a characteristic fluid volume R^3, we find a viscous energy dissipation rate that scales like $\mu U^2 R$. As demonstrated in the prior sections, the contact time $t_c \sim t_\sigma$, and thus we may estimate the additional fractional energy loss during contact as

$$\frac{\Delta E_\mu}{E_o} \sim \frac{\mu}{\sqrt{\sigma \rho R}} = Oh. \tag{3.37}$$

Replotting the data from Figure 3-8(a) in 3-9(c) shows that apart from the very lowest We cases considered, the curves collapse to a single line, confirming the proposed scaling. For all We, the curves are approximately linear in Oh (consistent with equation (3.37)) with the slope evidently depending on We for the smallest We

cases.

In summary, our models predict an additional energy transfer (or loss) over the pure inertio-capillary limit when gravitational (or viscous) effects are introduced. Our scaling suggests that gravity leads to additional deformations in the system, coming at an additional energetic cost. Additionally, viscosity provides a mechanism for energy dissipation, occuring over the finite contact time of the droplet. Computing the various energies directly in direct numerical simulations (such as in [Sanjay et al., 2022]) may provide additional insight to the remaining subtleties present in the data.

3.4.5 Comparison to prior literature data

In the works of [Jayaratne and Mason, 1964, Bach et al., 2004, Zhao et al., 2011, Zou et al., 2011, Moláček and Bush, 2013] there is a reported saturation in the energy transfer from the drop during rebound at modest $We > 1$ and low Oh, as measured by the coefficient of restitution. The exact value of the saturation restitution coefficient does seem to vary however, from 0.2 in [Moláček and Bush, 2012] for more viscous drops, to 0.3 in [Bach et al., 2004, Zhao et al., 2011], to as low as 0.1 [Zou et al., 2011] for large Bo impact scenarios. Remarkably, recent experiments on rebound of liquid metal droplets in viscous media also showed similar values of the coefficient of restitution with $\alpha = 0.27$ [McGuan et al., 2022]. A similar saturation is also observed in our experimental results presented herein, with water droplets generally bouncing higher that the 5 cSt silicone oil droplets. In Figure 3-10, we overlay existing available experimental data for α from numerous sources and find that the prediction from the quasi-potential model accurately captures much of this data. The grey line represents the extrapolation of data from non-normal impacts by [Jayaratne and Mason, 1964] over the range of We reported in their work. Data from the experiments completed in this work utilizing 5 cSt silicone oil and deionized water are included with error bars. The historical data generally indicates a decrease in α with Bo, as captured by the present model. Despite the relatively large variation in Oh, the experimental data appear to match the results of the quasi-potential model quite well.

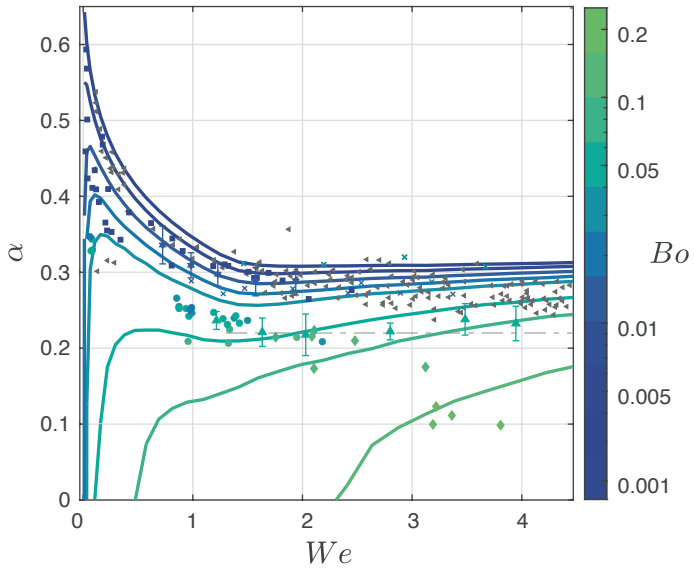

Figure 3-10: Comparison of model Bo predictions (Figure 3-7(a)) to existing literature data where We was reported. The grey markers represent data points where the exact value of Bo is unknown, with only ranges reported. The grey dot-dashed line represents the extrapolation of oblique impact data to normal impacts by [Jayaratne and Mason, 1964]. Data from the experiments completed in the present work are included with error bars. Studies included here are summarized in Table 3.2

Furthermore, the existing experimental data (apart from a small number of outlying points) is well bounded by the inertio-capillary limit presented earlier. This curve thus appears to define a universal upper bound on the coefficient of restitution for a droplet rebounding from a deep pool of the same fluid as a function of We, regardless of any other parameters.

There is substantially less data available on contact times for low Oh impacts, but when reported they generally take values within the range of $4-6t_\sigma$ [Zhao et al., 2011, Moláček and Bush, 2013, Wu et al., 2020].

3.5 Discussion

In this work we have used a combination of custom experiments, state-of-the-art direct numerical simulation techniques, and a new quasi-potential model to study the bouncing of millimetric droplets on a deep bath of the same fluid in the inertio-capillary

Table 3.2: Relevant publications and ranges of droplet parameters for experiments presented in Figure 3-10.

Publication	Bo	Oh	**Symbol**
[Bach et al., 2004]	$5 \times 10^{-5} - 2 \times 10^{-4}$	$0.31 - 0.69$	■
[Zhao et al., 2011]	> 0.005	> 0.008	◁
[Zou et al., 2011]	$0.10 - 0.48$	$0.0026 - 0.0039$	◇
[Moláček and Bush, 2013]	$0.027 - 0.2$	$0.16 - 0.27$	○
[Wu et al., 2020]	$0.016 - 0.04$	$0.005 - 0.006$	×
This work	$0.017 - 0.056$	$0.006 - 0.058$	△

regime. Weakly viscous models for the bath and droplet interfaces are coupled to one another through the use of a simplified kinematic matching condition, and allow us to make accurate predictions for the droplet trajectory and time-dependent droplet and bath shapes. Furthermore, the quasi-potential model is relatively efficient to compute and uses only standard off-the-shelf algorithms, resolving multiple bounces in less than 5 minutes on a standard desktop computer. Both the quasi-potential model and DNS are demonstrated to accurately predict the coefficient of restitution, contact time, and maximum surface deflection, validated by direction comparison to experiments with two different working fluids.

Starting from the inertio-capillary limit (where both gravitational and viscous are negligible) in the model, as we increase Bo, we see a decrease in the coefficient of restitution and an increase in the contact time. Additionally, a local maximum develops in α at low We as Bo increases. As Bo increases further, droplets cease to return to their original height. Furthermore, as Oh is increased away from the inertio-capillary limit, a simpler, monotonic decrease in α is observed, with the contact time remaining almost unchanged for the much of the Oh range explored in this work. By further comparison with DNS, the complete model is shown to hold in the limit of small Bo and Oh, and up to intermediate We, provided that the influence of the intervening gas layer that inhibits coalescence on the overall dynamics is minimal. These trends can be rationalized using simple scaling arguments, with gravity resulting in additional droplet-bath deformations (and thus energy transfer), and viscosity providing a mechanism for energy dissipation in the fluid during contact. Addition-

ally, the model can be used to connect much of the existing experimental data on this particular topic. In particular, the inertio-capillary limit appears to define an upper bound on the possible coefficient of restitution for droplet-bath impact, with the value depending only on the Weber number, and saturating to a near constant value at intermediate We.

The related problem of a droplet impactor rebounding off a solid surface has been considered in numerous previous works [Anders et al., 1993, Richard and Quéré, 2000, Richard et al., 2002, Gilet and Bush, 2012]. The dependence of the coefficient of restitution on the Weber number has previously been reported [Biance et al., 2006, Aussillous and Quéré, 2006, Gilet and Bush, 2012], and the trend observed in these studies is similar to what is found in this work for low We and low Bo, however the typical values of restitution coefficients in these studies are significantly larger. This is likely due to the fact that a large portion of the initial droplet energy in the present case is carried away by surface waves excited in the fluid bath. Our general findings also have many similarities with the investigation of [Galeano-Rios et al., 2021a], in which non-wetting spheres impact and rebound from a water bath. In particular, the general trends for maximum penetration depths and contact times are consistent with the present work. However, spheres with density most similar to that of water show a consistent monotonic increase in the coefficient of restitution with increasing We rather than saturating to a near constant value for the case of droplet-bath rebound. Furthermore, at intermediate We, coefficients of restitution can take values as high as $\alpha \approx 0.5$, distinctly greater than otherwise equivalent droplet-bath rebounds considered in the present work. Evidently, the nature of the impactor and substrate influences the subtle energy transfer mechanisms across these different capillary rebound problems.

The model presented here is highly versatile, with only a single embodiment thereof considered here in terms of target canonical physical scenario. Future work will consider the effect of relative surface tension and viscosity, where the droplets are composed of a different fluid than the bath. Also, in the present work we have specifically selected the size of the bath to be much greater than that of the droplet radius

to eliminate any possible wave reflection and interaction effects. In [Zou et al., 2013], experimental results indicate that reducing the size of the bath (such that the impacting wave on the bath has time to travel to the edge and return to the impact point) can increase the coefficient of restitution with the droplet recovering energy initially lost to waves. Furthermore, the effects of incident droplet or bath deformations could be readily studied, and has been shown to influence bouncing behavior in similar systems [Biance et al., 2006, Yun, 2018]. There are a number of possible additions to the existing model that could expand its reach to other related problems. For instance, the model for the droplet deformation can be extended into a regime where the dynamics of the gas layer does matter, and the gas layer dynamics coupled to the droplet deformation through the use of lubrication equations. The model can also be adapted to non-axisymmetric domains, or to droplet impacts at varying angles of incidence. However, in these cases the full kinematic match should be utilized, as the shape of the pressure distribution would likely change at each time step. Moreover, numerous authors have studied the variety of phenomena that occur when a droplet impacts another droplet [Qian and Law, 1997, Tang et al., 2012]. Droplet-droplet collisions are of extreme importance in combustion science [Jiang et al., 1992] and cloud formation [Grabowski and Wang, 2013], for instance, the general effect of cloud turbulence acts to increase droplet-droplet interaction, and droplet impact and coalescence is postulated as the primary mechanism by which warm rain forms [Grabowski and Wang, 2013]. With such motivation in mind, the present model could be readily extended to cases where equal and unequal sized droplets impact and rebound from one another. Overall, the quasi-potential model developed in this work has the potential to continue to inspire and inform the rich subject of capillary rebounds.

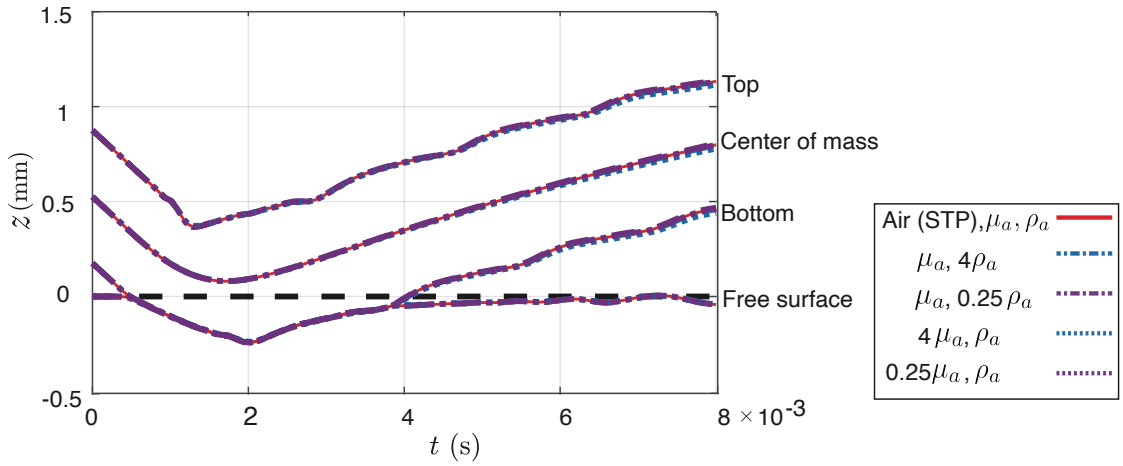

Figure 3-11: DNS predictions of the trajectory of a deionized water droplet with $R = 0.35$ mm in air at $We = 0.7$ (with $Bo = 0.017$, $Oh = 0.006$). The ambient gas density and viscosity are increased and decreased independently by a factor of 4. These simulations are compared to the case with the reference case of air properties at standard temperature and pressure (STP).

3.6 Additional Supporting Information

3.6.1 Influence of ambient gas properties

In order to verify our assumption that the flow within the air layer is negligible to the droplet and bath dynamics in our parameter regime of interest, we run DNS simulations where the ambient gas density and viscosity are varied. First, the gas viscosity is held fixed for air at 21°C and 1 atm and the density is increased by a factor of four, and then decreased by a factor of four, respectively. Then the variation process is repeated for the gas viscosity, with density held fixed. The results of these simulations are presented in Figure 3-11 and are nearly indistinguishable, particularly during contact.

3.6.2 Influence of pressure shape function

Additionally, we tested several pressure shape functions H_r to assess the relative influence of this choice. In the simulations show in Figure 3-12 a parabola, 4th-order,

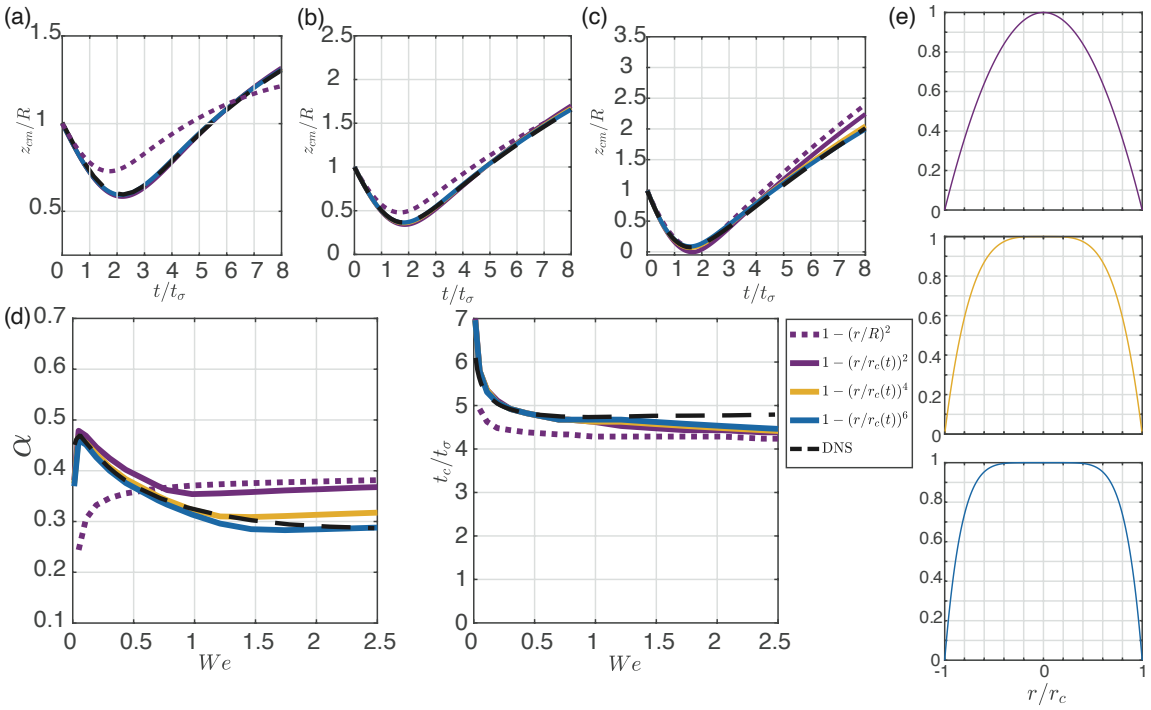

Figure 3-12: Quasi-potential model and DNS predictions for a deionized water droplet with $R = 0.35$ mm corresponding to $Bo = 0.017$ and $Oh = 0.006$. Droplet center of mass trajectories for (a) $We = 0.07$, (b) $We = 0.36$, and (c) $We = 1.36$. (d) Coefficient of restitution α and contact time t_c/t_σ as a function of We. (e) Plots of the pressure shape functions $H_r(r/r_c)$ tested in this figure, shown for reference.

and 6th-order polynomial with time varying contact areas set as described in the modeling section are compared as well as to a parabola with fixed contact radius $r_c(t) = R$. These results all correspond to $Bo = 0.017$ and $Oh = 0.006$ impacts. The parabola with the fixed contact area performs the most poorly, especially at lower impact We. At higher impact We, the fixed radius $r_c(t) = R$ parabolic distribution prediction becomes similar to the time evolving parabolic case. For the simulations presented in this work, the contact radius is defined to have a maximum value of R, as the projection of the pressure distribution onto the undisturbed spherical surface is no longer well defined for $r_c > R$. The value for $r_c(t)$ quickly saturates to R at higher impact We, and the agreement between the constant contact radius and the contact radius model used in the present work improves. Overall, inclusion of a time-varying contact radius appears necessary to capture the correct trends in α and t_c/t_σ over the range of We presented in this work. In addition, as the order of the polynomial increases, the shape of the pressure function more closely resembles a top hat, and the predictions of the model improves as compared to the corresponding DNS. The 6th-order polynomial was ultimately chosen for the present work, as higher polynomials (corresponding to broader flat regions) converged more slowly with only marginal changes in the quantitative predictions.

Chapter 4

Non-wetting Droplet Impact on a Rigid Substrate

4.1 Introduction

The next problem that we will study is where a droplet impacts axisymmetrically on a dry, rigid surface. This case has been studied extensively due to the relatively simple setup of experiments and the wide range of applications. In this experiment, the droplets can either bounce, wet the surface, or splash. It has been demonstrated that the most important factor determining the fate of an impacting droplet in this scenario is actually the surrounding fluid [Driscoll et al., 2010, Mandre et al., 2009, Mani et al., 2010]. The lubricating film that develops has a large pressure gradient toward the edge of the region of contact, and this pressure induces an axisymmetric fluid sheet, called a lamella, that ejects out from the region of impact. The lamella either sticks to the surface, or, if the impact has substantial inertia, breaks up into secondary droplets. These splashes can be modified or even entirely suppressed by controlling the ambient pressure and surface roughness of the substrate [Latka et al., 2012]. Droplets can also bounce off of wettable surfaces [de Ruiter et al., 2015b, Kolinski et al., 2014], via the identical mechanism of droplet bouncing on a pool where a stable air film is created due to drop deformability. However, most work on droplet bouncing on rigid substrates has focused on non-wetting

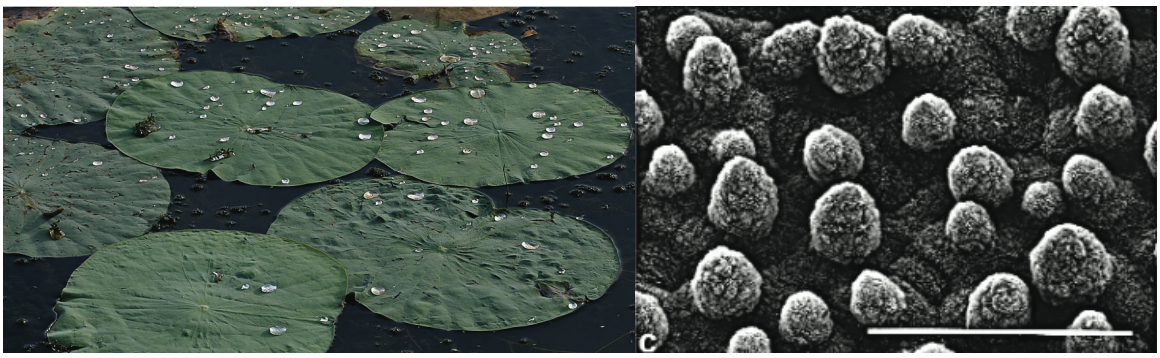

Figure 4-1: *Left*: Large water droplets resting on a lotus leaf. *Right*: Microstructure of the lotus leaf. The small paraboloids of revolution on the surface of the leaf are coated with epiticular wax crystals that help produce a static contact angle of 162° with water. Image from [Neinhuis and Barthlott, 1997], with scale bar of $20\mu m$.

impact or partially wetting impact. There are over 200 known species of plants that have textured micro-structures on their leaves in addition to wax coatings that keep the leaves dry, with the most well known example being the lotus, *Nelumbo nucifera* [Neinhuis and Barthlott, 1997]. These micro-structures are depicted in the right panel of figure 4-1. With advances in understanding of the science of wetting, various surface treatment methods are available to produce surfaces that are effectively non-wetting for a variety of different fluids [Tuteja et al., 2007, Ohkubo et al., 2010, Li et al., 2016, Li et al., 2007, Wang et al., 2020, Yang et al., 2011, Lu et al., 2015]. Typically, there exists two wetting states on a textured substrate, the Cassie-Baxter state and the Wenzel state, depicted in figure 4-2. In the Cassie-Baxter state, surface microstructures act to trap small gas pockets between the drop interface and the surface. This effectively reduces the total contact area of the droplet, and allows the droplet to move freely on the surface. In the Wenzel state, these air pockets have drained, and the drop has fully wet the surface. Now, moving the droplet becomes more challenging, as the surface structures act as "pins", holding the contact line of the droplet in place as the bulk is deformed. In fact, defects as small as 10 nm can pin the contact line, and create contact line dynamics that cannot be fully described by continuum mechanics [Colosqui et al., 2016]. Various methods to make a surface superhydrophobic have been utilized in the literature, from developing micro- and nanostructures on the surface [Wang et al., 2020, Quéré, 2005],

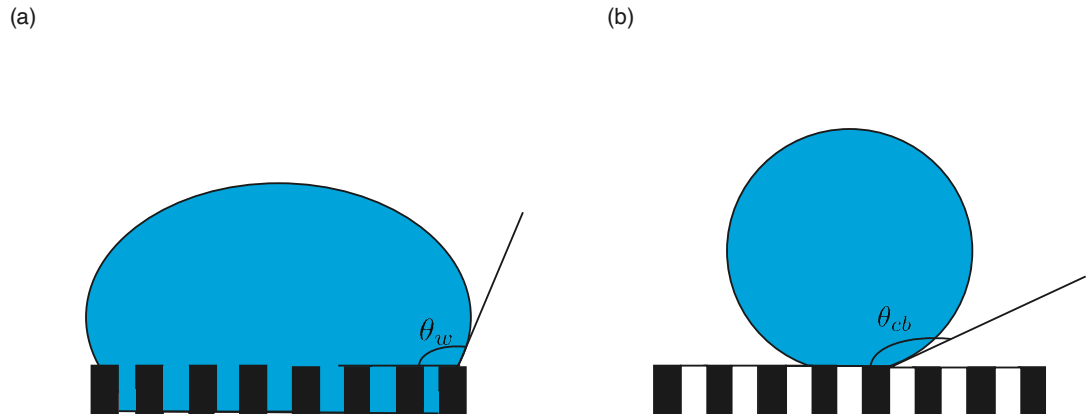

Figure 4-2: Droplets resting on a model surface. Intrinsic surface roughness is represented by rectangular pillars. *Left*: In the Wenzel state, the fluid penetrates the surface layer, creating an equilibrium contact angle θ_w. *Right*: In the Cassie-Baxter state, the interstitial gas is trapped in the surface layer, leading to an equilibrium angle $\theta_{cb} > \theta_w$.

coating the surface with a textured hydrophobic surface layer (typically a wax or Teflon based spray), or possibly even using photocatalytic materials that transform as UV light is applied [Lu et al., 2015, Callies and Quéré, 2005]. These superhydrophobic surfaces are not perfectly non-wetting, but they have been successfully modeled as such in prior work [Galeano-Rios et al., 2021a], and exhibit extremely large equilibrium contact angles $\theta_c > 160°$. Superoleophobic surfaces that prevent wetting of organic liquids are somewhat more difficult to design, as the extremely low surface tension of organic liquids would require a substrate with a surface energy lower than any currently known substance [Tuteja et al., 2007]. However, recent progress has demonstrated that it is possible to make a surface superoleophobic by taking advantage of a different kind of surface structure and coatings [Tuteja et al., 2007, Li et al., 2016]. Droplet impact on these surfaces has been studied extensively [Clanet et al., 2004, Richard and Quéré, 2000, Richard et al., 2002]

There is yet another scenario where non-wetting of droplets can occur, one where no surface treatments are necessary, and that is the well studied Leidenfrost effect. This effect occurs when a fluid comes interacts with a hot surface which is above a critical temperature called the Leidenfrost temperature [Harvey et al., 2021,

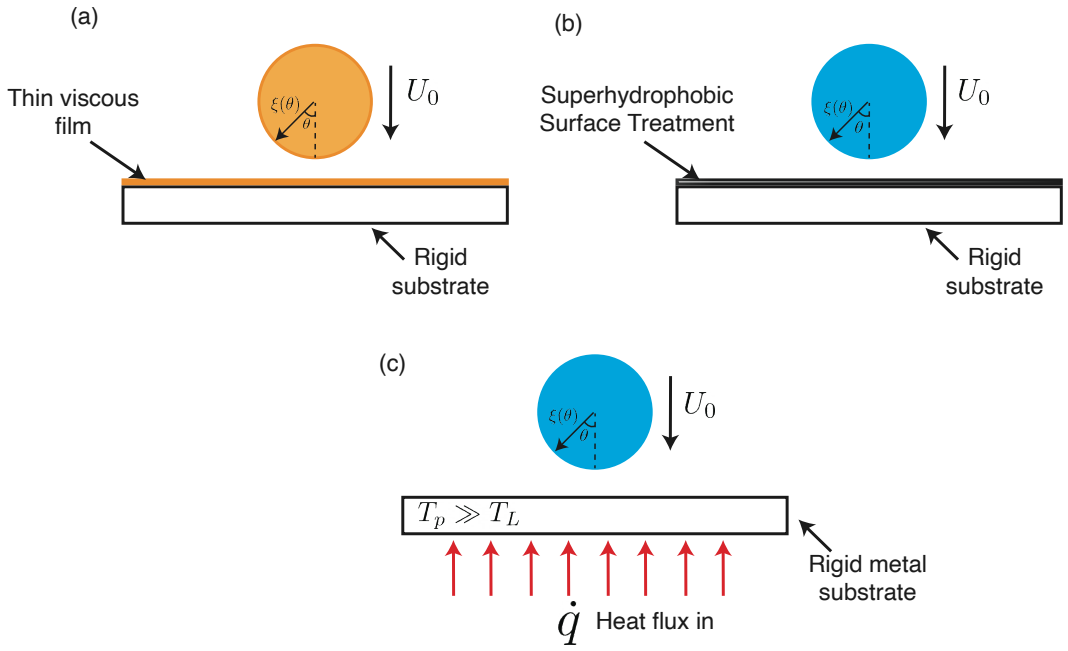

Figure 4-3: Three different "non wetting" impact scenarios considered in this chapter.

Pomeau et al., 2012]. In this scenario, the heat flux from the surface is large enough that some portion of the fluid can levitate on a stable film of its own vapor. Studying the Leidenfrost effect is extremely accessible, and something that almost everyone has experienced but may not be aware of. Most people have tried to check if a pan is hot enough to cook an egg by flicking a little bit of water onto it. Next time you are cooking breakfast, throw some droplets on the pan and watch as the Leidenfrost effect scatters the drops about. These droplets are very stable, lasting for minutes on the hot surface [Biance et al., 2003], much longer than expected as the vapor layer has the secondary effect of insulating the droplet. These droplets can self propel [Wang et al., 2021, Linke et al., 2006], stably oscillate [Ma and Burton, 2018], and bounce repeatedly [Tran et al., 2012, Biance et al., 2006]. Additionally, Leidenfrost droplets can even launch themselves off the surface from rest via pressure fluctuations caused by interfacial instabilities and waves [Graeber et al., 2021]. Some literature has been devoted to understanding the vapor layer which separates the droplet and

surface via interferometry [Pomeau et al., 2012, Burton et al., 2012]. Mathematical models have been written to describe the motion of the droplets, as well as the shapes they take during their lifespan [Sobac et al., 2014, Myers and Charpin, 2009]. There has been work on the so called dynamic Leidenfrost effect, where a non-negligible droplet velocity modifies the required minimum temperature for this effect [Tran et al., 2012]. The bouncing of ethanol droplets at oblique angles off hot surfaces was studied in detail experimentally by [Anders et al., 1993, Karl et al., 1996]. DNS of the problem were presented in [Karl et al., 1996] with excellent agreement to experiments for the droplet shape during impact.

Additionally, droplets of low viscosity silicone fluid impacting on extremely viscous thin films can also bounce [Sanjay et al., 2022, Gilet and Bush, 2012]. The very large viscosity of the fluid in the film and the high energy dissipation rates present due to the small thickness effectively eliminates substrate deformation. Thus, the film acts as non-wetting rigid surface. Another method of creating non-wetting droplets is through the use of hydrophobic powders. Liquid marbles are droplets of water coated in hydrophobic powders [Aussillous and Quéré, 2006, Aussillous and Quéré, 2001]. Common powders utilized in the literature include teflon (PTFE) spheres, glass spheres chemically treated by silanization [Planchette et al., 2012], polyethylene, hydrophobized copper, and lycopodium powder which is derived from the spores of the *Lycopodium Clavatum* clubmoss [Aussillous and Quéré, 2001, Bormashenko, 2011]. Liquid marbles show promising applications in remote gas sensing and as micro bioreactors [Vadivelu et al., 2017b, Vadivelu et al., 2017a, Tian et al., 2010].

4.2 Normal Impact

Across the literature of non-wetting and partially wetting droplets, there are a number of works dedicated to the dynamic scenario of normal droplet impact. Strikingly, despite the extremely different physics of each experimental setup, the droplet impact and subsequent bounce show similar dynamics across all known scenarios. Specifically, in [Anders et al., 1993, Gilet and Bush, 2012, Richard and Quéré, 2000,

Biance et al., 2006, Planchette et al., 2012, Wang et al., 2022, de Ruiter et al., 2015a], non-monotonic trends are found in the coefficient of restitution as the impact We is increased. At very low impact We, droplets dissipate most of their initial impact energy and do not bounce. As the impact velocity in increased, there is a rapid increase in the restitution coefficient, approaching unity. Further increase in We decreases the restitution coefficient, albeit at a much slower rate. Much of the work has focused on experiments and DNS of these complex, multi-phase fluid structure interactions and there is a lack of fully predictive, first principles reduced order models that accurately describe these phenomena. Luckily, the droplet model developed in Section 3.3.2 can be utilized to study these diverse phenomena. However, as before, we will assume that the air or vapor film does not induce additional dissipation and solely acts to prevent contact.

4.2.1 Droplet Interface Model

As outlined in Section (3.3.2) , we re-use the droplet model, summarized here.

$$\xi(\theta, t) = R + \sum_{l=1}^{\infty} \beta_l(t) P_l^n(\cos\theta), \tag{4.1}$$

$$\frac{d^2\beta_l}{dt^2} + 2\alpha_l \frac{d\beta_l}{dt} + \omega_l^2 \beta_l = -\frac{(2l+1)l}{2\rho R} \int_0^{\pi} p_s(\theta) \sin\theta P_l(\cos\theta) d\theta + g\delta_{1l}, \tag{4.2}$$

with

$$\alpha_l = (2l+1)(l-1)\frac{\mu}{\rho R^2}, \tag{4.3}$$

$$\omega_l^2 = l(l-1)(l+2)\frac{\sigma}{\rho R^3}, \tag{4.4}$$

and δ_{1l} is the Kronecker delta function. In this model, we replace the bath interface model and state that the height of the rigid, non wetting substrate is zero,

$$h_d(t) = 0. \tag{4.5}$$

We utilize the "1PKM" model again and write

$$h_d(t) = z_{cm}(t) - \xi(\theta = 0, t) = z_{cm}(t) - \left(R + \sum_{l=2}^{\infty} \beta_l(t) \right), \tag{4.6}$$

closing the system and allowing us to determine the unknown contact force. Again, we assume that this unknown pressure distribution takes the form

$$p_s(r,t) = \frac{F(t)}{\pi R^2} H_r(r/r_c(t)) \tag{4.7}$$

where F is the instantaneous magnitude of the contact force, evaluated at $r = 0$ and H_r is an assumed spatial profile of the pressure in the contact region. In this section, we will use a 4^{th} order polynomial to model the impact pressure shape,

$$H_r(r/r_c(t)) = \begin{cases} C\left(1 - (\frac{r}{r_c(t)})^4\right) & r \leq r_c(t) \\ 0 & r > r_c(t). \end{cases} \tag{4.8}$$

We choose this reduced order of the polynomial compared to the previously utilized 6^{th} order polynomial due to the same 1PKM instability that occurred in section 3.4. The 4^{th} order polynomial is much more stable for this problem.

4.3 Experiments

We complete three separate experiments for each of the impact scenarios depicted in figure 4-3. We generate droplets with the same droplet generator utilized in section 3.2, taking high speed videos at 10000 fps with a Phantom Miro LC 311 camera. We set the camera with a slight angle $\sim 5°$ such that the time of initial contact is resolved. For the superhydrophobic coating case, we spray an acrylic sheet with commercially available Never-Wet Teflon-based spray, which has an equilibrium contact angle with water of 155° [Galeano-Rios et al., 2021a]. For the Leidenfrost scenario, we utilize a Thermo-Fischer hot plate, and clamp a carbon steel plate onto the heating element. The steel plate is first cleaned with soap and water to remove oil residue, then, once

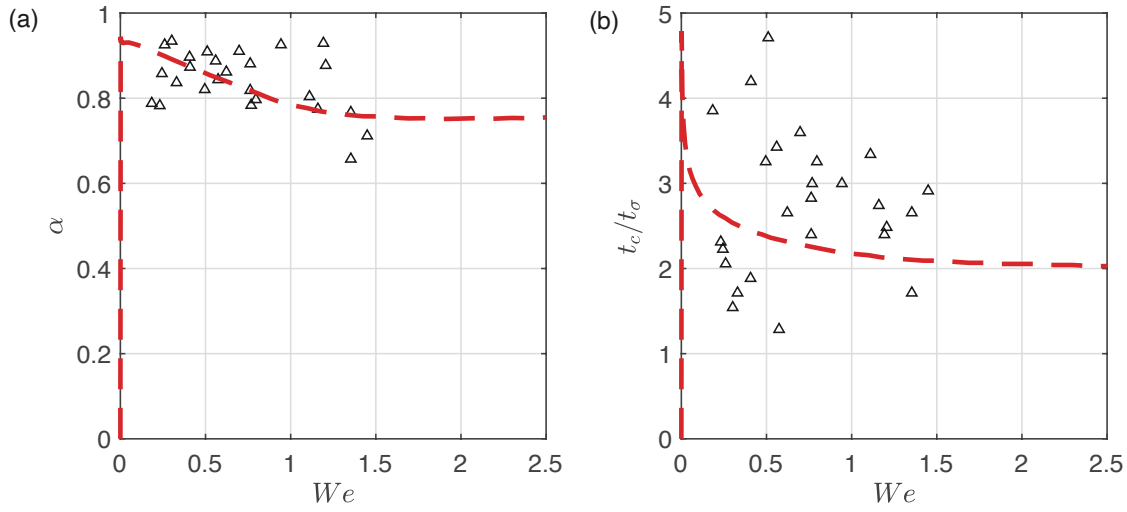

Figure 4-4: (a) Restitution coefficient as a function of We for a de-ionized water droplet $R = 0.4$ mm impacting on a superhydrophobic surface (b) Normalized contact time as a function of We

dry, it is cleaned again with isopropyl alcohol and a dust free lens cleaning paper. In order to prepare the surface for the non-wetting oil droplet impact, we 3D print a custom holding plate with a small indent in the center. The small plate is first cleaned with a solution of isopropyl alcohol, and the circular indentation in the center is filled with 0.2 mL of 10000 cSt silicone oil. The surface is then scraped with a clean razor blade to ensure that there is no local curvature on the interface. We take data and record a series of bounces. In each case, the droplet can bounce up to 10 times before coming to rest on the surface. We take each bounce and fit a parabola to the incoming and outgoing trajectories, utilizing at least 40 data points to minimize error. From the fitted parabolas, we extract the impact and exit velocities, compute the restitution coefficient and contact time.

4.4 Model and Experiment Comparison

We summarize the results of the experiments and quasi-potential model in figures 4-4, 4-5, and 4-6. In figure 4-4 the quasi-potential model accurately predicts the restitution coefficient and contact time up until $We \sim 2$. The experimental data

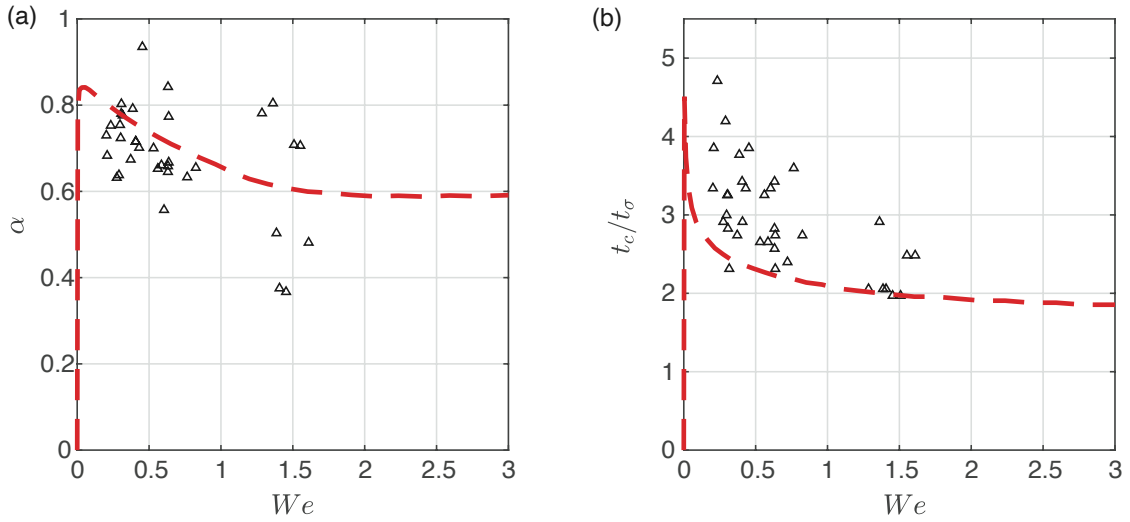

Figure 4-5: (a) Restitution coefficient as a function of We for a 2 cSt silicone oil droplet $R = 0.3$ mm impacting on a thin, 10000 cSt film. (b) Normalized contact time as a function of We

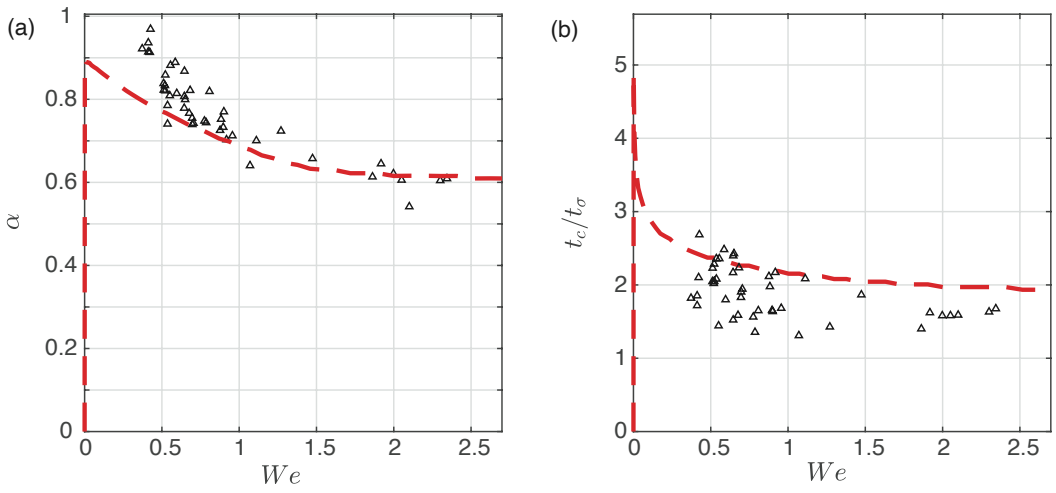

Figure 4-6: (a) Restitution coefficient as a function of We for an de-ionized water $R = 0.35$ mm droplet impacting on a superheated metal plate that maintains a constant temperature of 190°C, which is above the Leidenfrost temperature for this fluid. (b) Normalized contact time as a function of We

shows considerable scatter, which is expected due to a lack of control on droplet initial shape since the data is collected following multiple bounces. However, the data is centered enough to show the trend. As We is increased, the restitution coefficient rapidly approaches 0.95, and then decays as the impact speed is further increased. The same trends occur in figure 4-5, however the magnitude of the restitution coefficient is decreased. This is expected due to the higher kinematic viscosity of the impacting droplet. The Leidenfrost droplet impact shows similar trends in data, depicted in figure 4-6. For all impact scenarios considered in this section, we find that the quasi-potential model accurately describes the impact, suggesting the air layer or contact line motion only plays a secondary role in the liquid dynamics, as with the drop-bath impact case. Furthermore, in all experiments completed in this section, the coefficient of restitution is substantially higher than the equivalent droplet-bath impacts. When analyzing the relevant energies, the drop-bath impact problem is dominated by energy transferred to the highly deformable bath, with the droplet oscillations and dissipation playing a more minor role.

4.5 Oscillating Plate Experiment

A classical problem in dynamical systems theory is one where an elastic ball bounces on a substrate that is oscillating vertically. The non-linear coupling induces, at particular forcing frequencies and accelerations, a form of deterministic chaos. The ball's height as a function of time typically displays a period-doubling transition to chaos as the acceleration of the plate is increased [Holmes, 1982]. The elegance of this problem is evident, as such a simple experiment can be utilized to produce extreme cases of complexity. These fundamental interactions can be applied help further the understanding of granular materials [Dorbolo et al., 2005, Farkas et al., 1999, Jaeger et al., 1996] and molecular collisions [Fermi, 1949]. Granular matter deforms and flows under certain conditions, yet it is static friction that induces energy dissipation, and metastable states that depend very sensitively on initial conditions dominate the dynamical evolution of these flows. Within these flows, collisions between par-

ticles and boundaries are of paramount importance, as such, there exists a need to fully understand these seemingly simple interactions. The analysis of the bouncing ball on a plate system is very important in this regard, as typical machinery used to transport granular materials tends to rely on container vibrations to induce mass transport [Hongler and Figour, 1989]. Various experiments and mathematical models have been utilized to analyze the system for the case where the ball is perfectly elastic $\alpha = 1$, inelastic $0 < \alpha < 1$, and perfectly inelastic $\alpha = 0$, where α is the coefficient of restitution [Tufillaro et al., 1992]. Previous studies on the perfectly inelastic case have explored dynamical regimes of "transmitting" and "absorbing", where the period-doubling transition to chaos is prevented. Additionally, a numerical study on the inelastic case has provided evidence that the period doubling transition to chaos can also be prevented [Luck and Mehta, 1993], and there exists "chattering" regimes in the dynamics. Interestingly, breaking symmetries in the problem induces entirely novel dynamics as well. A bouncing inelastic ball on a slightly parabolic surface has been studied previously [McBennett and Harris, 2016], as well as on a periodic surface [Halev and Harris, 2018]. Even if the ball bounces perfectly vertically at the minimum of the surface, horizontal motion can be induced by modifying the curvature at the minimum above a critical threshold. These impacts can have a preferred direction if left-right symmetries are broken in the problem, leading to regimes of "walking".

Many models on the inelastic cases assume a constant restitution coefficient, that is $\alpha = C$ which holds for all impacts, as well as a contact time that is instantaneous [Tufillaro et al., 1992]. However, for real materials, the inelasticity of impact is a function of the impact speed and the contact time is finite. As evidenced above, the non-wetting bouncing droplets have a restitution coefficient that is a function of impact speed. We wish to analyze the system where a non-wetting droplet impacts and rebounds from an oscillating surface. The experiment that we complete is depicted in figure 4-7. It is a small bass speaker, mounted on an 80-20 aluminum frame, with Bluetooth enabled control from a Python-based application. The membrane of the speaker holds a bolt and linear shaft, and the shaft can be connected to a custom

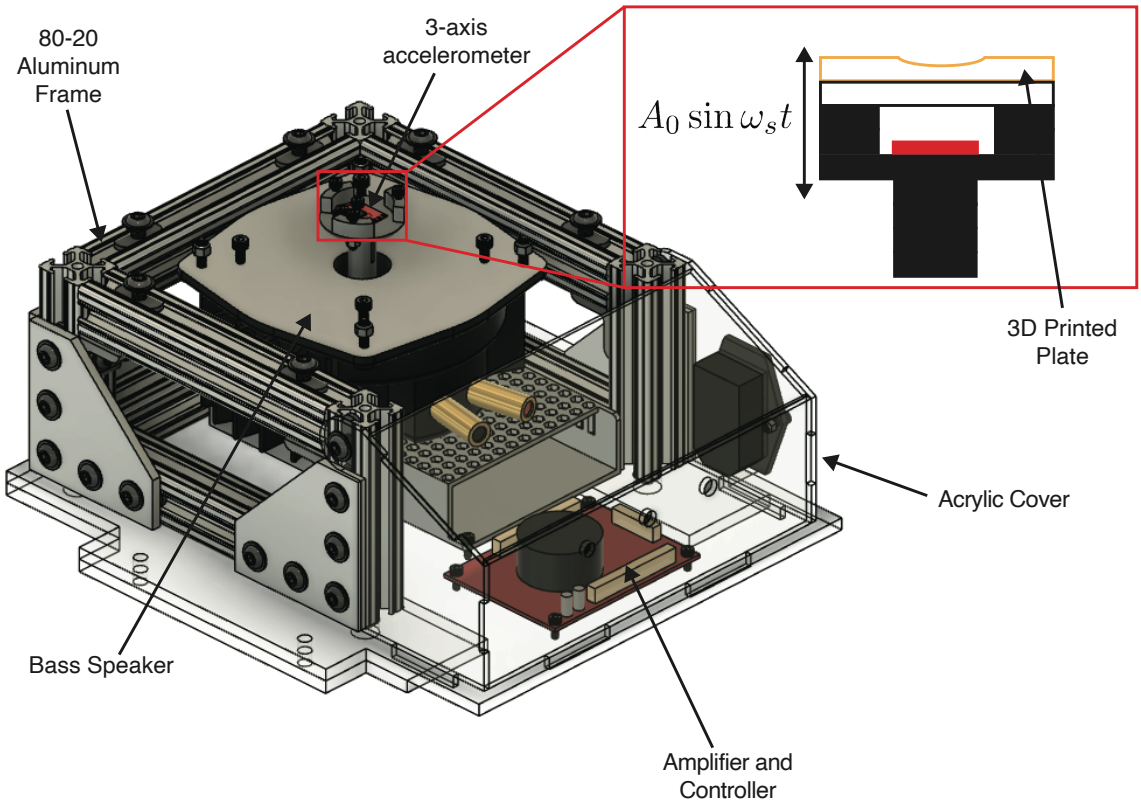

Figure 4-7: Setup for oscillating plate experiments.

3D-printed plate. The small plate is first cleaned with a solution of isopropyl alcohol, and has a circular indentation in the center, which is filled with 0.2 mL of 10000 cSt silicone oil. The high viscosity of the oil renders the substrate effectively rigid, as the short time scale of droplet impact forcing cannot substantially move the free surface during impact. The surface of the plate is then scraped with a razor blade to ensure that the oil has no indentations. The plate has a 3-axis accelerometer mounted underneath, which records acceleration data and sends it to the Python application. We set the frequency and acceleration of the plate, and deposit a single droplet of silicone fluid in the center of the dimple. The vibrating plate is enclosed by a small acrylic box to prevent air currents from disturbing the experiment.[1] In this section, we utilize droplets of 2 cSt silicone fluid. Droplets are generated with the same method utilized in all prior section, see Chapter 3.2. After the droplet bouncing settles into a stable periodic regime, we step up the acceleration of the plate in uniform steps of $0.05g$. After each increase in acceleration, we hold the forcing acceleration constant for at least 8 seconds to allow for transient behavior to disappear. The speaker application has an open-loop control that allows the user to sweep over plate accelerations. The Python application also ensures that a smooth, overdamped increase to the set point is achieved so that the droplet does not coalesce with the oil on the plate because of sudden changes in forcing amplitude during contact. An Allied Vision Mako U-130B USB camera with a Nikon 200 mm lens takes an single image every plate oscillation, producing a video file that appears to be strobed at the same frequency of oscillation as the plate. The camera is triggered with an acceleration threshold, read directly from the plate's accelerometer, triggering image capture when the acceleration crosses the $0g$ mark from below.

[1]The author would like to thank Eli Silver and Ray Gresalfi for the design and construction of the shaker setup.

4.6 Extension of Droplet Model

In this section, we account for the bottom substrate's oscillation as,

$$h_d(t) = A_0 \sin(\omega_s t). \tag{4.9}$$

No other modifications are made to the model. We also define an acceleration parameter

$$\Gamma = \frac{A_0 \omega_s^2}{g}. \tag{4.10}$$

This simulation takes substantial time, as we need to wait for unstable transient solutions to die out at each increase in acceleration. In order to simulate the same amount of time, we must speed up our code. When the droplet is in free flight, each individual mode behaves as an underdamped harmonic oscillator, and we can write down analytical solutions that hold until the next contact occurs. It is possible to have overdamped droplet modes at high values of l, but for the 2 cSt oil bifurcation run, we truncate the series before these occur as the dynamics have already converged. In order to determine the time of next contact, we reconstruct the droplet interface and measure the trajectory of the south pole of the droplet. We then search for intersections of the south pole with the oscillating plate. In the nonlinear regime, it is possible for "skipping" contacts to occur, where the droplet and oscillating plate begin contact with almost identically matched velocities. This leads to many short ($\sim \delta t$) contacts and is a numerical artifact associated with the time discretization. In the experimental system, the lubricating layer which separates the droplet and substrate provides suction forces, which would smooth out and eliminate such skipping behavior. Since we do not model these forces, we set each contact to have a minimum number of time steps, typically $3\delta t$. In free flight, each $\beta_l(t)$ can be described as

$$\beta_l(t) = Ae^{-\alpha_l(t-t_0)} \cos\left(\omega_d(t-t_0) + \gamma\right), \tag{4.11}$$

where t_0 is the last point in time where the droplet and substrate are in contact, $\omega_d = \sqrt{1-\zeta_l^2}\omega_l$, and $\zeta_l = \alpha_l/\omega_l$. We solve for the unknown constants γ and A using

the initial conditions $\beta_l|_{t_0}$ and $\frac{d\beta_l}{dt}|_{t_0}$, yielding

$$\gamma = \arctan \frac{-(\frac{d\beta_l}{dt}|_{t_0} + \beta_l|_{t_0}\alpha_l)}{\beta_l|_{t_0}\omega_d} \tag{4.12}$$

$$A = \frac{\beta_l|_{t_0}}{\cos\gamma}. \tag{4.13}$$

The height of the center of mass follows a parabolic trajectory, with

$$z_{cm}(t-t_0) = -\frac{g}{2}(t-t_0)^2 + \frac{dz_{cm}}{dt}|_{t_0}(t-t_0) + z_{cm}|_{t_0} \tag{4.14}$$

These analytical models speed up our code substantially, as the drop spends most of the time in free flight. We start the acceleration sweep at $0.5g$, and sweep in steps of $0.025g$ until we reach $2.4g$. We hold the amplitude as fixed for 5 s of simulation time and discard the first 20 bounces to eliminate transients.

4.7 Results

We drive the system at 50 Hz, and utilize an $R = 0.5$ mm droplet. The experimental results are depicted in figure 4-8. Initially, the droplet and plate system exhibit a period-1 bounce, where the drop contacts once every plate oscillation cycle at the same relative phase. As the acceleration is increased, we recover the onset of a period doubling transition to chaos, with a period-2 mode occurring at $\Gamma \sim 0.85$, lasting for a fairly large range of plate accelerations. There appears to be another period doubling event to period-4 occurring at around $\Gamma = 1.3$. Another period-4, which due to experimental noise looks similar to period-3, interrupts the chaotic regime at $\Gamma = 1.5$, beyond which the system becomes increasingly chaotic.

Now, we can utilize our code to see if the model captures this physical transition to chaos using the same physical paramters as the experiment. We run for 100 simulation seconds with a time-step of $\delta t = 30\mu s$. The results of this simulation are depicted in figure 4-10 The model captures the period-1 to period-2 transition, with the model predicting this event at approximately $\Gamma = 0.9$. This event occurs at approximately

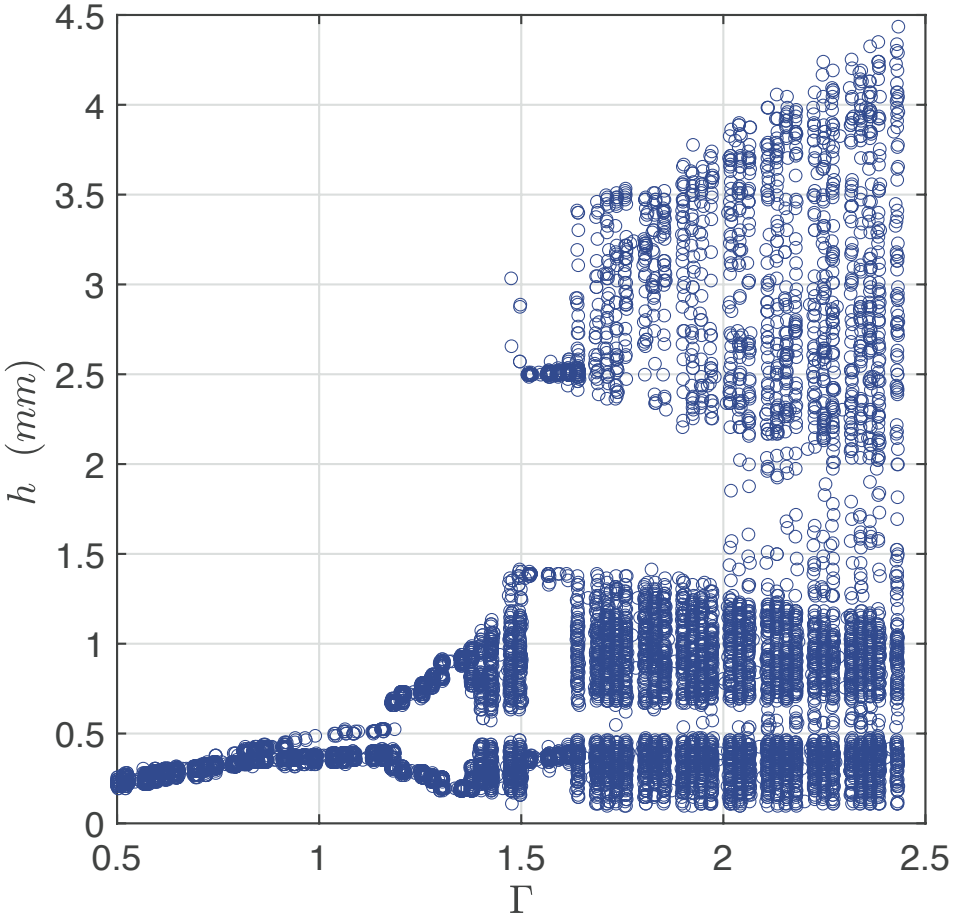

Figure 4-8: Experimental bifurcation diagram for the bouncing droplet oscillating plate system for an $R = 0.5$ mm droplet driven at 50 Hz.

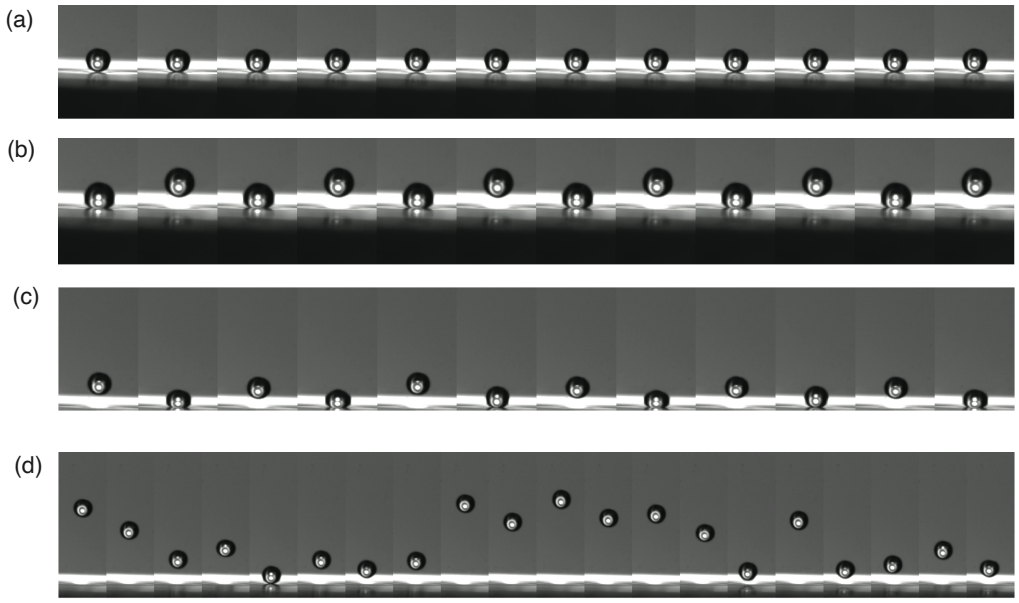

Figure 4-9: Regimes of $R = 0.5$ mm droplet driven at 50 Hz. (a) Period-1 at $\Gamma = 0.7$ (b) Period-2 at $\Gamma = 1.2$ (c) Period-4 at $\Gamma = 1.3$ (d) Chaos at $\Gamma = 2.2$.

$\Gamma = 0.9$ in the experimental system as well. The system continues on its bifurcating path, exhibiting a period-2 to period-4 bifurcation in both the model and experiment at $\Gamma = 1.4$ The system becomes increasingly chaotic as Γ is further increased for both the model and experimental system.

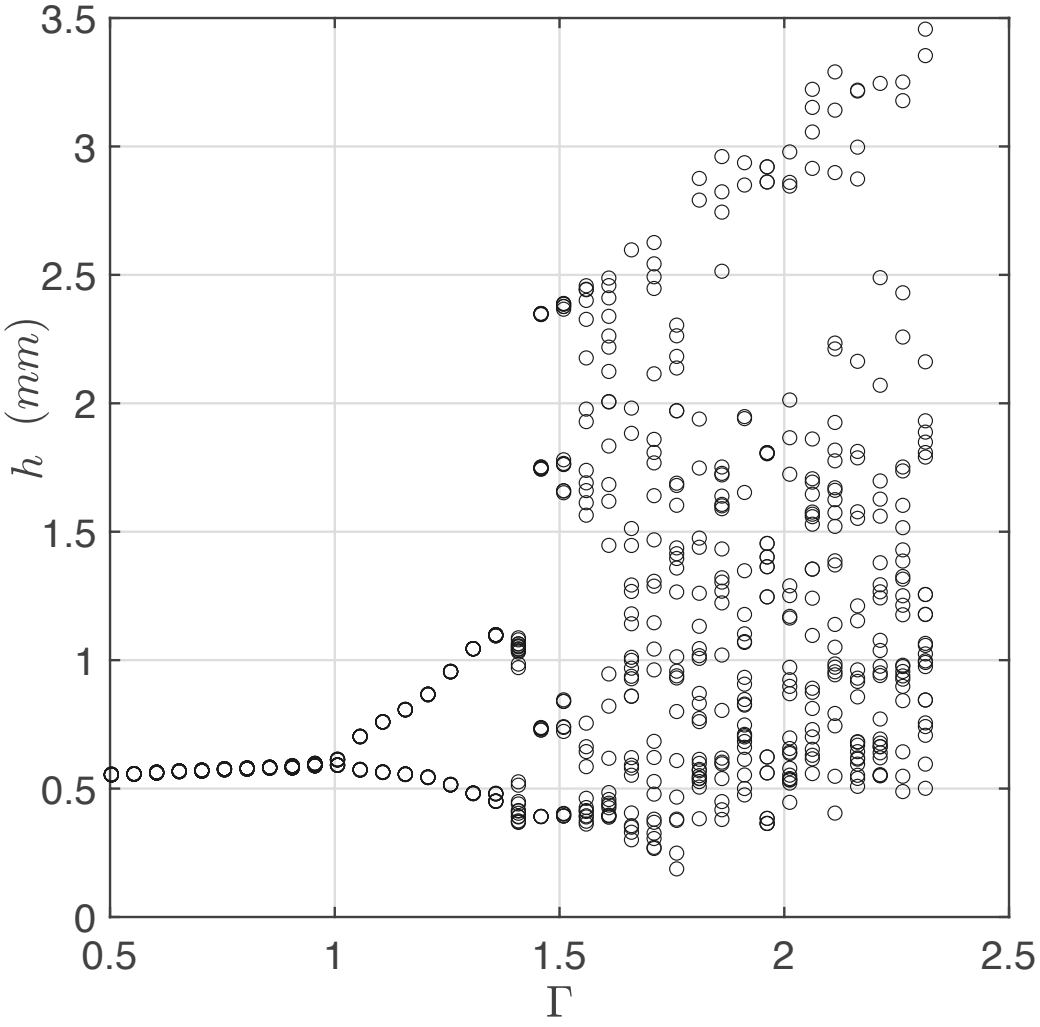

Figure 4-10: Theoretical bifurcation diagram for the bouncing droplet oscillating plate system for an $R = 0.5$ mm droplet driven at 50 Hz.

Chapter 5

Droplet Impact on Moving Liquid Layers

5.1 Introduction

Now that we have illuminated some of the finer details of the dynamics of the normal droplet impact problem, we turn to a scenario which is much more common in applications, one where the droplet and fluid bath have some relative velocity between them. In this instance, little is known about the overall dynamics, and in particular, the regimes of bouncing, coalescing, and splashing are still not well defined. Previous work has focused on streams of droplets impacting at some oblique angle to an undisturbed bath, and have found that the normal component of the velocity is sufficient to determine the transition between regimes [Schotland, 1960, Jayaratne and Mason, 1964] [Bradley and Stow, 1978, Burrill and Woods, 1969]. Additionally, the effect of droplet charge on these transitions in physical behavior has been quantified [Jayaratne and Mason, 1964]. Ultimately, these thresholds are strongly dependent on the intervening gas layer, and little is known about the lubricating flow in that layer for non-axisymmetric impacts. Prior work has focused on high energy oblique impact, and looked at the dynamics of cavity formation and the onset of splashing [Gielen et al., 2017]. The presence of shear in this lubrication flow has the potential to produce a rotating flow within the droplet, which has been shown

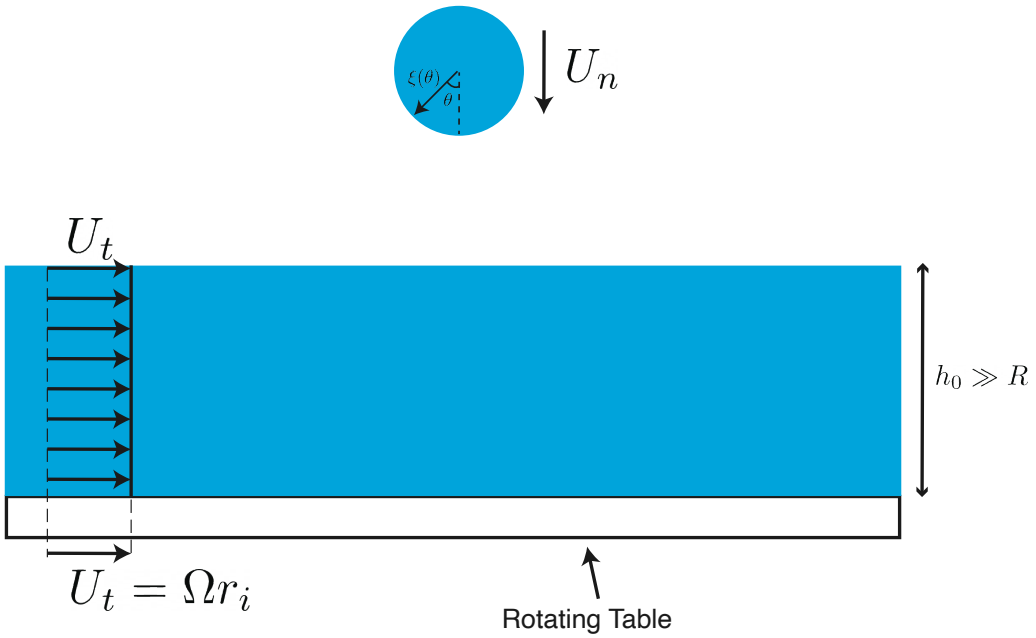

Figure 5-1: Schematic of the moving liquid layer setup. A droplet impacts normally on a deep layer of the same liquid that is moving at a uniform speed. We utilize rotation to achieve plug flow in the bath.

in prior work to induce a stable lubricating film that levitates very large droplets [Sreenivas et al., 1999, Castrejón-Pita et al., 2016, Thoroddsen and Mahadevan, 1997]. These larger droplets then enter into regimes of 'surfing'. Additionally, splashing of a droplet onto a moving layer produces striking vortices, as the shear difference between the moving layer and the droplet induces a Kelvin-Helmholtz type instability upon coalescence [Castrejón-Pita et al., 2016].

5.2 Rotating Table

In this work, we utilize a large rotating table that consists of two concentric cylinders on a flat PVC plate. The outer cylinder has a diameter of $D_o = 0.8$ m, and the inner has a diameter of $D_i = 0.7$ m. The height of the cylinders are both 10 cm. The table is filled with working fluid, and is driven by a friction wheel on

a motor.[1]The motor is directly controllable, and can continuously vary the angular rotation rates from $[0-1]$ Hz, as measured via a rotary encoder placed at the center axle. We take the centerline velocity at $r_i = 75$ cm as the droplet impact location, thus the range of table speed is from $[0-75]$ cm s^{-1}. At rotation rates above 0.8 Hz, a standing wave appear in the bath and slowly migrates around the table, so we restrict our analysis from $[0-0.66]$ Hz, or $[0-50]$ cm s^{-1} at the centerline. This wave is most likely the result of a slight warping in the bottom PVC plate. The fluid in the channel approaches a rigid-body rotation state, with a uniform plug flow. Before performing experiments, we wait a minimum of 5 min such that the fluid in the layer is at steady state. Minimal interfacial disturbances are observed for the entire range of table rotation speeds. As the table rotates, the interface develops a parabolic surface shape, which only has significant slope at rotation speeds much larger than that used in this work. In steady state, the surface shape of the fluid in the table can be written as

$$h_0(r) = \frac{\Omega^2 r^2}{2g} + C, \tag{5.1}$$

where Ω is the angular velocity of the table, r is the radial coordinate as measured from the center of rotation, and C is a volume dependent constant. The surface slope is $\frac{dh_0}{dr} = \Omega^2 \frac{r}{g}$, and thus at the maximum table speed utilized in this work, the slope at the centerline is $\frac{dh_0}{dr}|_{r=r_i} = 0.03$. The entire rotating table setup is controlled through the use of an Arduino Uno board, and is mounted on an optical table to isolate the experiment from building vibrations. In order to generate droplets, we utilize the same experimental setup as in section (3.2). The depth of the bath is approximately 3 cm, which allows for all of our experiments to be considered in the deep-pool limit. Due to the large table size and sensitivity of the problem to Marangoni effects, we decided to utilize a working fluid that was less sensitive to contamination to Marangoni flows and surfactant. In this work, we utilize 2 cSt silicone oil as the working fluid, as this fluid is significantly less sensitive to these effects.

[1]The author would like to thank Oliver Sand for the design and construction of the rotating table. His design was based on the MIT Weather-in-a-Tank apparatus [Marshall et al.,].

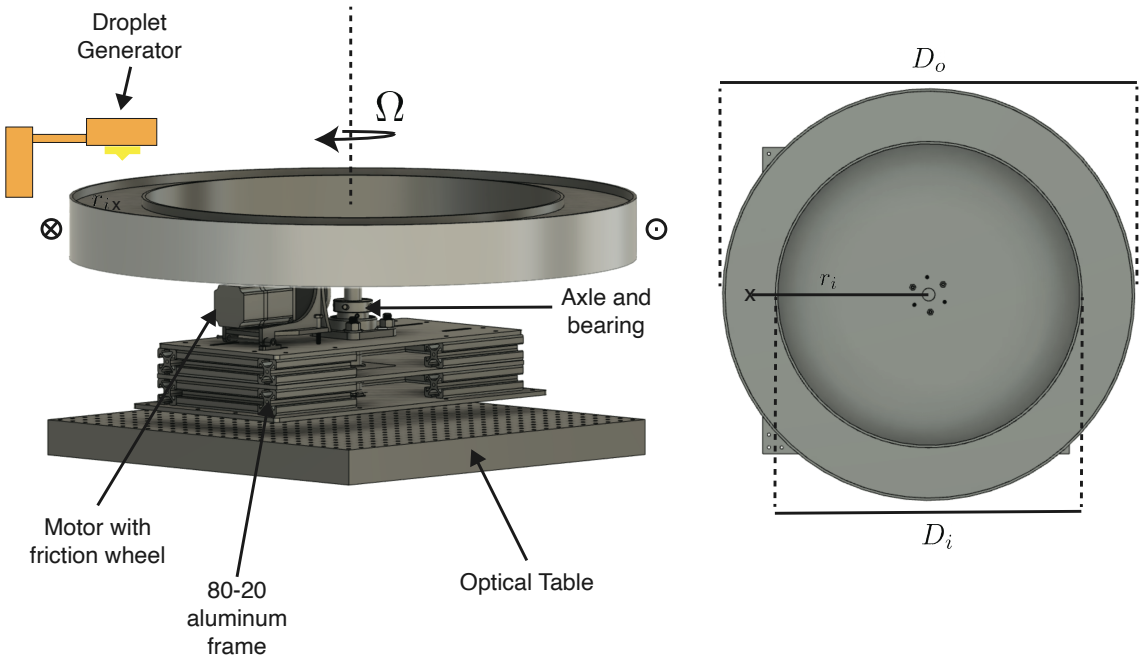

Figure 5-2: The rotating table setup.

5.3 Coalescence Thresholds

We begin the experiments by taking our reference coalescence threshold, where the surface is not moving. This threshold has been studied previously for a variety of different working fluids by [Tang et al., 2018], and found that in the deep pool limit, the threshold is characterized by the We and Oh numbers. In particular, increases in viscosity increase the critical $We_{n,cr}$ number above which coalescence occurs, and gravitational effects only weakly modify the threshold. However, as the thickness of the impacting layer varies, different regimes were identified. In these experiments, we used a slightly downward angled view of 5° such that we see over the meniscus that forms on the walls of the bath and the slight surface tilt when the table is in rotation, as previously discussed. In figure 5-3, we plot the critical normal impact velocity for coalescence for a $R = 0.24$ mm silicone oil droplet as a function of table speed. We find that there is a monotonic trend, with increases in table speed decreasing the critical normal impact velocity required to drain the interstitial air layer. In this plot, the solid line represents the normal velocity for droplets above which all coalesce, and

the dashed line represents droplets that bounce. To classify a normal velocity value as "bouncing" or "coalescing" at least 10 trials of each behavior are observed. We then take high speed video of the impacts. We fit a parabola to the incoming and outgoing trajectories to determine the impact and exit velocities. At least 40 frames are taken to minimize error. Dotted lines represent the standard error associated with each velocity measure. Each data point represents the average of at least 7 trials. The exact transition point occurs somewhere between the two curves. We plot the trend in $We_{n,cr}$ as a function of Bo in figure 5-4 where there is no rotation in the bath. There is a slight non-monotonicity in the curve, however we would need to span a larger range of Bo to determine if this effect continues. Generally, an increase in Bo increases the $We_{n,cr}$. In figure 5-5, we determine the thresholds of coalescence for 4 different droplet diameters and 5 different table rotation speeds, and summarize the results. The curves depict almost identical trends, with increases in table speed monotonically decreasing the critical $We_{n,cr}$. For the case where there is no table rotation, we determine a critical We for coalescence to be between $We = [6 - 8]$. These values are very similar to the bouncing to coalescence transition found for a variety of working fluids by [Tang et al., 2018]. For 5 cSt silicone fluid with similar density and surface tension relative to our working fluid, they found the critical We number for the transition to be ~ 8. For n-decane, which has a similar surface tension and kinematic viscosity but lower density, relative to the fluid used in these experiments, they determined the critical We number for the transition to be ~ 6.5. In all, the threshold for no rotation determined in this work is largely insensitive to the Bo, with a decrease in the Bo weakly decreasing the threshold for transition. This effect is replicated in [Tang et al., 2018], as the thresholds for n-heptadecane and 5 cSt silicone fluid only differ by $\Delta We_{n,cr} \sim 1$. These fluids have similar surface tension and viscosities but different densities, and thus, for a fixed droplet size different Bo.

In figure 5-6, we plot the critical $We_{cr,|U|}$ as defined utilizing the velocity scale of $|U| = \sqrt{U_n^2 + U_t^2}$ as a function of normalized table speed. The collapse of the data is excellent, however there seems to be an additional effect which is not perfectly captured by this scaling. It is most likely that this effect is dependent on the Bo. Now,

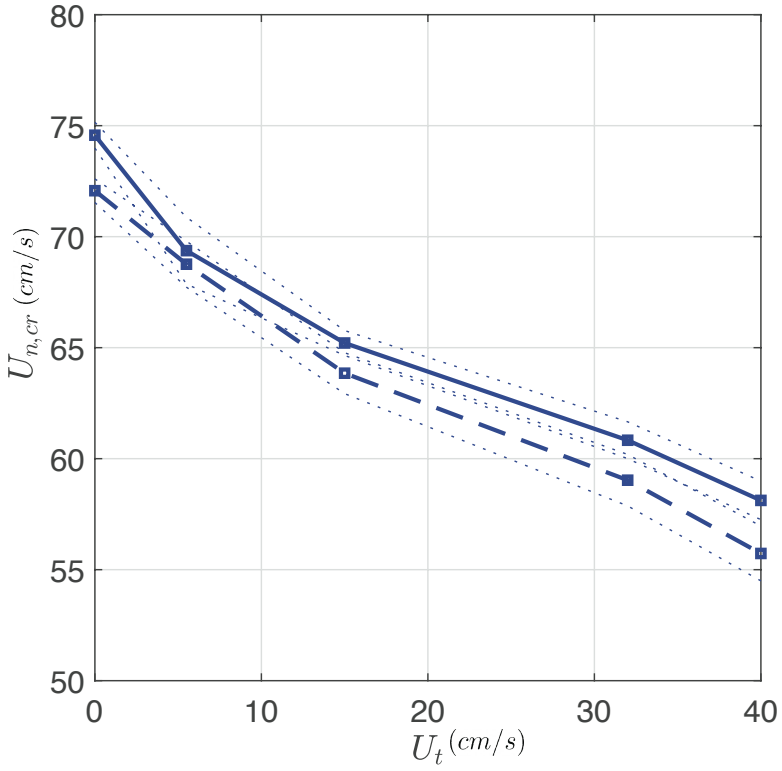

Figure 5-3: Critical normal velocity for the bouncing to coalescence transition as a function of table speed for a $Bo = 0.0265$ silicone oil droplet. The dashed line represents the normal velocity for droplets that bounce, and the solid line represents droplets that coalesce. Dotted line represent the standard error associated with each velocity measure. Each data point represents the average of at least 7 trials.

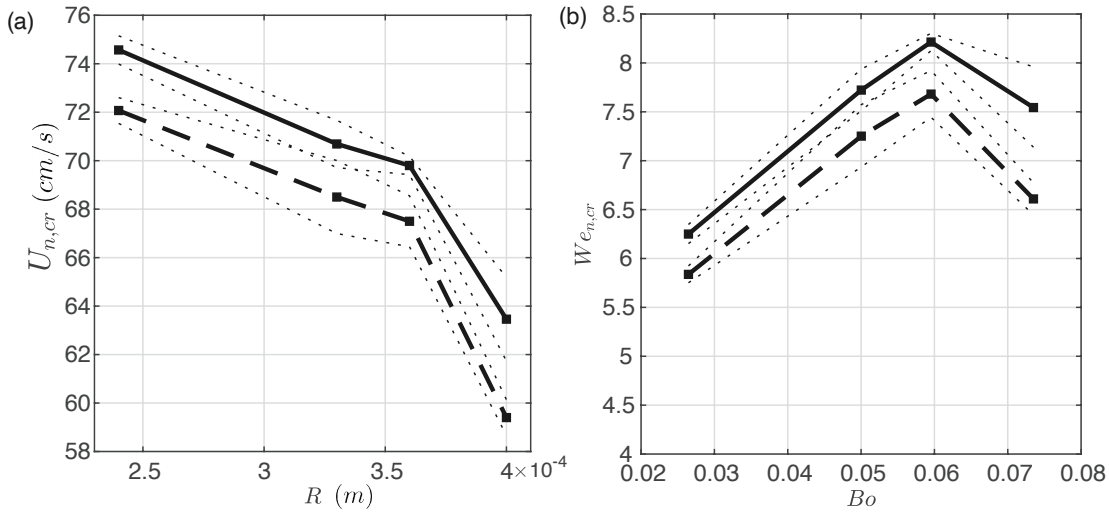

Figure 5-4: (a) Critical normal velocity for the bouncing to coalescence transition as a function of undisturbed droplet radius R for a still interface. (b) Critical normal $We_{n,cr}$ for the bouncing to coalescence transition as a function of Bo for a still interface. The dashed line represents the normal velocity for droplets that bounce, and the solid line represents droplets that coalesce. Dotted line represent the standard error associated with each velocity measure. Each data point represents the average of at least 7 trials.

we move the high speed camera to the side, such that we are viewing perpendicular to the direction of rotation. With this view the deformation of the droplet and bath are more visible. We also are able to visualize the capillary waves generated by the impact. Figures (5-7), (5-8), (5-9), (5-10), and (5-11) depict the impact of the droplet at each layer speed utilized in this work for one bouncing impact and one coalescing, just above the threshold. In these images, the layer velocity is from left-to-right and each image is separated by 10 frames, which corresponds to 2 ms. Initially, when there is no rotation in the bath, the droplet impacts and rebounds from the same point, creating an axisymmetric capillary wave. As the table speed is increased, the droplet begins to deform on the upstream side of the moving liquid layer's interface. In cases of rebound, the droplet lift-off location drifts to the left of the center point of the corresponding capillary wave as the table speed is increased. For coalescing droplets, noticeable asymmetries begin appearing in the capillary wave field for the highest two tables speeds for both bouncing and coalescing impacts. This is a mark

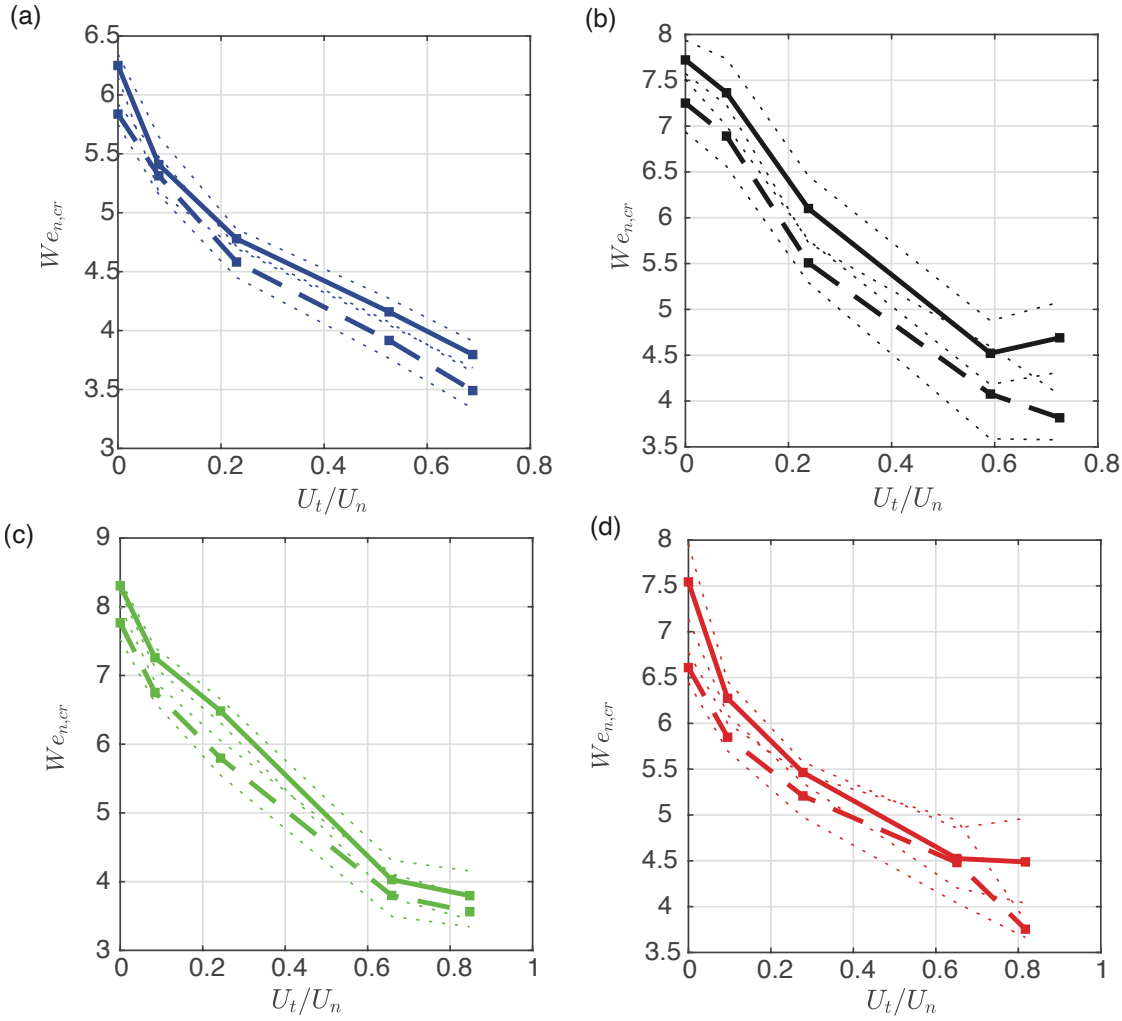

Figure 5-5: Critical $We_{n,cr}$ for the bouncing to coalescence transition as a function of normalized table speed for silicone oil droplets with *(a):* $Bo = 0.0265$, $R = 0.24$ mm , *(b):* $Bo = 0.05$, $R = 0.33$ mm,*(c):* $Bo = 0.061$, $R = 0.36$ mm,*(d):* $Bo = 0.0735$, $R = 0.4$ mm. The dashed line represents the normal velocity for droplets that bounce, and the solid line represents droplets that coalesce. Dotted line represent the standard error associated with each velocity measure. Each data point represents the average of at least 7 trials.

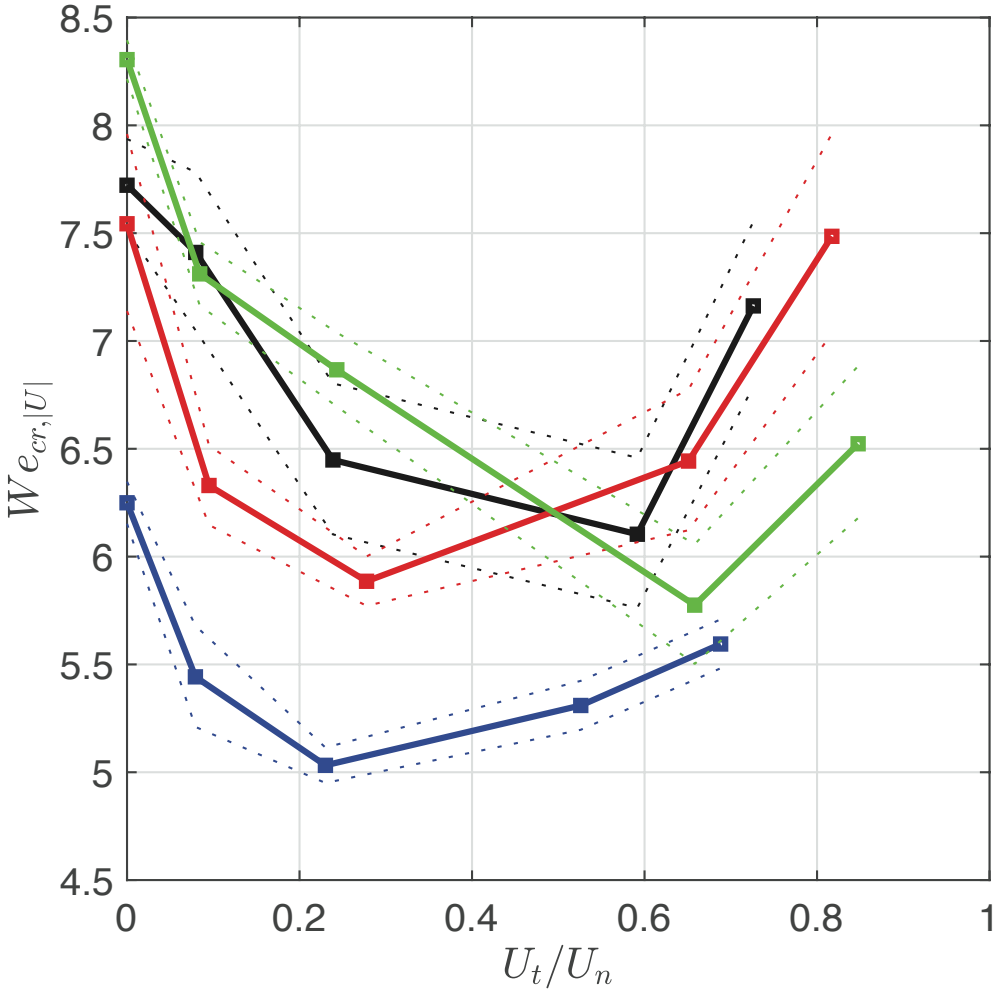

Figure 5-6: Critical $We_{cr,|U|}$ as defined utilizing the velocity scale of $|U| = \sqrt{U_n^2 + U_t^2}$, as a function of the normalized table speed for silicone oil droplets

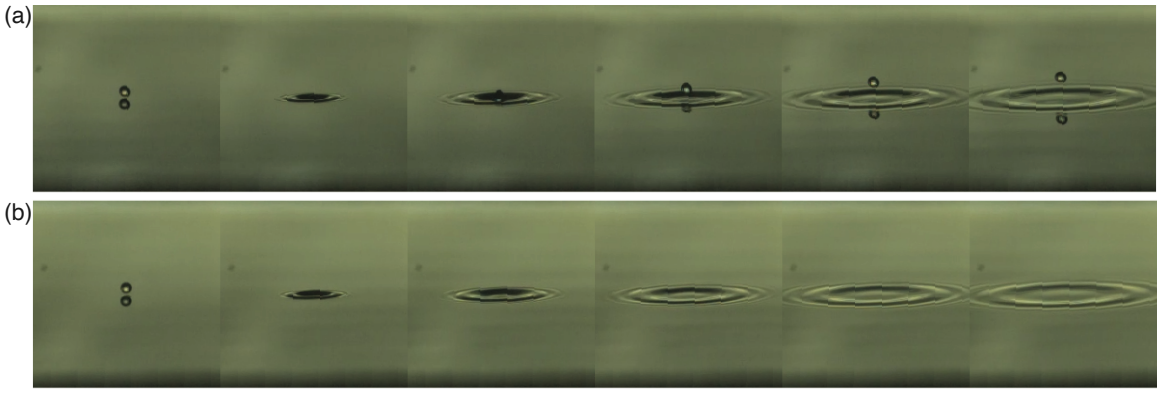

Figure 5-7: Oblique view for an (a) $R = 0.33$ mm, $U_n = 64$ cm s^{-1} and (b) $R = 0.33$ mm, $U_n = 75$ cm s^{-1} impacting droplet with no table rotation. Each image is spaced 2 ms in time from the previous image.

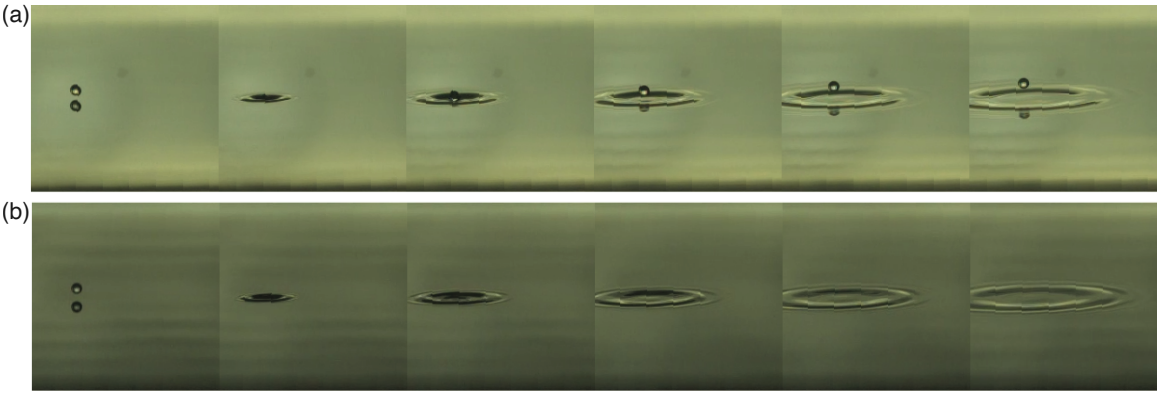

Figure 5-8: Oblique view for an (a) $R = 0.33$ mm, $U_n = 62$ cm s^{-1} and (b) $R = 0.33$ mm, $U_n = 76$ cm s^{-1} impacting droplet with $U_t = 5.5$ cm/s. Each image is spaced 2 ms in time from the previous image.

of the highly deformable substrate. As the rotation speed of the table is increased, there is a similar monotonic decrease in the We_{cr} for each Bo, depicted in figure 5-5. At the largest table speed, this critical value is almost half of the value for no rotation. We hypothesize that the lateral motion forces to droplet to press against its self generated capillary wave, which asymmetrically deforms the interstitial gas layer such that drainage is enhanced. Thus, the additional flow caused by the table rotation drains the lubricating air layer between the interfaces at a rate faster than the still layer impact. This is a somewhat counter-intuitive result, as previous results

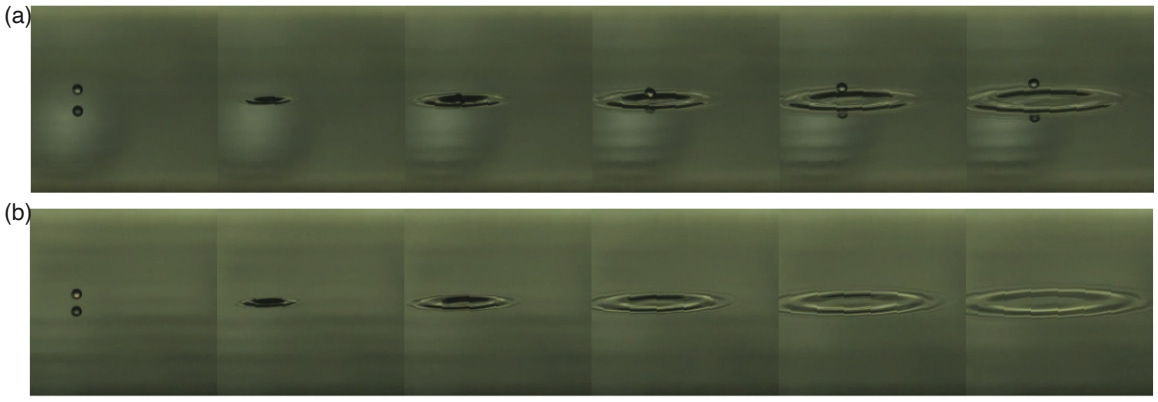

Figure 5-9: Oblique view for an (a) $R = 0.33$ mm, $U_n = 55$ cm s^{-1} and (b) $R = 0.33$ mm, $U_n = 66$ cm s^{-1} impacting droplet with $U_t = 15$ cm/s. Each image is spaced 2 ms in time from the previous image.

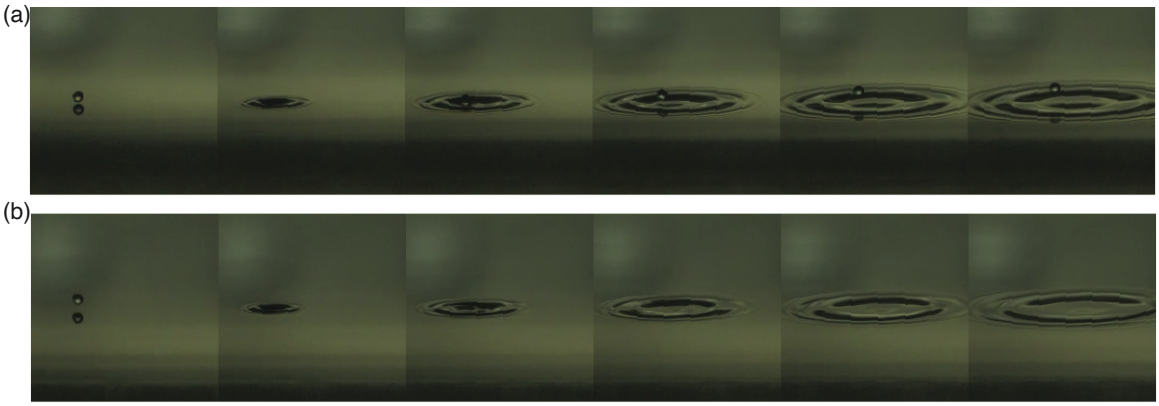

Figure 5-10: Oblique view for an (a) $R = 0.33$ mm, $U_n = 48$ cm s^{-1} and (b) $R = 0.33$ mm, $U_n = 59$ cm s^{-1} impacting droplet with $U_t = 32$ cm/s. Each image is spaced 2 ms in time from the previous image.

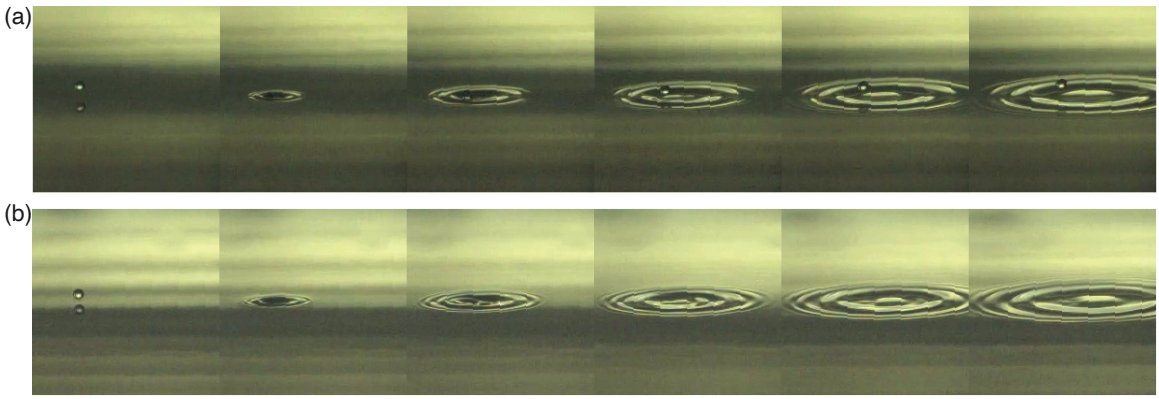

Figure 5-11: Oblique view for an (a) $R = 0.33$ mm, $U_n = 42$ cm s^{-1} and (b) $R = 0.33$ mm, $U_n = 59$ cm s^{-1} impacting droplet with $U_t = 40$ cm/s. Each image is spaced 2 ms in time from the previous image.

for droplet impact on moving layers suggest that flow in the bottom fluid layer will suppress coalescence [Dell'Aversana et al., 1996, Thoroddsen and Mahadevan, 1997, Sreenivas et al., 1999]. However, these works either utilized very large droplets, much larger than the capillary length, or used thermally induced flows to suppress coalescence. Additionally, the liquid layers in these problems were very thin, relative to the undeformed diameter of the droplet. It is most likely that substrate deformability is the key to the decrease in critical We number for coalescence in our deep pool experiments, as no significant substrate deformation is observed in thin layers. In addition, there are different physics present in the gas layer for these other scenarios could also contribute to the discrepancy. This gas layer only needs to be modified by a fraction of a micron to induce coalescence. It is also possible that the rotation of the table induces a rolling flow during impact, much like a rolling droplet on a tilted non-wetting surface [Mahadevan and Pomeau, 1999]. In this scenario, the droplet would roll like an elastic ball, possibly adding additional unresolved dynamics in the gas layer to enhance drainage. Additional experiments are ongoing to help uncover the physics of the new trend discovered in this work, as well as companion DNS simulations which resolve the gas layer dynamics.

5.4 Cleaning Methods

We originally planned on using de-ionized water as the working fluid, in order to provide an exact fluid match to collaborators studying the splashing regime with the same experimental setup. However, completing bouncing droplet experiments with water poses a unique challenge, as it is readily contaminated and can result in surface tension gradients and Marangoni flows at interfaces. Surfactants are special molecules that have a hydrophillic head and a hydrophobic tail. These molecules love to aggregate at interfaces, and can be the source of surface flows. Collectively, these molecules act to decrease the surface tension of the fluid. Locally, however, there is a distribution of molecules that potentially is non-uniform. In other words, there are local gradients in the surface tension of interfaces with surfactant, which drive additional flows, called Marangoni flows. If you look at a soap bubble in good lighting, you will be able to see the rapid flows on the surface of the bubble induced by the inhomogeneous distribution of surfactant. These flows will modify the dynamics of the droplet-bath interactions in ways which are not directly controllable. In the experience of the author, surface contamination inhibits bouncing by changing the deformability of the gas layer. Near the bouncing-to-coalescence transition, contamination creates regimes of partial coalescence, where the droplet impacts and begins to rebound from the surface, yet just as it is about to lift off, the lubrication layer drains and coalescence occurs. However, the droplet has enough inertia to stretch into a liquid ligament which is unstable due to a surface tension driven instability. This daughter droplet will then bounce, giving the illusion of a true bounce. As a result, bouncing to coalescence thresholds become more difficult to define and potentially change based on the current level of contamination. Additionally, it has been shown that Marangoni flows induced by thermal gradients can modify the dynamics of a lubricating vapor layer, potentially changing the physics entirely [van Limbeek et al., 2021]. Thus, we need a robust method for cleaning the air-fluid interface to minimize these effects. In [Kou and Saylor, 2008], a variety of cleaning methods are discussed, in particular, surfactant raking, surface vacuuming, electrostatic methods, and overflowing. We

attempted every practical cleaning method, with the exception of overflowing, and found no success in removing dust and surfactant from the interface. Surfactant rakes are small glass capillaries that are attached to a peristaltic pump. The action of the pump effectively sucks up a small volume of fluid from the interface, taking with it small particles and surfactant. Unfortunately, due to the small size of the capillaries, it was impractical for our experiment as the size of the table is very large, and thus all of the surface area cannot be covered by the capillaries. Surface vacuuming is roughly the same concept as the surfactant rake, yet removes a substantially larger volume of fluid from the bath. This method was the best performing out of those tested in eliminating surface contamination, however, removed such a large portion of the working fluid that the bath needed to be refilled after every cleaning. Once the bath is refilled, the table needs additional time to spin up into rigid body rotation. During this time, dust particles and surfactant could enter the bath, thus requiring re-cleaning, creating a seemingly never-ending cycle. This method was deemed impractical for experimentation and potentially would lead to challenges in reproduction of results. Electrostatic cleaning methods involve a glass cylinder that is swept along the surface, or in our case held in one place as the table rotates around, with the hope that the electrostatic charge on the glass rod is large enough to trap dust particles. Unfortunately, dust particles in the Harris Lab do not all have the same charge, leading to the glass rod selectively cleaning dust. Overflowing would require serious modification of our current working setup, and we chose not modify the table further. Overflowing has proven to be a successful technique in our prior experiments with water, albeit in a much smaller bath [Galeano-Rios et al., 2021a] and in section 3.2.

Chapter 6

Impact of a Rigid Sphere on an Elastic Membrane

The work presented in this chapter appears as part of a publication in the Proceedings of the Royal Society A as *Agüero, E. A., Alventosa, L., Harris, D. M., and Galeano-Rios, C. A. (2022). Impact of a rigid sphere onto an elastic membrane. Proceedings of the Royal Society A, 478(2266), 20220340.* LFA performed and analyzed the experiments and discovered the new behaviors associated with non-Hertzian effects. DMH performed the scaling analysis and wrote the quasi-static model. EAA and CGR wrote the mathematical model, created the simulation software, and utilized the software. All authors contributed to the writing of the paper.

6.1 Introduction

Mechanical contact problems arise naturally in countless industrial and scientific applications. Classical examples include the study of the deformation and stress in gear teeth [Bruzzone et al., 2021a, Bruzzone et al., 2021b, Rosso et al., 2019], ball bearings and ball joints [Askari, 2021], impact absorbers [Hundal, 1976], propagation of stress waves in colliding solids [Johnson and Johnson, 1987], and models of granular materials [Cundall and Strack, 1979]. Contact problems also frequently arise in problems relating to material characterisation, where a localized indenter is used to infer

properties of solid substrates [Herbert et al., 2001]. In particular, the mechanical response of elastic films and membranes under indentation [Begley and Mackin, 2004, Komaragiri et al., 2005, Selvadurai, 2006] has seen recent interest for applications in characterising soft polymeric and biological materials [Ahearne et al., 2005], or '2D materials' such as graphene [Gupta et al., 2015].

Several studies in contact mechanics have stemmed from the seminal works of Hertz [Hertz, 1896, Hertz, 1882]; in which, friction effects are neglected, the shape of the contact region (in the vicinity of the initial contact point) is approximated by a paraboloid, and the resulting contact surfaces are elliptical. The work of Hertz covered mainly static contacts, yielding predictions that have held remarkably well. Moreover, Hertz also considered impacts of deformable solids, working within the framework of quasi-static approximations. In particular, waves generated by the impact were ignored [Hertz, 1896, Johnson, 1982].

6.1.1 Non-Hertzian problems

Problems that do not conform to the simplifying hypotheses of Hertz are called non-Hertzian. The solution to contact problems of this kind involves a free-boundary problem on 2-dimensional (2D) surface, i.e. finding the bounding curve of the portion of the outer surface of the solids, where contact happens. Moreover, this free-boundary problem is embedded within a 3D free-boundary problem, i.e. finding where the deformed external surfaces of the contacting solids lie in the first place.

These nested free-boundary problems are also coupled; as the extent of the pressed surface influences the pressure distribution, which in turn influences the shape of the solids, on whose outer surface lies the contact surface. The coupling of these free-boundary problems brings in non-linearities of geometric origin, even when the partial differential equations that govern the deformation of the solids are linear.

Non-Hertzian contact problems represent a substantial number of cases of interest in engineering applications. Due to their complexity, analytical solutions are often unavailable and, thus, they are typically tackled using numerical methods [Karami, 1989]. The nested free-boundary problems they involve are solved using

strategies that include imposing energy minimisation principles [Kalker and Van Randen, 1972], and iterating on the extent of the pressed surface until the pressures obtained are all positive and there is no superposition of the solids outside the region where the pressure is applied [Paul and Hashemi, 1981].

6.1.2 The model problem

In the present work, we consider the problem of a rigid sphere impacting on an elastic membrane and we formulate its mathematical representation along the lines of the Kinematic Match (KM) method. Moreover, we improve the original form of the KM, expanding the compatibility conditions in the pressed area, while also reducing the size of the resulting system of equations. The resulting equations are solved numerically, yielding predictions for the contact time, trajectory of the impactor, deflection of the membrane, coefficient of restitution of the impacting sphere, and the evolution of the pressed surface as well as the pressure distribution supported on it. As the KM model was developed and implemented by collaborators, its details have not been included in this thesis but are available in the publication associated with this work [Agüero et al., 2022]. In some cases, it is possible that a decidedly simpler quasi-static model may be appropriate to model impacts on an elastic membrane. We anticipate this to occur when the kinetic energy of the membrane during the impact process is negligible as compared to its elastic energy. Such kinetic and elastic energies can be estimated to leading order by $E_k \sim \mu\Lambda^2(\delta/t_c)^2$ and $E_e \sim \tau\delta^2$ [Courbin et al., 2006], respectively, where μ is the area density of the membrane, Λ is the membrane radius, τ is the membrane tension, and δ is the maximum deflection of the membrane during an impact occuring over a time scale t_c. By requiring $E_k \ll E_e$ we find the condition

$$\frac{\tau t_c^2}{\mu\Lambda^2} \gg 1 \tag{6.1}$$

that thus corresponds to the quasi-static limit.

In a tensioned membrane the wave speed is known to be $C = \sqrt{\tau/\mu}$, and thus a timescale for wave propagation in the membrane can be defined as $t_p = \Lambda/C$. Upon

substitution, our quasi-static condition (6.1) can also be reinterpreted as a ratio of time scales:

$$\frac{t_c^2}{t_p^2} \gg 1, \tag{6.2}$$

or that the timescale of impact must be sufficiently long as compared to the time scale of wave propagation. Finally, for a freely impacting mass m, the contact time on a membrane of constant tension scales like $t_c \sim \sqrt{m/\tau}$ [Gilet and Bush, 2009], and thus our condition can also be rewritten as a mass ratio:

$$\frac{m}{\mu\Lambda^2} \gg 1, \tag{6.3}$$

or that the mass of the impactor is much greater than the total mass of the membrane. Should the our impact parameters occur outside of this limit, we expect dynamic processes to be important in determining the subsequent dynamics, requiring a non-Hertzian model.

An experimental set-up was designed to test the predictions produced by our model against controlled experiments. Our predictions for contact time and maximum surface deflection match our experimental results remarkably well, while also being in line with prior experimental results reported in [Courbin et al., 2006].

Section 6.2 presents the mathematical formulation of the impact problem. The experimental set-up and procedures are detailed in section 6.3. Comparisons to our experimental data, together with other predictions of the model are presented in section 6.4. We discuss the implications of our findings and describe ongoing directions of development in section 6.5. Julia, Python and Matlab codes, used for the computational implementations of the methods here presented are made available in a public repository, while videos of the experiments, and animations of the results are made available as supplementary material of the publication associated with this work [Agüero et al., 2022].

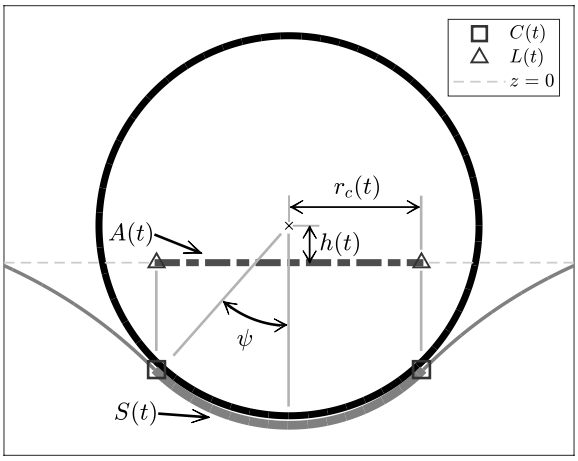

Figure 6-1: Schematic representation of the impact. The elastic membrane is shown with thin grey solid lines outside the contact surface $S(t)$, and with a thick grey solid line inside $S(t)$. It should be noted that, in this model $S(t)$ is a subset of the graph of $\eta(t)$, and that the separation shown is merely for illustrative purposes. The orthogonal projection of $S(t)$ onto the (r, θ)-plane, $A(t)$, is shown with a thick dark grey dashed line. Curves $C(t)$ and $L(t)$, which respectively bound $S(t)$ and $A(t)$, are seen as points in this cross-section. Variables $h(t)$ and $r_c(t)$ correspond to the height of the centre of mass of the sphere and the radius of $A(t)$, respectively.

6.2 Problem formulation

We consider the case of an elastic membrane of mass per unit area μ, supported by a circular rim of radius Λ, and subject to initial isotropic stress τ (see figure 6-1). We introduce cylindrical coordinates (r, θ, z) with the rim on the $z = 0$ plane, the origin at the centre of the rim, and gravity given by $\vec{g} = -g\hat{z}$.

At time $t = 0$, this elastic membrane lies in equilibrium, deformed by the action of its own weight, as the lowest point (the "south pole") of a homogeneous rigid sphere of radius R and mass m, that moves with a velocity $\vec{v}(t = 0) = -V_0\hat{z}$, is in imminent contact with the centre of the mesh (i.e. the height of the south pole coincides exactly with the height of the centre of the at-rest membrane).

We will consider only axisymmetric impacts in the present work and, therefore, we ignore all dependence on the θ variable from here on. Non-axisymmetric impacts can also be modelled by the methods here introduced; however, these will be the subject of a separate article.

6.2.1 Governing equations

We take R, $C = \sqrt{\tau/\mu}$ and $P = \tau/R$ as the characteristic length, velocity and pressure, respectively; and we define the following dimensionless numbers

$$\mathfrak{F} = \frac{g\mu R}{\tau}, \qquad \mathfrak{L} = \frac{\Lambda}{R}, \qquad \mathfrak{U} = \frac{V_0}{C}, \qquad \mathfrak{M} = \frac{\mu R^2}{m}. \tag{6.4}$$

We make the simplifying assumptions that the displacement of all points in the membrane happens exclusively along the z direction and that the tension on the membrane $\tau(r,t)$ is constant everywhere and throughout the impact.

We define $\eta(r,t) : [0,\mathfrak{L}] \times [0,+\infty) \to \mathbb{R}$ as the deflection of the membrane, and we introduce the vertical surface velocity $u(r,t) = \partial_t \eta$. Disregarding friction between the sphere and the membrane, the effect of the impact can be modelled by a pressure distribution $p = p(r,t)$ supported on $A(t)$, the orthogonal projection of the contact surface $S(t)$ onto the (r,θ)-plane (see figure 6-1).

We define $\kappa = \kappa(\eta)$ as twice the mean curvature of membrane, i.e.

$$\kappa = \frac{\partial_{rr}\eta}{\left[1 + (\partial_r \eta)^2\right]^{\frac{3}{2}}} + \frac{\partial_r \eta}{r\left[1 + (\partial_r \eta)^2\right]^{\frac{1}{2}}}; \tag{6.5}$$

and thus the elevation of the membrane is governed by

$$\partial_{tt}\eta = -\mathfrak{F} + \kappa - p, \qquad \forall\ (r,t) \in [0,\mathfrak{L}] \times (0,\infty), \tag{6.6}$$

subject to

$$p(r,t) = 0, \qquad \forall\ r,t; r \notin A(t), \tag{6.7}$$

$$p(r,t=0) = 0, \qquad \forall\ r \in [0,\mathfrak{L}], \tag{6.8}$$

$$\eta(\mathfrak{L},t) = 0, \qquad \forall\ t \geq 0, \tag{6.9}$$

with the initial conditions given by

$$\kappa(\eta(r,t=0)) = \mathfrak{F}, \qquad \forall r \in [0,\mathfrak{L}] \tag{6.10}$$

and

$$u(r, t = 0) = 0, \qquad \forall\ r \in [0, \mathfrak{L}]. \tag{6.11}$$

We note that equation (6.10) imposes that, as the membrane is about to be hit, it is found at its equilibrium shape, as dictated by its own weight distribution and initial tension.

We define $h = h(t)$ as the z coordinate of the centre of mass of the sphere and $v(t) = h'(t)$. By Newton's second law we have

$$v'(t) = -\mathfrak{F} + \mathfrak{M} \int_{A(t)} p\, dA, \qquad \forall\ t \in (0, \infty) \tag{6.12}$$

subject to

$$v(t = 0) = -\mathfrak{U} \tag{6.13}$$

and

$$h(t = 0) = 1 + \eta(r = 0, t = 0). \tag{6.14}$$

6.2.2 Kinematic Match

Four compatibility conditions are imposed. First, on the contact area $A(t)$, the two surfaces must coincide. Secondly, the velocity of the membrane u must be equivalent to the sphere's velocity within the contact region. Here, we are implicitly assuming that the deformation of the elastic membrane is such that the surface can be described at all times by a well-defined function of r. This assumption is extremely reasonable for the present case, though it is not strictly required by the KM formulation. The third condition requires that, at the boundary of the contact surface $S(t)$ (i.e. the contact curve $C(t)$), the deformable surface be differentiable. Our final compatibility condition requires that there be no superposition between the sphere and the membrane outside of the pressed surface. The mathematical formulations of these compatibility conditions can be found in [Agüero et al., 2022]. In the present

problem, we further assume that the pressed area is simply connected; which, within our axially symmetric configuration, is equivalent to $S(t)$ being a spherical cap centred at the lowest point of the sphere and, consequently, $A(t)$ being a circle of radius $r_c(t)$. Moreover, we note that, in the equations above, the only non-linear term is the one given by $\kappa = \kappa(\eta)$, in equation (6.6); however, this is by no means the only non-linearity in the problem. The other source of non-linearity is "hidden" in the problem of finding the pressed area. This full kinematic match can be considered the natural extension of the "1PKM" utilized in chapter 3, where we assume the droplet interface and bath interface contact at a single point. The full kinematic match applies this restriction over the entire contact region, simultaneously solving for the size and shape of the pressure distribution within the contact region. The "1PKM" can be considered as a further approximation of the full KM, and can potentially be applied to the current problem, but was not tested.

6.2.3 Quasi-static model

In the quasi-static limit discussed earlier, the free membrane (outside of the contact region) satisfies Laplace's equation $\nabla^2\eta = 0$ to linear order for $r_c \leq r \leq \mathfrak{L}$ (neglecting the weight of the elastic sheet). $r_c = \sin\psi$ is the radius of contact between the sphere and membrane, η is the deflection of the membrane, and all lengths non-dimensionalised by R. Under these assumptions, the deformation has a known analytical solution (with the outer boundary of the membrane fixed such that $\eta(\mathfrak{L}) = 0$),

$$\eta(r) = A_0 \ln\left(\frac{r}{\mathfrak{L}}\right). \tag{6.15}$$

To determine A_0, the tangency boundary condition at the point of contact is applied. In other words,

$$\partial_r\eta(r_c) = \tan\psi. \tag{6.16}$$

Thus the solution for the membrane shape becomes

$$\eta(r) = r_c \tan\psi \ln \frac{r}{\mathfrak{L}}. \tag{6.17}$$

Now, we need to determine the radius of contact, r_c, that occurs when a sphere is resting statically on the membrane and displaces the center of the membrane by an amount δ_s. We can thus write

$$\delta_s = -\eta(r_c) + (1 - \cos\psi) = -r_c \tan\psi \ln \frac{r_c}{\mathfrak{L}} + (1 - \cos\psi). \tag{6.18}$$

This algebraic equation can be solved numerically for r_c for each δ_s.

Furthermore, in this limit, the non-dimensional trajectory equation for the sphere (6.12) reduces to

$$v'(t) = -\mathfrak{F} + 2\mathfrak{M}A(t). \tag{6.19}$$

In the quasi-static model, $A(t)$ is fully determined by the instantaneous δ_s at time t.

6.3 Experiments

A rendering of the experimental set-up is depicted in figure 6-2. In each trial, spheres were dropped from a mechanical iris that is connected to a 2 degree-of-freedom linear stage that allows for precise and repeatable release of the spheres. The elastic membrane is clamped to a square holding plate with circular cut-out, which is then stretched over a hollow vertical cylinder of mean diameter 105 mm. The membranes used in these experiments are HYTONE LS-034 natural rubber latex sheets of thickness 0.3 mm and have a material density of 0.98 g/cm^3. The top edge of the cylinder is rounded with a 5 mm radius to ensure smooth contact with the membrane. The vertical cylinder can be precisely levelled by adjusting three levelling spring supports. The membrane holding plate is then securely fastened to an optical table. The vibration isolation provided by the optical table ensured minimal disturbances on the membrane prior to impact. A Phantom Miro LC311 camera with a Nikon Micro

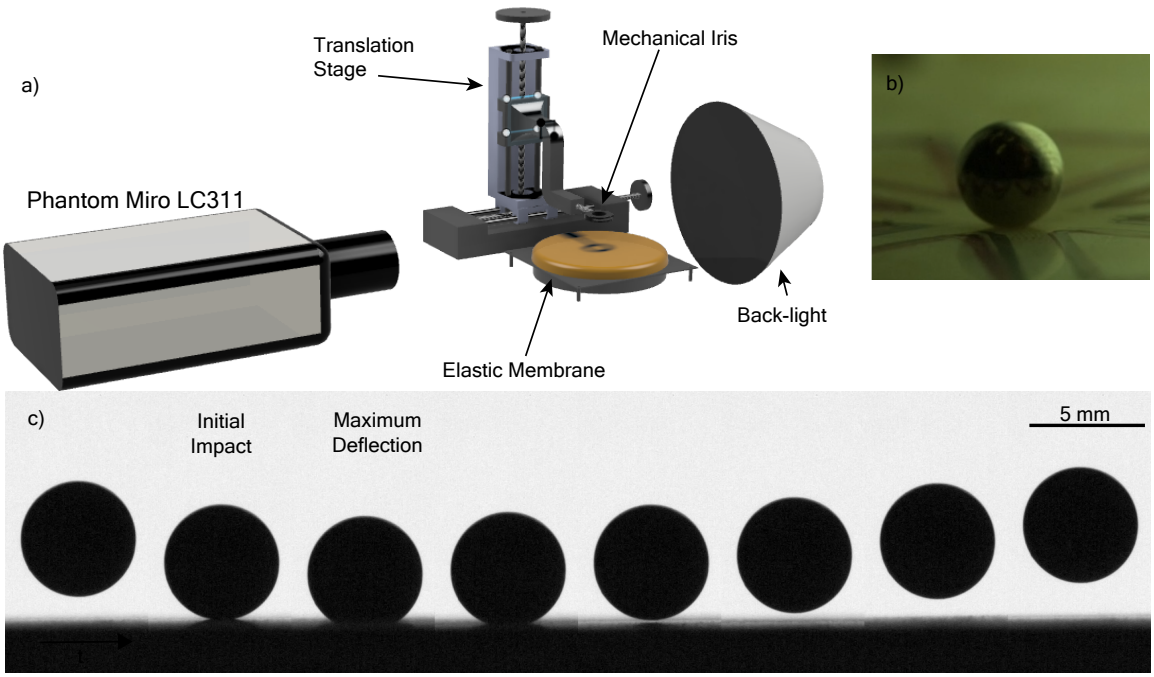

Figure 6-2: (a) A 3D rendering of the experimental setup. (b) Ceramic sphere resting on a tensioned membrane. (c) A sequence of images depicting the initial stages of impact and subsequent bounce for a ceramic sphere of diameter $D = 4.73$ mm. The time interval between images is 1 ms.

200 mm lens was used for the video capture. The camera was mounted directly on the optical table with the back edge of the camera elevated slightly for a downward viewing angle of $\sim 5°$. Images were captured at 10,000 frames per second with an exposure time of 99.6 μs. Two spheres of diameter 4.73 mm and different densities were used in this study: one of SAE 304 stainless steel $\rho_s = 7.93$ g/cm^3 and the other of Silicon Nitride ceramic $\rho_s = 3.25$ g/cm^3. Release heights were varied to achieve impact velocities from 25 to 100 cm/s .

Spheres were released from the mechanical iris at a range of heights, beginning at approximately one sphere diameter above the membrane. To characterise error, a minimum of 5 trials were completed at each height, and spheres were routinely cleaned using isopropyl alcohol and dried before being re-used in the experiments. After each increase in height, the membrane was wiped using dust-free optical lens cleaning paper. The raw video data was processed using a custom code written in MATLAB that uses a Canny edge detection. The top and bottom edges in the image corresponding to the north and south poles of the sphere, respectively, were then recorded. Initial contact ($t = 0$) was determined as the time where the actual sphere and its reflection in the membrane first met. Due to the slight downward angle of the camera toward the membrane, this instant was resolved in all trials. During contact, the south pole was obscured by the membrane edge, and the trajectory of the south pole of the sphere was determined by shifting the top trajectory down by one sphere diameter. For the range of impact speeds tested, the top point on the sphere was resolvable for all times during contact.

To determine the membrane tension, we placed a large solid stainless steel sphere of radius $R = 15.875$ mm at the centre of the membrane and measured the maximum static displacement δ_s. To relate these to the membrane tension τ, we balance the vertical forces on the sphere at equilibrium using the static membrane solution outlined in §6.2.3 and rearrange to get

$$\tau = \frac{2\rho_s R^2 g}{3r_c^2}. \tag{6.20}$$

In summary, we measured δ_s from a still camera image, then solved for r_c numerically in equation (6.18) and use equation (6.20) to determine the tension. Additionally, we compared the solution of the linearized problem above to the solution including the fully nonlinear curvature term (which yields a catenoid solution [Gilet and Bush, 2009]) and found negligible quantitative differences for our current experimental parameters.

In the present work, contact time, t_c, is defined as the time duration from when the bottom of the sphere touches the membrane to the time the bottom of the sphere returns to that height. Due to the nature of visualisation set-up, it was impossible to accurately determine when the spheres lost physical contact with the membrane. Each bounce is also characterised by its coefficient of restitution, α, which is defined here as the negative of the normal exit velocity, V_e, divided by the normal impact velocity, V_0. The exit velocity is taken to be the velocity of the top of the sphere measured exactly at the contact time, t_c. V_e and V_0 are determined by fitting a quadratic polynomial to both the incoming and outgoing trajectories in MATLAB, ensuring that at least 30 data points (frames) were used in each fit to minimise error. Additionally, we measure the maximum membrane deflection δ as the lowest point in the bottom trajectory of the sphere. Error bars are quantified as the standard deviation of the respective measurement over at least 5 experimental trials.

6.4 Results

Our simulations show the sphere landing on the membrane, deforming it as the pressed surface expands, and bouncing back as the pressed surface contracts and then vanishes. Simulations are run until the centre of the membrane starts to move downward, following lift-off. However, the method is able to capture repeated bounces, as shown in a video animation of these results, which is made available as supplementary material found in [Agüero et al., 2022]. We follow [Galeano-Rios et al., 2021b] and we check that all simulations satisfy the condition $|\nabla\eta(r,t)| < 1$, throughout the simulation, as a consistency check for our linear approximation of curvature outside the

pressed area.

To facilitate comparisons with the experimental results, we measure t_c, δ and α (as defined in the experiments). However, it should be noted that there is no difficulty in obtaining the exact time at which the sphere detaches from the membrane in our simulations, therefore it is also possible to use such instant as the basis for the definition of contact time and coefficient of restitution, if needed.

6.4.1 Comparisons to experiments

We compare our full simulation and corresponding quasi-static model predictions to our experimental results for the set-up described in section 6.3 using two different sphere densities over a range of impact velocities. In our experiments, the non-dimensional quantity $m/(\mu\Lambda^2)$ defined in equation (6.3) takes a value 0.22-0.54, signifying that we are outside of the quasi-static regime for the parameters considered here. Our predictions for contact time t_c and maximum surface deflection δ are in line with our experimental results for both sphere densities used, and our predictions for the coefficient of restitution α match the experiments for the lower sphere density case, as can be seen in figure 6-3. Agreement in the coefficient of restitution is not equally good for the larger density sphere. This error in the coefficient of restitution is, to some extent, expected in the case of heavier spheres; in which the resulting larger deformation may mean that dissipation mechanisms and material nonlinearities, not considered in the present model, are of importance to the rebound. The quasi-static model underpredicts the contact time and overpredicts the maximum surface deflection for the cases studied in figure 6-3. Furthermore, we measure $\alpha < 1$ indicative of energy transfer to the membrane during impact, an effect that is captured by the full model but not the quasi-static model. The general trends in our data and predictions, specifically the near independence of the contact time and coefficient of restitution with the impact velocity and the approximate linear relationship between the maximum deformation and impact velocity, are consistent with classical predictions of the rebound of a linear mass-spring-damper model under weak gravity [Nagurka and Huang, 2004].

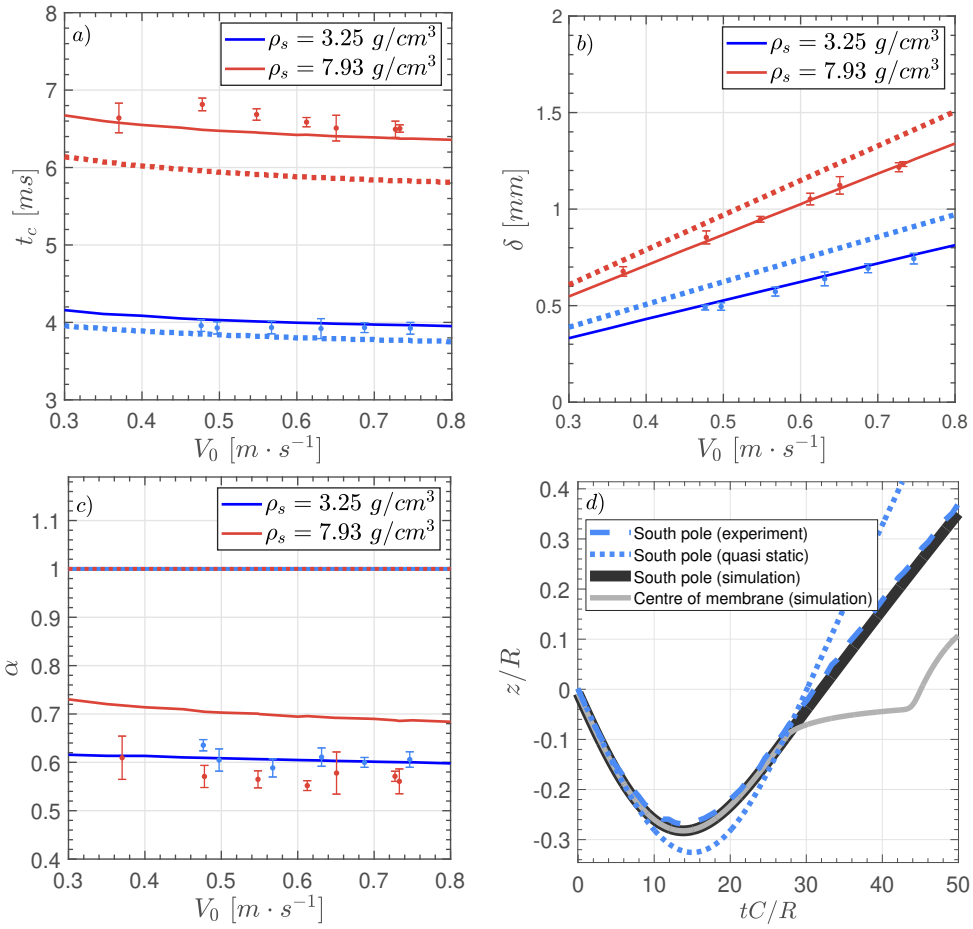

Figure 6-3: Comparison of full simulation predictions (solid lines), quasi-static model predictions (dotted lines), and experimental measurements for contact time (a), maximum surface deflection (b), coefficient of restitution (c), and south pole trajectory (d) for $\Lambda = 52.5$ mm, $R = 2.38$ mm, $\mu = 0.3$ kg/m^2 and $\tau = 107$ N/m (i.e. $\mathfrak{L} = 22.06$, $\mathfrak{F} = 6.54 \times 10^{-5}$), for both $\rho_s = 3.25$ g/cm^3 (blue lines and markers) and $\rho_s = 7.93$ g/cm^3 (red), (i.e. $\mathfrak{M} = 9.26 \times 10^{-3}$ and $\mathfrak{M} = 3.79 \times 10^{-3}$). Experimental values are shown with error bars using the same colour coding as solid lines that represent model predictions. Trajectories of the south pole are compared for $\mathfrak{L} = 22.06$, $\mathfrak{F} = 6.54 \times 10^{-5}$, $\mathfrak{M} = 9.26 \times 10^{-3}$, and $\mathfrak{U} = 3.34 \times 10^{-2}$.

The agreement of our predictions with the experiments is not limited to the metrics mentioned above, the full trajectory is also well predicted by our method. In panel *d* of figure 6-3, we compare the prediction for the trajectory of the "south pole" of the sphere with the experimental measurement of the trajectory for the same physical parameters. The corresponding prediction of the quasi-static model is also shown, with poorer agreement to the measured trajectory. In particular, the quasi-static model is unable to capture the asymmetry between the incoming and outgoing segments of the trajectory. Videos of an experiment and an animation of the simulation results for this bounce are made available as part of the supplementary material.

We also attempted a comparison of our model predictions with the results reported in [Courbin et al., 2006]. Unfortunately, a direct comparison was impossible, as the membrane tension used for each bounce was not reported. Instead, [Courbin et al., 2006] reports a range of tensions used in their experiments. Given the information provided, the best that we could do was to test whether our predictions for that range of tensions was in line with their results. Indeed, our results for the minimum and maximum tensions reported in [Courbin et al., 2006] produce an interval of possible values for the maximum deflection and the contact time that is consistent with the experimental results obtained in [Courbin et al., 2006] for the lighter spheres used in that work. Coefficients of restitution were not reported in [Courbin et al., 2006].

6.4.2 Further findings

One benefit of the present model is that it allows us to obtain detailed predictions for the evolution of variables such as the pressure distribution, which is more difficult to measure experimentally. Moreover, our model enables us to explore regimes that are challenging to experiment on, such as the low $\mathfrak{U}$ limit; in which, incidentally, our modelling assumptions are more readily satisfied.

An important quality of the method here considered lies in the fact that it captures the mechanism by which waves are generated over the contact. There are several useful implications of this virtue of the KM. In particular, we are able to estimate the

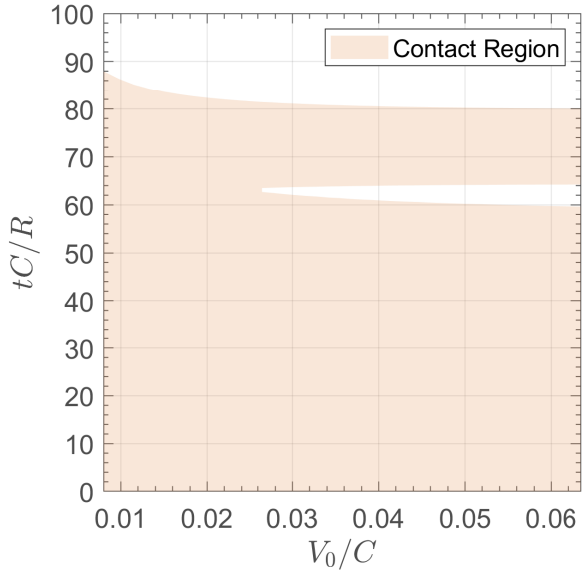

Figure 6-4: Evolution of the touch-down and take-off times as a function of initial velocity for $\mathfrak{F} = 1.81 \times 10^{-4}$, $\mathfrak{L} = 16.54$, $\mathfrak{M} = 7.11 \times 10^{-3}$.

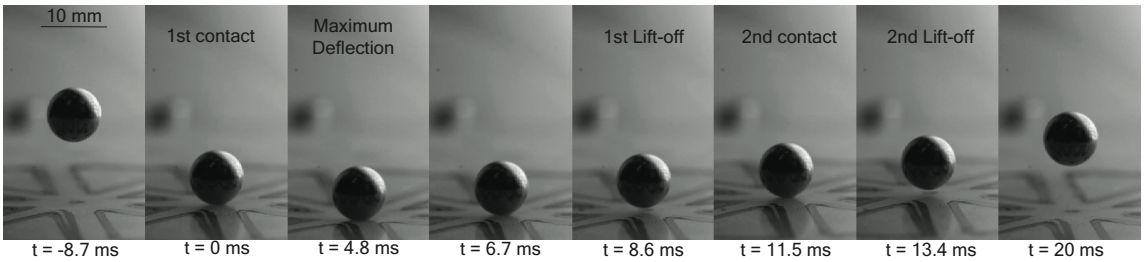

Figure 6-5: Double bounce as seen in experiments ($\mathfrak{L} = 13.08$, $\mathfrak{F} = 2.29 \times 10^{-4}$, $\mathfrak{M} = 5.62 \times 10^{-3}$ and $\mathfrak{U} = 8.23 \times 10^{-2}$).

transfer of energy to the impacted surfaces. This is reflected, for example, in the possibility to successfully predict the coefficient of restitution that results from the impact of a rigid solid onto a complex substrate, as was shown in [Galeano-Rios et al., 2021b].

Multiplicity of contacts

While carrying out the investigations described above, we were also able to identify that, for certain parameter regimes, multiple contacts occur before the centre of the membrane moves downward a second time. Such double contacts were observed in simulations as well as in experiments.

For $\mathfrak{F} = 1.81 \times 10^{-4}$, $\mathfrak{L} = 16.54$, $\mathfrak{M} = 7.11 \times 10^{-3}$, we track the contact between

the sphere and membrane in our simulations and we summarise the results in figure 6-4. The low $\mathfrak{U}$ limit does not show signs of multiple contacts. These appear at intermediate values of $\mathfrak{U} = V_0/C$, and the duration of the intermediate flight slowly increases with $\mathfrak{U}$.

We highlight that flights in between to contacts reported are extremely short periods of mid-rebound flight, which are very difficult to measure in the experiments, and consequently it was not possible to verify these experimentally. Nevertheless, double contacts can be observed in some experiments for relatively higher $\mathfrak{U}$. Figure 6-5 shows one of these double contacts, observed in the experiments. A video of this double bounce is also made available as supplementary material, for a case in which this can be clearly seen. Unfortunately, these experimental rebounds with double contacts correspond to relatively strong impacts, which somewhat escape the linearity assumptions of our model, so a direct comparison was not realistic, and indeed our model did not predict a double rebound in the case for which it is was observed in the experiments.

We note that, when the sphere lifts off for the first time, the membrane enters a free oscillation regime; in which, the configuration of the membrane is described by a (potentially infinite) sum of standing modes, each with a different oscillation frequency. At the same time, the sphere is slowing down following lift-off, as fast oscillating modes in the membrane are to catch up with the south pole of the sphere once again.

Non-monotonic decay of bouncing

Experimenting with somewhat stronger impacts, we are able to identify regimes in which a second rebound results in a coefficient of restitution that is greater than one ($\alpha > 1$). In particular, this was observed in a case when the second impact happens as the centre of the membrane is moving downward (as if in phase with the impactor). Figure 6-6, which is constructed by placing three-pixel-wide central slices of the images on the bounce, illustrates this phenomenon. The figure clearly shows that during its second impact, the sphere is able to recover some of the energy it had

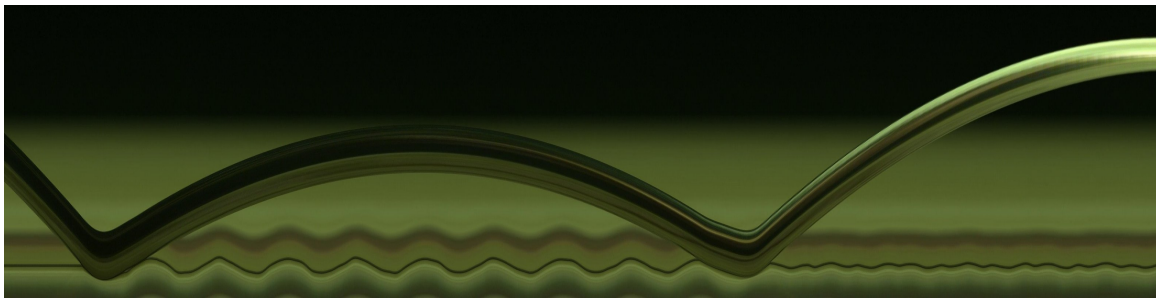

Figure 6-6: Spatiotemporal diagram composed of three-pixel-wide central slices for rebound experiment with $\mathfrak{L} = 13.08$, $\mathfrak{F} = 2.29 \times 10^{-4}$, $\mathfrak{M} = 5.62 \times 10^{-3}$ and $\mathfrak{U} = 8.39 \times 10^{-2}$. Each slice is separated by 0.19 ms. The sequence illustrates that a second impact can produce a coefficient of restitution greater than one, recovering previously transferred energy back from the vibrating membrane.

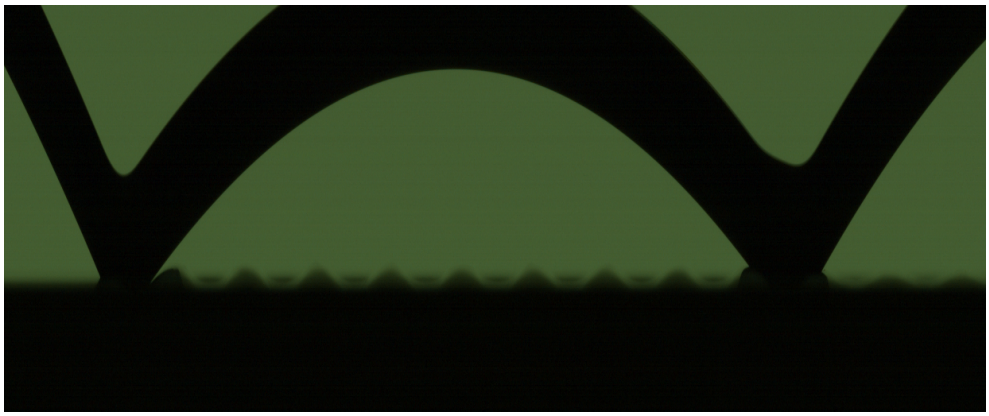

Figure 6-7: Another sample of second bounce with $\alpha > 1$ found in the experiments. The experiment corresponds to $\mathfrak{L} = 22.1987$, $\mathfrak{F} = 6.50 \times 10^{-5}$, $\mathfrak{M} = 3.82 \times 10^{-3}$ and $\mathfrak{U} = 3.62 \times 10^{-2}$.

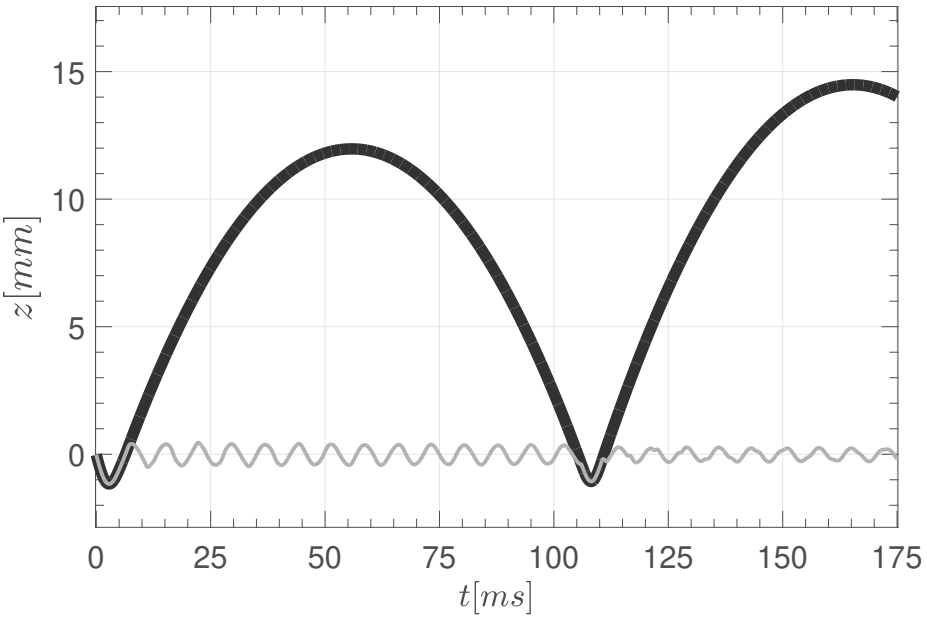

Figure 6-8: Example of second bounce with $\alpha > 1$ found in the simulations. The simulation corresponds to $\mathfrak{L} = 22.1987$, $\mathfrak{F} = 6.50 \times 10^{-5}$, $\mathfrak{M} = 3.82 \times 10^{-3}$ and $\mathfrak{U} = 3.62 \times 10^{-2}$.

bestowed to the membrane during the first bounce. A careful inspection of the first bounce in figure 6-6 reveals that the phenomenon reported in figures 6-4 and 6-5 is also present in this rebound. In figure 6-7, another case of this phenomenon occurs for a smaller sphere.

A second bounce with $\alpha > 1$ can also be seen in the simulations (see figure 6-8), proving that the model is able to capture this type of inertial effect. Moreover, we note that in all cases where we found $\alpha > 1$, whether in experiments or in simulations, the sphere impacts the membrane as the centre of the membrane is moving downward, indicating that such an impact phase contributes to this effect.

Figure 6-8 presents a sample case for which a second bounce with $\alpha > 1$ is predicted in the simulations. A larger second bounce is also found in the experiments for these parameters. However, the second bounce is particularly sensitive to the first coefficient of restitution, as a differing flight time leads to a different impact phase. In particular, a direct quantitative comparison between model predictions and experimental results for this effect is currently impractical; as even a slight mismatch in the coefficient of restitution of the first impact (compounded by experimental un-

certainty on the impact velocity) leads to different flight times (and impact phases) between consecutive bounces in the simulations. Regardless, this inertial effect is qualitatively observed in both experiment and simulation throughout wide parameter ranges. Even further experimental and modelling refinements would be necessary to achieve quantitative agreement, and will be the subject of future work.

6.5 Discussion

The application of the kinematic match method to the model problem here considered reveals the richness of what at first glance might appear as an exceedingly simple mechanical system. In particular, the possibility to model non-Hertzian effects allows us to capture behaviour that results from the wave-mediated exchanges of energy between the colliding solids.

The exploration of a parameter regime that lies away from the quasi-static limit (characterised by equations 6.1 and 6.2) reveals new phenomena in both experiments and simulations. In particular, we have shown that the energy exchange with wave field in the membrane can lead to complex behaviour that includes multiple contacts over a single rebound, and non-monotonic decay of the rebound amplitude. These effects attest to the need for models of the present kind to have reasonable predictions for the coefficient of restitution, such as the ones given here.

For the range of impacts most readily accessible in experiment, the coefficient of restitution depends only weakly on impact velocity, it increases with the radius of the sphere, and it also increases for increased sphere density, when all other parameters are kept constant.

Chapter 7

Conclusion

In all of the related impact scenarios, we see that inertia and capillarity act to dominate the dynamics of the deformations of both impactor and substrate, leading to the diverse range of phenomena described throughout this work. Impact inherently generates surface waves, transferring initial kinetic energy into surface energy. Additionally, the experimental methods utilized in this work are highly accessible, allowing for the generation of large data sets that drive the verification and validation of many different types of numerical models of impact. Ultimately, the particular combination of reduced-order modeling, experiments, and DNS utilized in this work sets a high standard for studying the diverse range of inertio-capillary impacts. The modeling methods presented here are highly versatile, with only a single embodiment thereof considered here in terms of target canonical physical scenario. There are a number of possible additions to the existing model used in chapter 3 that could expand its reach to other related problems. For instance, the model for the droplet deformation can be extended into a regime where the dynamics of the gas layer does matter, and the gas layer dynamics coupled to the droplet deformation through the use of lubrication equations. Moreover, numerous authors have studied the variety of phenomena that occur when a droplet impacts another droplet [Qian and Law, 1997, Tang et al., 2012]. Droplet-droplet collisions are of extreme importance in combustion science [Jiang et al., 1992] and cloud formation [Grabowski and Wang, 2013]. Future work will consider the effect of relative

surface tension and viscosity, where the droplets are composed of a different fluid than the bath. Furthermore, the effects of incident droplet or bath deformations could be readily studied, and has been shown to influence bouncing behavior in similar systems [Biance et al., 2006, Yun, 2018]. These effects can be included in our existing model with the application of the appropriate initial conditions on the droplet. Furthermore, the simplified version of the kinematic match introduced in this work requires further study from a numerical perspective. The time-step threshold below which unstable oscillations in the impact force needs further attention, in particular. It is possible that it is the result of the weakly damped assumption utilized throughout the work. As we saw at the end of chapter 4, the solutions for the decay of each mode in free flight include an $e^{-\alpha_l t}$, which when discretized would read $e^{-\alpha_l \delta t}$. If δt and α_l are small enough, it is possible that limits on numerical precision could lead to the code interpreting this as an undamped problem, potentially causing these oscillations. It is important to note that the oscillations are not a true instability, as each mode amplitude and velocity remains bounded and well-behaved. The forcing term simply oscillates until the minimum force threshold is crossed, after which the simulation is terminated. We attempted to utilize various other pressure distribution shape functions, including a bell function [Boyd, 2006], and found almost identical behaviour to that of the polynomials utilized in this work.

The model can also be adapted to non-axisymmetric domains, or to droplet impacts at varying angles of incidence. It is also possible to model the experiments completed in chapter 5 utilizing a more general form of the weakly damped free surface models. However, in these cases the full kinematic match should be utilized, as the shape of the pressure distribution would likely change at each time step. Currently, the only modeling work done on these moving liquid layer problems are DNS, and the application of a reduced order model would elucidate the dynamics of impact in those scenarios. Further experiments can be completed with the rotating table to better understand the role of substrate deformability. An updated experiment utilizing a method to measure surface deformation, like a synthetic Schlieren method [Moisy et al., 2009], would shed additional light on the dynamics of the impact and

transition in behavior. If possible, the completion of an experiment with interferometric measurements on the gas layer in this impact scenario would be of fundamental importance.

Additionally, it is possible as well to re-create the study in chapter 6 utilizing the "1PKM" formulation to provide a direct comparison to the full kinematic match. The decomposition methods utilized in chapter 3 can be re-used, as a similar orthogonal function decomposition can be completed for a cylindrical elastic membrane. We can additionally study the impact of droplets on these membranes, possibly extending the membrane model to study the impact of droplets on flexible cantilevers, which have been demonstrated in prior literature to mimic droplet impact on leaves. The simplified matching condition can be used as well in studying impacts of two rigid spheres, providing a very simple framework for modeling contacts between elastic objects.

Appendix A

A.1 Quasi-Static Methods for Determining Radius of Contact $r_c(t)$ During Drop Bath Rebound

In this Appendix, we will detail a few other models for the instantaneous contact area between a droplet and a non-deformable substrate. These models are more computationally efficient than the intersections based model utilized throughout the work, yet are too restrictive in that they require either low We and low Bo or low We and intermediate Bo to be valid. This creates additional restrictions on the model, but due to their efficiency and simplicity, these models may be useful in other related work.

A.1.1 Linearized Young-Laplace Equation

If we revisit our dynamic boundary condition (A.1), we can see that if the impact velocity is reduced, the first and third terms on the right hand side become dominant. Assuming the droplet remains spherical during contact, we can choose a length scale as R, a time scale as $\sqrt{\frac{\rho R^3}{\sigma}}$, and scaling for the potential as $V_0 R$.

$$\partial_t \phi = -g\eta - 2\nu\partial_z^2\phi + \frac{\sigma}{\rho}H - \frac{P_s}{\rho} \tag{A.1}$$

We can non-dimensionalize the above equation as $\widetilde{\eta} = \frac{\eta}{R}$, $\widetilde{r} = \frac{r}{R}$, $\widetilde{\phi} = \frac{\phi}{V_0 R}$, and $\widetilde{t} = \sqrt{\frac{\sigma}{\rho R^3}}t$. We restrict our analysis to be outside of the region of contact, such that

$P_s = 0$. Substituting these into the equation, and re-arranging gives us

$$\sqrt{We}\ \partial_{\widetilde{t}}\widetilde{\phi} = -Bo\ \widetilde{\eta} - 2Oh\ \partial_{\widetilde{z}}^2\widetilde{\phi} + \widetilde{H}, \tag{A.2}$$

where Bo and Oh are the Bond and Ohnersorge numbers, respectively. In the limit that $We \ll 1$, $Oh \ll 1$, $Bo \sim \mathrm{O}(1)$ this boundary condition will reduce to the Young-Laplace equation, which balances surface tension and gravity in a static equilibrium. Consistent with our previous linear assumption, we can linearize the equation, and write it as

$$\mathrm{Bo}\ \widetilde{\eta} = \frac{1}{\widetilde{r}}\partial_{\widetilde{r}}(\widetilde{r}\partial_{\widetilde{r}}\widetilde{\eta}). \tag{A.3}$$

Rearranging this expression and dropping the tildes gives us

$$\partial_r^2\eta + \frac{1}{r}\partial_r\eta - \mathrm{Bo}\ \eta = 0 \tag{A.4}$$

This is a modified Bessel equation of order zero, which has a known solution

$$\eta(r) = EI_0(\sqrt{\mathrm{Bo}}\ r) + DK_0(\sqrt{\mathrm{Bo}}\ r) \tag{A.5}$$

where I_0 , K_0 are the modified Bessel functions of the first and second kind, respectively. The boundary conditions are given as

$$r \to \infty\ ,\ \eta \to 0 \tag{A.6}$$

$$\partial_r\left(\eta|_{R\sin\psi}\right) = -\tan\phi \tag{A.7}$$

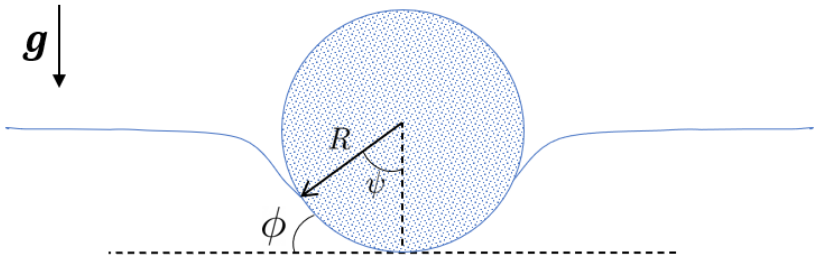

Figure A-1: Schematic of Variables for the Young-Laplace equation

These conditions give the value of the two unknown constants,

$$D = \frac{-\tan\phi}{\sqrt{\text{Bo}}\, K_1\left(\sqrt{\text{Bo}}\, R\sin\psi\right)} \tag{A.8}$$

$$E = 0 \tag{A.9}$$

Now, we can relate the growth of the radius of contact to the center of mass height of the object as

$$z_{cm} = \eta|_{R\sin\psi} + R\cos\psi \tag{A.10}$$

$$r_c = R\sin\psi \tag{A.11}$$

Thus, $r_c = r_c(t) = r_c(z_{cm}(t))$. Typical profiles for $r_c(z_{cm}(t))$ are shown in Figure A-2.

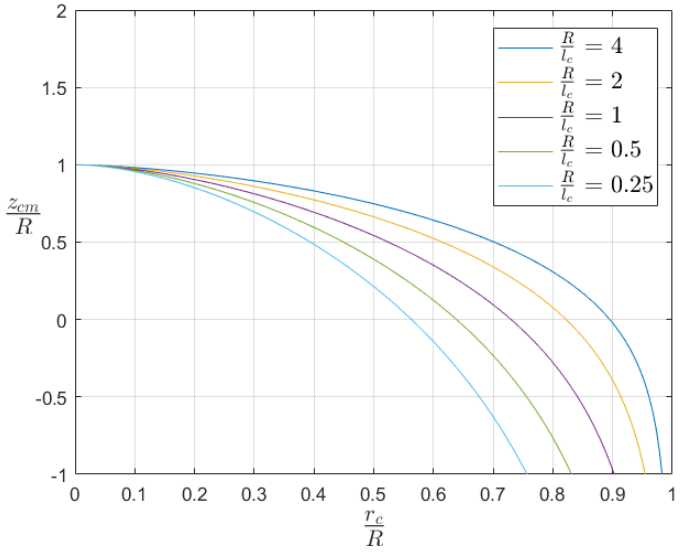

Figure A-2: The center of mass height, z_{cm} as a function of the radius of contact, r_c, non-dimensionalized by R, for different values of $\frac{R}{l_c} = \sqrt{\text{Bo}}$.

A.1.2 Including Ellipsoidal Solutions

In our original quasi-static approximation for the radius of contact, we always assumed the droplet to be spherical. However, since we have modeled the droplet as

deformable, we can approximate it to take on an ellipsoidal shape during and after contact with the free interface. The droplet takes on the shape of an oblate spheroid rapidly after contact is first initiated, and then the eccentricity decays as the droplet oscillates in free flight. This may lead to an increased radius of contact at early times relative to the spherical case, which would improve our prediction for the bouncing droplet contact area.

To extend this model to include ellipsoids, there is really only one geometric quantity that changes. In Figure A-4, we have a rigid sphere resting on an interface. From inspection, we have

$$K = \theta - \phi. \tag{A.12}$$

Additionally,

$$L + \phi + K = \pi \tag{A.13}$$

$$\frac{\pi}{2} - \psi + L + \phi = \frac{\pi}{2}. \tag{A.14}$$

Thus,

$$\phi = \theta + \psi - \pi. \tag{A.15}$$

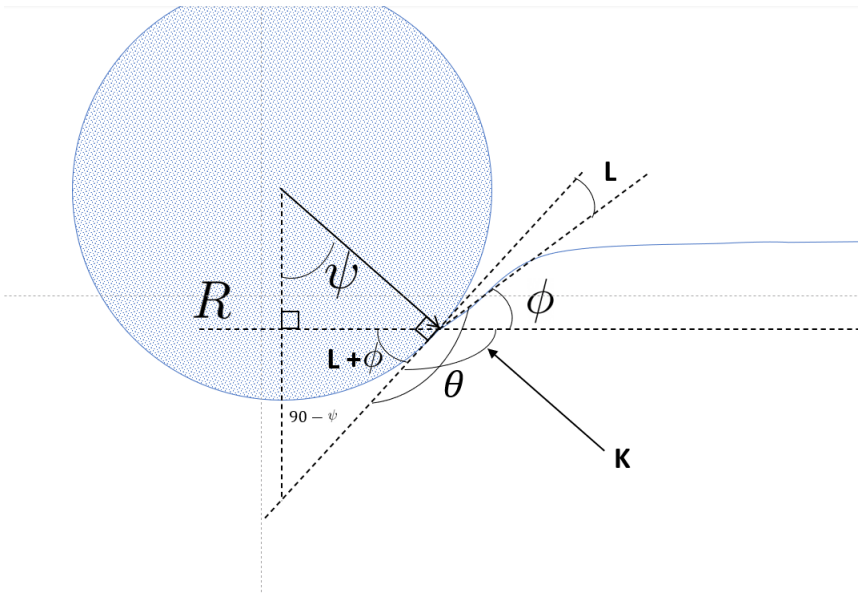

Figure A-3: Geometric Schematic of Angles for the Young-Laplace equation for a sphere resting on an interface.

This has been utilized in numerous papers, most notably by [Vella et al., 2006, Galeano-Rios et al., 2021 Lee and Kim, 2008].

For an ellipse, the only geometric quantity that changes is now, $R = R(\psi)$. Thus, the angle that the radial vector R makes with the tangent can no longer be assumed to be $\pi/2$. This value, depicted as α, can be computed through the use of a dot product. If we take the radial vector,

$$\overrightarrow{R} = \overrightarrow{R}(\psi) = [a\cos\psi, b\sin\psi]^T, \tag{A.16}$$

and take a derivative, we will have the tangent vector, $\overrightarrow{T}$. Dotting $\overrightarrow{T} \cdot \overrightarrow{R}$ gives us

$$\alpha = \cos^{-1}\left(\frac{\overrightarrow{T}\cdot\overrightarrow{R}}{||\overrightarrow{T}||||\overrightarrow{R}||}\right) \tag{A.17}$$

Then, we can perform the same calculation as before from inspection, we have

$$K = \theta - \phi. \tag{A.18}$$

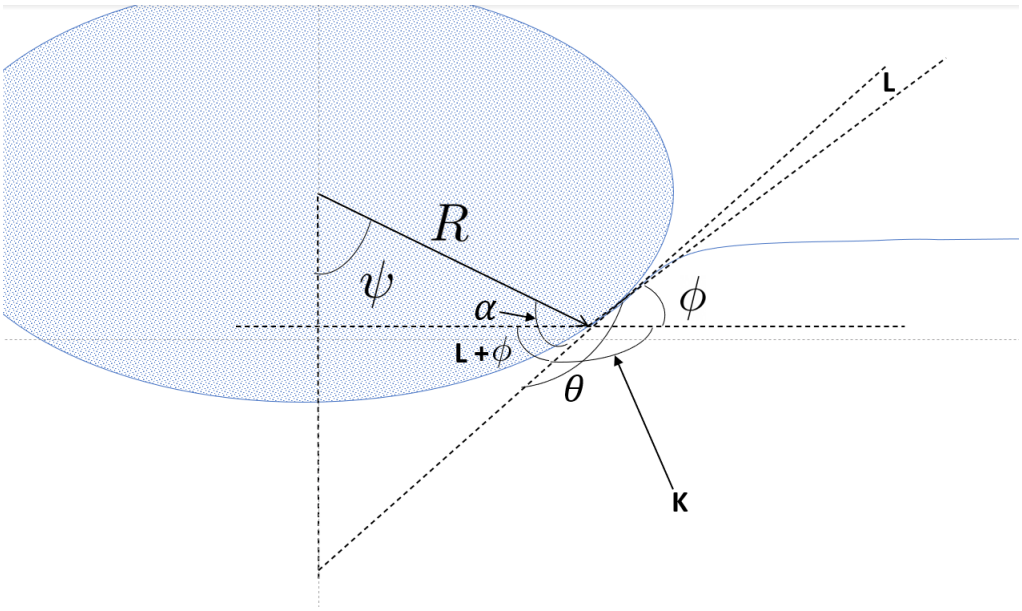

Figure A-4: Geometric Schematic of Angles for the Linearized Young-Laplace equation for an oblate spheroid resting on an interface.

Additionally,

$$L + \phi + K = \pi \tag{A.19}$$

$$\frac{\pi}{2} - \psi + L + \phi = \alpha. \tag{A.20}$$

Thus,

$$\phi = \theta + \psi + \alpha - \frac{3\pi}{2}. \tag{A.21}$$

This expression for the interface angle ϕ can be used to solve for the interface shape as

$$\eta(r) = DK_0(\sqrt{\text{Bo}}\, r) \tag{A.22}$$

with

$$D = \frac{-\tan\phi}{\sqrt{\text{Bo}}\, K_1\left(\sqrt{\text{Bo}}\, R\sin\psi\right)} \tag{A.23}$$

$$\tag{A.24}$$

and finally solving for the contact radius as a function of the height as

$$z_{cm} = \eta|_{R\sin\psi} + R\cos\psi \tag{A.25}$$

$$r_c = R\sin\psi \tag{A.26}$$

A.1.3 The Quasi-static Approximation for a Droplet Resting on a Rigid Surface

In the work of [Mahadevan and Pomeau, 1999], the rolling of a sessile droplet was studied theoretically. In particular, they write a scaling law that relates the size of the contact area of the non-wetting droplet to the deformation, as measured by the lowering of the center of mass due to the droplets weight. This law is

$$A_c^2 \sim R\delta, \tag{A.27}$$

where A_c is the contact area, R is the undeformed radius, and δ is the "sag" of the droplet. Typically, this measure is used at the top of the droplet, where $\delta = D - D_d$ where D is the undeformed droplet diameter and D_d is the deformed droplet diameter, as measured vertically from the substrate to the top of the droplet. This sag measure can also be defined using the center of mass heights with $\delta_{cm} = R - z_{cm}$. They then utilize energy scaling analysis to determine that

$$\delta \sim Bo\, R, \tag{A.28}$$

and,

$$\frac{A_c}{R^2} \sim Bo\,. \tag{A.29}$$

Then, equating the two yields

$$\frac{A_c}{R} \sim \delta. \tag{A.30}$$

Measurements taken in [Aussillous and Quéré, 2001] confirm these scalings. In [Chevy et al., 2012], they extend this analysis by considering the shape of the sessile drop, and utilized the Young-Laplace equation to write an analytical solution for the shape of a non-wetting droplet. Then, they computed the sag of both the center of mass and top of the droplet, finding a weakly-logarithmic expression for the sag

$$\frac{\delta}{R} = \frac{Bo}{3}\left|\ln\frac{Bo}{6}\right|, \tag{A.31}$$

$$\frac{\delta_{cm}}{R} = \frac{Bo}{3}\left|\ln\frac{e^{5/6}Bo}{6}\right|. \tag{A.32}$$

This analysis holds for sessile droplets or droplets that are weakly oscillating on a non-deformable surface.

We performed experiments using sessile liquid marbles and water droplets on a superhydrophobic plate, measured the sag of the top and center of mass of the droplets, and confirmed the results of [Chevy et al., 2012]. Then, we can check the scaling A.30 experimentally, and fit the data. If we assume the droplet to be in a quasi-static state, a force balance requires that capillarity balances the droplet's

weight force [Chevy et al., 2012]. We then can write an expression for Bo as

$$Bo = \frac{3A_c}{2\pi R^2}. \tag{A.33}$$

We then write

$$\frac{\delta}{R} = \frac{A_c}{2\pi R^2}\left|\ln\frac{A_c}{4\pi R^2}\right|, \tag{A.34}$$

$$\frac{\delta_{cm}}{R} = \frac{A_c}{2\pi R^2}\left|\ln\frac{e^{5/6}A_c}{4\pi R^2}\right|. \tag{A.35}$$

Thus, given a value of either the sag of the top of the droplet or the sag of the center of mass, we can numerically solve these equations for $A_c = \pi r_c(t)^2$.

Bibliography

[Agüero et al., 2022] Agüero, E. A., Alventosa, L., Harris, D. M., and Galeano-Rios, C. A. (2022). Impact of a rigid sphere onto an elastic membrane. *Proceedings of the Royal Society A*, 478(2266):20220340.

[Ahearne et al., 2005] Ahearne, M., Yang, Y., El Haj, A. J., Then, K. Y., and Liu, K.-K. (2005). Characterizing the viscoelastic properties of thin hydrogel-based constructs for tissue engineering applications. *Journal of the Royal Society Interface*, 2(5):455–463.

[Anders et al., 1993] Anders, K., Roth, N., and Frohn, A. (1993). The velocity change of ethanol droplets during collision with a wall analysed by image processing. *Experiments in Fluids*, 15(2):91–96.

[Askari, 2021] Askari, E. (2021). Mathematical models for characterizing non-hertzian contacts. *Applied Mathematical Modelling*, 90:432–447.

[Aussillous and Quéré, 2001] Aussillous, P. and Quéré, D. (2001). Liquid marbles. *Nature*, 411(6840):924–927.

[Aussillous and Quéré, 2006] Aussillous, P. and Quéré, D. (2006). Properties of liquid marbles. *Proceedings of the Royal Society A: Mathematical, Physical and Engineering Sciences*, 462(2067):973–999.

[Bach et al., 2004] Bach, G. A., Koch, D. L., and Gopinath, A. (2004). Coalescence and bouncing of small aerosol droplets. *Journal of Fluid Mechanics*, 518:157–185.

[Balla et al., 2019] Balla, M., Tripathi, M. K., and Sahu, K. C. (2019). Shape oscillations of a nonspherical water droplet. *Physical Review E*, 99(2):023107.

[Begley and Mackin, 2004] Begley, M. R. and Mackin, T. J. (2004). Spherical indentation of freestanding circular thin films in the membrane regime. *Journal of the Mechanics and Physics of Solids*, 52(9):2005–2023.

[Benjamin and Ursell, 1954] Benjamin, T. B. and Ursell, F. J. (1954). The stability of the plane free surface of a liquid in vertical periodic motion. *Proceedings of the Royal Society of London. Series A. Mathematical and Physical Sciences*, 225(1163):505–515.

[Biance et al., 2006] Biance, A.-L., Chevy, F., Clanet, C., Lagubeau, G., and Quéré, D. (2006). On the elasticity of an inertial liquid shock. *Journal of Fluid Mechanics*, 554:47–66.

[Biance et al., 2003] Biance, A.-L., Clanet, C., and Quéré, D. (2003). Leidenfrost drops. *Physics of Fluids*, 15(6):1632–1637.

[Bird et al., 2010] Bird, J. C., De Ruiter, R., Courbin, L., and Stone, H. A. (2010). Daughter bubble cascades produced by folding of ruptured thin films. *Nature*, 465(7299):759–762.

[Blanchette, 2016] Blanchette, F. (2016). Modeling the vertical motion of drops bouncing on a bounded fluid reservoir. *Physics of Fluids*, 28(3):032104.

[Blanchette, 2017] Blanchette, F. (2017). Octahedra as models of oscillating and bouncing drops. *Physical Review Fluids*, 2(9):093603.

[Bormashenko, 2011] Bormashenko, E. (2011). Liquid marbles: properties and applications. *Current Opinion in Colloid & Interface Science*, 16(4):266–271.

[Boyd, 2006] Boyd, J. P. (2006). Asymptotic fourier coefficients for a c bell (smoothed-"top-hat") & the fourier extension problem. *Journal of Scientific Computing*, 29(1):1–24.

[Bradley and Stow, 1978] Bradley, S. and Stow, C. (1978). Collisions between liquid drops. *Philosophical Transactions of the Royal Society of London. Series A, Mathematical and Physical Sciences*, 287(1349):635–675.

[Bruzzone et al., 2021a] Bruzzone, F., Maggi, T., Marcellini, C., and Rosso, C. (2021a). 2d nonlinear and non-hertzian gear teeth deflection model for static transmission error calculation. *Mechanism and Machine Theory*, 166:104471.

[Bruzzone et al., 2021b] Bruzzone, F., Maggi, T., Marcellini, C., and Rosso, C. (2021b). Gear teeth deflection model for spur gears: Proposal of a 3d nonlinear and non-hertzian approach. *Machines*, 9(10):223.

[Burrill and Woods, 1969] Burrill, K. and Woods, D. (1969). Change in interface and film shapes for a deformable drop at a deformable liquid-liquid interface: Part i. film hydrodynamic pressure distribution and interface shapes. *Journal of Colloid and Interface Science*, 30(4):511–524.

[Burton et al., 2012] Burton, J., Sharpe, A., Van Der Veen, R., Franco, A., and Nagel, S. (2012). Geometry of the vapor layer under a leidenfrost drop. *Physical Review Letters*, 109(7):074301.

[Bush and Oza, 2020] Bush, J. W. and Oza, A. U. (2020). Hydrodynamic quantum analogs. *Reports on Progress in Physics*, 84(1):017001.

[Callies and Quéré, 2005] Callies, M. and Quéré, D. (2005). On water repellency. *Soft matter*, 1(1):55–61.

[Castrejón-Pita et al., 2016] Castrejón-Pita, J. R., Muñoz-Sánchez, B. N., Hutchings, I. M., and Castrejón-Pita, A. (2016). Droplet impact onto moving liquids. *Journal of Fluid Mechanics*, 809:716–725.

[Chandrasekhar, 2013] Chandrasekhar, S. (2013). *Hydrodynamic and hydromagnetic stability*. Courier Corporation.

[Chevy et al., 2012] Chevy, F., Chepelianskii, A., Quéré, D., and Raphaël, E. (2012). Liquid Hertz contact: Softness of weakly deformed drops on non-wetting substrates. *EPL (Europhysics Letters)*, 100(5):54002.

[Clanet et al., 2004] Clanet, C., Béguin, C., Richard, D., and Quéré, D. (2004). Maximal deformation of an impacting drop. *Journal of Fluid Mechanics*, 517:199–208.

[Colosqui et al., 2016] Colosqui, C. E., Wexler, J. S., Liu, Y., and Stone, H. A. (2016). Crossover from shear-driven to thermally activated drainage of liquid-infused microscale capillaries. *Physical Review Fluids*, 1(6):064101.

[Couder et al., 2005a] Couder, Y., Fort, E., Gautier, C.-H., and Boudaoud, A. (2005a). From bouncing to floating: noncoalescence of drops on a fluid bath. *Physical Review Letters*, 94(17):177801.

[Couder et al., 2005b] Couder, Y., Protiere, S., Fort, E., and Boudaoud, A. (2005b). Walking and orbiting droplets. *Nature*, 437(7056):208–208.

[Courbin et al., 2006] Courbin, L., Marchand, A., Vaziri, A., Ajdari, A., and Stone, H. A. (2006). Impact dynamics for elastic membranes. *Physical Review Letters*, 97(24):244301.

[Courty et al., 2006] Courty, S., Lagubeau, G., and Tixier, T. (2006). Oscillating droplets by decomposition on the spherical harmonics basis. *Physical Review E*, 73(4):045301.

[Cundall and Strack, 1979] Cundall, P. A. and Strack, O. D. (1979). A discrete numerical model for granular assemblies. *geotechnique*, 29(1):47–65.

[de Ruiter et al., 2015a] de Ruiter, J., Lagraauw, R., Mugele, F., and van den Ende, D. (2015a). Bouncing on thin air: how squeeze forces in the air film during non-wetting droplet bouncing lead to momentum transfer and dissipation. *Journal of Fluid Mechanics*, 776:531–567.

[de Ruiter et al., 2015b] de Ruiter, J., Lagraauw, R., Van Den Ende, D., and Mugele, F. (2015b). Wettability-independent bouncing on flat surfaces mediated by thin air films. *Nature Physics*, 11(1):48–53.

[de Ruiter et al., 2012] de Ruiter, J., Oh, J. M., van den Ende, D., and Mugele, F. (2012). Dynamics of collapse of air films in drop impact. *Physical Review Letters*, 108(7):074505.

[Dell'Aversana et al., 1996] Dell'Aversana, P., Banavar, J. R., and Koplik, J. (1996). Suppression of coalescence by shear and temperature gradients. *Physics of Fluids*, 8(1):15–28.

[Dias et al., 2008] Dias, F., Dyachenko, A. I., and Zakharov, V. E. (2008). Theory of weakly damped free-surface flows: a new formulation based on potential flow solutions. *Physics Letters A*, 372(8):1297–1302.

[Dorbolo et al., 2005] Dorbolo, S., Volfson, D., Tsimring, L., and Kudrolli, A. (2005). Dynamics of a bouncing dimer. *Physical Review Letters*, 95(4):044101.

[Driscoll et al., 2010] Driscoll, M. M., Stevens, C. S., and Nagel, S. R. (2010). Thin film formation during splashing of viscous liquids. *Physical Review E*, 82(3):036302.

[Durey and Milewski, 2017] Durey, M. and Milewski, P. A. (2017). Faraday wave–droplet dynamics: discrete-time analysis. *Journal of Fluid Mechanics*, 821:296–329.

[Ellison and Zisman, 1954] Ellison, A. and Zisman, W. (1954). Wettability studies on nylon, polyethylene terephthalate and polystyrene. *The Journal of Physical Chemistry*, 58(6):503–506.

[Farkas et al., 1999] Farkas, Z., Tegzes, P., Vukics, A., and Vicsek, T. (1999). Transitions in the horizontal transport of vertically vibrated granular layers. *Physical Review E*, 60(6):7022.

[Fermi, 1949] Fermi, E. (1949). On the origin of the cosmic radiation. *Physical review*, 75(8):1169.

[Fudge et al., 2021] Fudge, B. D., Cimpeanu, R., and Castrejón-Pita, A. A. (2021). Dipping into a new pool: The interface dynamics of drops impacting onto a different liquid. *Physical Review E*, 104(6):065102.

[Galeano-Rios et al., 2021a] Galeano-Rios, C. A., Cimpeanu, R., Bauman, I. A., MacEwen, A., Milewski, P. A., and Harris, D. M. (2021a). Capillary-scale solid rebounds: experiments, modelling and simulations. *Journal of Fluid Mechanics*, 912.

[Galeano-Rios et al., 2021b] Galeano-Rios, C. A., Cimpeanu, R., Bauman, I. A., MacEwen, A., Milewski, P. A., and Harris, D. M. (2021b). Capillary-scale solid rebounds: experiments, modelling and simulations. *Journal of Fluid Mechanics*, 912.

[Galeano-Rios et al., 2017] Galeano-Rios, C. A., Milewski, P. A., and Vanden-Broeck, J.-M. (2017). Non-wetting impact of a sphere onto a bath and its application to bouncing droplets. *Journal of Fluid Mechanics*, 826:97–127.

[Galeano-Rios et al., 2019] Galeano-Rios, C. A., Milewski, P. A., and Vanden-Broeck, J.-M. (2019). Quasi-normal free-surface impacts, capillary rebounds and application to Faraday walkers. *Journal of Fluid Mechanics*, 873:856–888.

[Gielen et al., 2017] Gielen, M. V., Sleutel, P., Benschop, J., Riepen, M., Voronina, V., Visser, C. W., Lohse, D., Snoeijer, J. H., Versluis, M., and Gelderblom, H. (2017). Oblique drop impact onto a deep liquid pool. *Physical review fluids*, 2(8):083602.

[Gilet and Bush, 2009] Gilet, T. and Bush, J. W. (2009). The fluid trampoline: droplets bouncing on a soap film. *Journal of Fluid Mechanics*, 625:167–203.

[Gilet and Bush, 2012] Gilet, T. and Bush, J. W. (2012). Droplets bouncing on a wet, inclined surface. *Physics of Fluids*, 24(12):122103.

[Good et al., 2014] Good, G., Ireland, P., Bewley, G., Bodenschatz, E., Collins, L., and Warhaft, Z. (2014). Settling regimes of inertial particles in isotropic turbulence. *Journal of Fluid Mechanics*, 759:R3.

[Gopinath and Koch, 2001] Gopinath, A. and Koch, D. L. (2001). Dynamics of droplet rebound from a weakly deformable gas–liquid interface. *Physics of Fluids*, 13(12):3526–3532.

[Grabowski and Wang, 2013] Grabowski, W. W. and Wang, L.-P. (2013). Growth of cloud droplets in a turbulent environment. *Annual Review of Fluid Mechanics*, 45(1):293–324.

[Graeber et al., 2021] Graeber, G., Regulagadda, K., Hodel, P., Küttel, C., Landolf, D., Schutzius, T. M., and Poulikakos, D. (2021). Leidenfrost droplet trampolining. *Nature communications*, 12(1):1727.

[Gupta et al., 2015] Gupta, A., Sakthivel, T., and Seal, S. (2015). Recent development in 2d materials beyond graphene. *Progress in Materials Science*, 73:44–126.

[Halev and Harris, 2018] Halev, A. and Harris, D. M. (2018). Bouncing ball on a vibrating periodic surface. *Chaos: An Interdisciplinary Journal of Nonlinear Science*, 28(9):096103.

[Harris et al., 2013] Harris, D. M., Moukhtar, J., Fort, E., Couder, Y., and Bush, J. W. (2013). Wavelike statistics from pilot-wave dynamics in a circular corral. *Physical Review E*, 88(1):011001.

[Harvey et al., 2021] Harvey, D., Harper, J. M., and Burton, J. C. (2021). Minimum leidenfrost temperature on smooth surfaces. *Physical Review Letters*, 127(10):104501.

[He et al., 2015] He, P., Liu, Y., and Qiao, R. (2015). Fluid dynamics of the droplet impact processes in cell printing. *Microfluidics and Nanofluidics*, 18(4):569–585.

[Herbert et al., 2001] Herbert, E., Pharr, G., Oliver, W., Lucas, B., and Hay, J. (2001). On the measurement of stress–strain curves by spherical indentation. *Thin solid films*, 398:331–335.

[Hertz, 1882] Hertz, H. (1882). Über die berührung fester elastischer körper. *Journal für die reine und angewandte Mathematik*, 92(156-171):22.

[Hertz, 1896] Hertz, H. (1896). *Miscellaneous papers,(ed.) P. Lenard*. Macmillan London.

[Holmes, 1982] Holmes, P. J. (1982). The dynamics of repeated impacts with a sinusoidally vibrating table. *Journal of Sound and Vibration*, 84(2):173–189.

[Hongler and Figour, 1989] Hongler, M. and Figour, J. (1989). Periodic versus chaotic dynamics in vibratory feeders. *Helvetica Physica Acta*, 62(ARTICLE):68–81.

[Hundal, 1976] Hundal, M. (1976). Impact absorber with linear spring and quadratic law damper. *Journal of Sound and Vibration*, 48(2):189–193.

[Ionkin and Harris, 2018] Ionkin, N. and Harris, D. M. (2018). Note: A versatile 3d-printed droplet-on-demand generator. *Review of Scientific Instruments*, 89(11):116103.

[Jaeger et al., 1996] Jaeger, H. M., Nagel, S. R., and Behringer, R. P. (1996). Granular solids, liquids, and gases. *Reviews of modern physics*, 68(4):1259.

[Jayaratne and Mason, 1964] Jayaratne, O. W. and Mason, B. J. (1964). The coalescence and bouncing of water drops at an air/water interface. *Proceedings of the Royal Society of London. Series A. Mathematical and Physical Sciences*, 280(1383):545–565.

[Jiang et al., 1992] Jiang, Y., Umemura, A., and Law, C. K. (1992). An experimental investigation on the collision behaviour of hydrocarbon droplets. *Journal of Fluid Mechanics*, 234:171–190.

[Johnson, 1982] Johnson, K. L. (1982). One hundred years of hertz contact. *Proceedings of the Institution of Mechanical Engineers*, 196(1):363–378.

[Johnson and Johnson, 1987] Johnson, K. L. and Johnson, K. L. (1987). *Contact mechanics*. Cambridge university press.

[Josserand and Thoroddsen, 2016] Josserand, C. and Thoroddsen, S. T. (2016). Drop impact on a solid surface. *Annual Review of Fluid Mechanics*, 48:365–391.

[Kalker and Van Randen, 1972] Kalker, J. and Van Randen, Y. (1972). A minimum principle for frictionless elastic contact with application to non-hertzian half-space contact problems. *Journal of engineering mathematics*, 6(2):193–206.

[Karami, 1989] Karami, G. (1989). Non-hertzian contact problems. In *Lecture Notes in Engineering*, pages 145–203. Springer.

[Karl et al., 1996] Karl, A., Anders, K., Rieber, M., and Frohn, A. (1996). Deformation of liquid droplets during collisions with hot walls: experimental and numerical results. *Particle & particle systems characterization*, 13(3):186–191.

[Kavehpour, 2015] Kavehpour, H. P. (2015). Coalescence of drops. *Annual Review of Fluid Mechanics*, 47:245–268.

[Kim, 2007] Kim, J. (2007). Spray cooling heat transfer: the state of the art. *International Journal of Heat and Fluid Flow*, 28(4):753–767.

[Kim et al., 2019] Kim, S., Park, H., Gruszewski, H. A., Schmale, D. G., and Jung, S. (2019). Vortex-induced dispersal of a plant pathogen by raindrop impact. *Proceedings of the National Academy of Sciences*, 116(11):4917–4922.

[Kolinski et al., 2014] Kolinski, J. M., Mahadevan, L., and Rubinstein, S. M. (2014). Drops can bounce from perfectly hydrophilic surfaces. *Europhysics Letters*, 108(2):24001.

[Komaragiri et al., 2005] Komaragiri, U., Begley, M., and Simmonds, J. (2005). The mechanical response of freestanding circular elastic films under point and pressure loads. *J. Appl. Mech.*, 72(2):203–212.

[Korobkin, 1995] Korobkin, A. (1995). Impact of two bodies one of which is covered by a thin layer of liquid. *Journal of Fluid Mechanics*, 300:43–58.

[Kou and Saylor, 2008] Kou, J. and Saylor, J. R. (2008). A method for removing surfactants from an air/water interface. *Review of Scientific Instruments*, 79(12):123907.

[Lamb, 1895] Lamb, H. (1895). Surface waves. *Hydrodynamics (Cambridge Univ Press, Cambridge, UK)*, pages 351–469.

[Lamb, 1924] Lamb, H. (1924). *Hydrodynamics*. University Press.

[Latka et al., 2012] Latka, A., Strandburg-Peshkin, A., Driscoll, M. M., Stevens, C. S., and Nagel, S. R. (2012). Creation of prompt and thin-sheet splashing by varying surface roughness or increasing air pressure. *Physical Review Letters*, 109(5):054501.

[Lee and Kim, 2008] Lee, D.-G. and Kim, H.-Y. (2008). Impact of a superhydrophobic sphere onto water. *Langmuir*, 24(1):142–145.

[Lefebvre and McDonell, 2017] Lefebvre, A. H. and McDonell, V. G. (2017). *Atomization and sprays*. CRC press.

[Li et al., 2016] Li, J., Qin, Q. H., Shah, A., Ras, R. H., Tian, X., and Jokinen, V. (2016). Oil droplet self-transportation on oleophobic surfaces. *Science advances*, 2(6):e1600148.

[Li et al., 2007] Li, X.-M., Reinhoudt, D., and Crego-Calama, M. (2007). What do we need for a superhydrophobic surface? a review on the recent progress in the preparation of superhydrophobic surfaces. *Chemical Society Reviews*, 36(8):1350–1368.

[Linke et al., 2006] Linke, H., Alemán, B., Melling, L., Taormina, M., Francis, M., Dow-Hygelund, C., Narayanan, V., Taylor, R., and Stout, A. (2006). Self-propelled leidenfrost droplets. *Physical Review Letters*, 96(15):154502.

[Lu et al., 2015] Lu, Y., Sathasivam, S., Song, J., Crick, C. R., Carmalt, C. J., and Parkin, I. P. (2015). Robust self-cleaning surfaces that function when exposed to either air or oil. *Science*, 347(6226):1132–1135.

[Luck and Mehta, 1993] Luck, J.-M. and Mehta, A. (1993). Bouncing ball with a finite restitution: chattering, locking, and chaos. *Physical Review E*, 48(5):3988.

[Ma and Burton, 2018] Ma, X. and Burton, J. C. (2018). Self-organized oscillations of leidenfrost drops. *Journal of Fluid Mechanics*, 846:263–291.

[Mahadevan and Pomeau, 1999] Mahadevan, L. and Pomeau, Y. (1999). Rolling droplets. *Physics of Fluids*, 11(9):2449–2453.

[Mandre et al., 2009] Mandre, S., Mani, M., and Brenner, M. P. (2009). Precursors to splashing of liquid droplets on a solid surface. *Physical Review Letters*, 102(13):134502.

[Mani et al., 2010] Mani, M., Mandre, S., and Brenner, M. P. (2010). Events before droplet splashing on a solid surface. *Journal of Fluid Mechanics*, 647:163–185.

[Marshall et al.,] Marshall, J., Illari, L., and Sigall, D. Mit weather-in-a-tank.

[Maxey and Riley, 1983] Maxey, M. R. and Riley, J. J. (1983). Equation of motion for a small rigid sphere in a nonuniform flow. *Physics of Fluids*, 26(4):883–889.

[McBennett and Harris, 2016] McBennett, B. G. and Harris, D. M. (2016). Horizontal stability of a bouncing ball. *Chaos: An Interdisciplinary Journal of Nonlinear Science*, 26(9):093105.

[McGuan et al., 2022] McGuan, R., Candler, R., and Kavehpour, H. (2022). The dynamics of bouncing, partially coalescing, liquid metal droplets in a viscous medium. *Journal of Fluid Mechanics*, 933.

[Miller and Scriven, 1968] Miller, C. and Scriven, L. (1968). The oscillations of a fluid droplet immersed in another fluid. *Journal of Fluid Mechanics*, 32(3):417–435.

[Moisy et al., 2009] Moisy, F., Rabaud, M., and Salsac, K. (2009). A synthetic schlieren method for the measurement of the topography of a liquid interface. *Experiments in Fluids*, 46(6):1021.

[Moláček and Bush, 2012] Moláček, J. and Bush, J. W. (2012). A quasi-static model of drop impact. *Physics of Fluids*, 24(12):127103.

[Moláček and Bush, 2013] Moláček, J. and Bush, J. W. (2013). Drops bouncing on a vibrating bath. *Journal of Fluid Mechanics*.

[Munk, 1951] Munk, W. H. (1951). Origin and generation of waves. Technical report, Scripps Institution of Oceanography La Jolla Calif.

[Myers and Charpin, 2009] Myers, T. and Charpin, J. (2009). A mathematical model of the leidenfrost effect on an axisymmetric droplet. *Physics of Fluids*, 21(6):063101.

[Nagurka and Huang, 2004] Nagurka, M. and Huang, S. (2004). A mass-spring-damper model of a bouncing ball. In *Proceedings of the 2004 American control conference*, volume 1, pages 499–504. IEEE.

[Neinhuis and Barthlott, 1997] Neinhuis, C. and Barthlott, W. (1997). Characterization and distribution of water-repellent, self-cleaning plant surfaces. *Annals of botany*, 79(6):667–677.

[Ohkubo et al., 2010] Ohkubo, Y., Tsuji, I., Onishi, S., and Ogawa, K. (2010). Preparation and characterization of super-hydrophobic and oleophobic surface. *Journal of Materials Science*, 45:4963–4969.

[Okumura et al., 2003] Okumura, K., Chevy, F., Richard, D., Quéré, D., and Clanet, C. (2003). Water spring: A model for bouncing drops. *EPL (Europhysics Letters)*, 62(2):237.

[Pan and Law, 2007] Pan, K.-L. and Law, C. K. (2007). Dynamics of droplet–film collision. *Journal of Fluid Mechanics*, 587:1–22.

[Park et al., 2005] Park, S., Jung, C., Jung, K., Lee, B., and Lee, K. (2005). Wet scrubbing of polydisperse aerosols by freely falling droplets. *Journal of Aerosol Science*, 36(12):1444–1458.

[Paul and Hashemi, 1981] Paul, B. and Hashemi, J. (1981). Contact Pressures on Closely Conforming Elastic Bodies. *Journal of Applied Mechanics*, 48(3):543–548.

[Planchette et al., 2012] Planchette, C., Biance, A., and Lorenceau, E. (2012). Transition of liquid marble impacts onto solid surfaces. *Europhysics letters*, 97(1):14003.

[Pomeau et al., 2012] Pomeau, Y., Le Berre, M., Celestini, F., and Frisch, T. (2012). The leidenfrost effect: From quasi-spherical droplets to puddles. *Comptes Rendus Mecanique*, 340(11-12):867–881.

[Qian and Law, 1997] Qian, J. and Law, C. K. (1997). Regimes of coalescence and separation in droplet collision. *Journal of Fluid Mechanics*, 331:59–80.

[Quéré, 2005] Quéré, D. (2005). Non-sticking drops. *Reports on Progress in Physics*, 68(11):2495.

[Rayleigh, 1879] Rayleigh, L. (1879). On the capillary phenomena of jets. *Proc. R. Soc. London*, 29(196-199):71–97.

[Reid, 1960] Reid, W. H. (1960). The oscillations of a viscous liquid drop. *Quarterly of Applied Mathematics*, 18(1):86–89.

[Reynolds, 1881] Reynolds, O. (1881). On drops floating on the surface of water. *Chem. News*, 44:211–212.

[Richard et al., 2002] Richard, D., Clanet, C., and Quéré, D. (2002). Contact time of a bouncing drop. *Nature*, 417(6891):811–811.

[Richard and Quéré, 2000] Richard, D. and Quéré, D. (2000). Bouncing water drops. *EPL (Europhysics Letters)*, 50(6):769.

[Rosso et al., 2019] Rosso, C., Bruzzone, F., Maggi, T., and Marcellini, C. (2019). A proposal for semi-analytical model of teeth contact with application to gear dynamics. Technical report, SAE Technical Paper.

[Sáenz et al., 2018] Sáenz, P. J., Cristea-Platon, T., and Bush, J. W. (2018). Statistical projection effects in a hydrodynamic pilot-wave system. *Nature Physics*, 14(3):315–319.

[Sanjay et al., 2022] Sanjay, V., Lakshman, S., Chantelot, P., Snoeijer, J. H., and Lohse, D. (2022). Drop impact on viscous liquid films. *arXiv preprint arXiv:2206.06298*.

[Schmieden, 1953] Schmieden, C. (1953). Der aufschlag von rotationskörpern auf eine wasseroberfläche. richard v. Mises zum 70. geburtstag gewidmet. *ZAMM-Journal of Applied Mathematics and Mechanics/Zeitschrift für Angewandte Mathematik und Mechanik*, 33(4):147–151.

[Schotland, 1960] Schotland, R. (1960). Experimental results relating to the coalescence of water drops with water surfaces. *Discussions of the Faraday Society*, 30:72–77.

[Schwarz, 2022] Schwarz, D. (2022). Fast and robust curve intersections. https://www.mathworks.com/matlabcentral/fileexchange/11837-fast-and-robust-curve-intersections.

[Scolan and Korobkin, 2001] Scolan, Y.-M. and Korobkin, A. A. (2001). Three-dimensional theory of water impact. Part 1: Inverse Wagner problem. *Journal of Fluid Mechanics*, 440:293.

[Selvadurai, 2006] Selvadurai, A. (2006). Deflections of a rubber membrane. *Journal of the Mechanics and Physics of Solids*, 54(6):1093–1119.

[Sharma and Dixit, 2020] Sharma, P. K. and Dixit, H. N. (2020). Energetics of a bouncing drop: Coefficient of restitution, bubble entrapment, and escape. *Physics of Fluids*, 32(11):112107.

[Shiri and Bird, 2017] Shiri, S. and Bird, J. C. (2017). Heat exchange between a bouncing drop and a superhydrophobic substrate. *Proceedings of the National Academy of Sciences*, 114(27):6930–6935.

[Sobac et al., 2014] Sobac, B., Rednikov, A., Dorbolo, S., and Colinet, P. (2014). Leidenfrost effect: Accurate drop shape modeling and refined scaling laws. *Physical Review E*, 90(5):053011.

[Sreenivas et al., 1999] Sreenivas, K., De, P., and Arakeri, J. H. (1999). Levitation of a drop over a film flow. *Journal of Fluid Mechanics*, 380:297–307.

[Storey, 1968] Storey, S. (1968). The convergence of Fourier–Bessel expansions. *The Computer Journal*, 10(4):402–405.

[Tang et al., 2012] Tang, C., Zhang, P., and Law, C. K. (2012). Bouncing, coalescence, and separation in head-on collision of unequal-size droplets. *Physics of Fluids*, 24(2):022101.

[Tang et al., 2018] Tang, X., Saha, A., Law, C. K., and Sun, C. (2018). Bouncing-to-merging transition in drop impact on liquid film: Role of liquid viscosity. *Langmuir*, 34(8):2654–2662.

[Tang et al., 2019] Tang, X., Saha, A., Law, C. K., and Sun, C. (2019). Bouncing drop on liquid film: Dynamics of interfacial gas layer. *Physics of Fluids*, 31(1):013304.

[Terwagne et al., 2013] Terwagne, D., Ludewig, F., Vandewalle, N., and Dorbolo, S. (2013). The role of the droplet deformations in the bouncing droplet dynamics. *Physics of Fluids*, 25(12):122101.

[Testik and Barros, 2007] Testik, F. and Barros, A. P. (2007). Toward elucidating the microstructure of warm rainfall: A survey. *Reviews of Geophysics*, 45(2).

[Thomson and Newall, 1886] Thomson, J. J. and Newall, H. F. (1886). On the formation of vortex rings by drops falling into liquids, and some allied phenomena. *Proceedings of the Royal Society of London*, 39(239-241):417–436.

[Thoroddsen and Mahadevan, 1997] Thoroddsen, S. and Mahadevan, L. (1997). Experimental study of coating flows in a partially-filled horizontally rotating cylinder. *Experiments in fluids*, 23(1):1–13.

[Thoroddsen and Takehara, 2000] Thoroddsen, S. T. and Takehara, K. (2000). The coalescence cascade of a drop. *Physics of Fluids*, 12(6):1265–1267.

[Tian et al., 2010] Tian, J., Arbatan, T., Li, X., and Shen, W. (2010). Liquid marble for gas sensing. *Chemical Communications*, 46(26):4734–4736.

[Tran et al., 2012] Tran, T., Staat, H. J., Prosperetti, A., Sun, C., and Lohse, D. (2012). Drop impact on superheated surfaces. *Physical Review Letters*, 108(3):036101.

[Tsamopoulos and Brown, 1983] Tsamopoulos, J. A. and Brown, R. A. (1983). Nonlinear oscillations of inviscid drops and bubbles. *Journal of Fluid Mechanics*, 127:519–537.

[Tufillaro et al., 1992] Tufillaro, N. B., Abbott, T., and Reilly, J. (1992). *An experimental approach to nonlinear dynamics and chaos*. Addison-Wesley Redwood City, CA.

[Tuteja et al., 2007] Tuteja, A., Choi, W., Ma, M., Mabry, J. M., Mazzella, S. A., Rutledge, G. C., McKinley, G. H., and Cohen, R. E. (2007). Designing superoleophobic surfaces. *Science*, 318(5856):1618–1622.

[Vadivelu et al., 2017a] Vadivelu, R. K., Kamble, H., Munaz, A., and Nguyen, N.-T. (2017a). Liquid marble as bioreactor for engineering three-dimensional toroid tissues. *Scientific reports*, 7(1):1–14.

[Vadivelu et al., 2017b] Vadivelu, R. K., Kamble, H., Munaz, A., and Nguyen, N.-T. (2017b). Liquid marbles as bioreactors for the study of three-dimensional cell interactions. *Biomedical microdevices*, 19:1–9.

[van Limbeek et al., 2021] van Limbeek, M. A., Ramírez-Soto, O., Prosperetti, A., and Lohse, D. (2021). How ambient conditions affect the leidenfrost temperature. *Soft matter*, 17(11):3207–3215.

[Vella et al., 2006] Vella, D., Lee, D.-G., and Kim, H.-Y. (2006). The load supported by small floating objects. *Langmuir*, 22(14):5979–5981.

[Wagner, 1932] Wagner, H. (1932). Über stoß-und gleitvorgänge an der oberfläche von flüssigkeiten. *ZAMM-Journal of Applied Mathematics and Mechanics/Zeitschrift für Angewandte Mathematik und Mechanik*, 12(4):193–215.

[Wang et al., 2020] Wang, D., Sun, Q., Hokkanen, M. J., Zhang, C., Lin, F.-Y., Liu, Q., Zhu, S.-P., Zhou, T., Chang, Q., He, B., et al. (2020). Design of robust superhydrophobic surfaces. *Nature*, 582(7810):55–59.

[Wang et al., 2021] Wang, G., McDonough, J. R., Zivkovic, V., Long, T., and Wang, S. (2021). From thermal energy to kinetic energy: Droplet motion triggered by the leidenfrost effect. *Advanced Materials Interfaces*, 8(2):2001249.

[Wang et al., 2022] Wang, Y., Zhao, Y., Sun, L., Mehrizi, A. A., Lin, S., Guo, J., and Chen, L. (2022). Successive rebounds of impinging water droplets on superhydrophobic surfaces. *Langmuir*, 38(12):3860–3867.

[Worthington, 1908] Worthington, A. M. (1908). *A study of splashes*. Longmans, Green, and Company.

[Wu et al., 2020] Wu, Z., Hao, J., Lu, J., Xu, L., Hu, G., and Floryan, J. (2020). Small droplet bouncing on a deep pool. *Physics of Fluids*, 32(1):012107.

[Yang et al., 2011] Yang, J., Zhang, Z., Xu, X., Men, X., Zhu, X., and Zhou, X. (2011). Superoleophobic textured aluminum surfaces. *New Journal of Chemistry*, 35(11):2422–2426.

[Yarin, 2006] Yarin, A. L. (2006). Drop impact dynamics: splashing, spreading, receding, bouncing. *Annual Review of Fluid Mechanics*, 38:159–192.

[Yun, 2018] Yun, S. (2018). Impact dynamics of egg-shaped drops on a solid surface for suppression of the bounce magnitude. *International Journal of Heat and Mass Transfer*, 127:172–178.

[Zhao et al., 2011] Zhao, H., Brunsvold, A., and Munkejord, S. T. (2011). Transition between coalescence and bouncing of droplets on a deep liquid pool. *International Journal of Multiphase Flow*, 37(9):1109–1119.

[Zou et al., 2013] Zou, J., Ren, Y., Ji, C., Ruan, X., and Fu, X. (2013). Phenomena of a drop impact on a restricted liquid surface. *Experimental Thermal and Fluid Science*, 51:332–341.

[Zou et al., 2011] Zou, J., Wang, P. F., Zhang, T. R., Fu, X., and Ruan, X. (2011). Experimental study of a drop bouncing on a liquid surface. *Physics of Fluids*, 23(4):044101.